Process Window and Variation Characterization of the Micro Embossing Process

by

Qi Wang

B.S., Mechanical Engineering
Tsinghua University at Beijing, China, 2000

M.S., Innovation of Manufacturing System and Technology
Singapore-MIT Alliance, Singapore, 2003

Submitted to the Department of Mechanical Engineering
in Partial Fulfillment of the Requirements for the Degree of
Master of Science in Mechanical Engineering
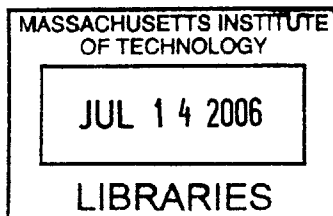
at the

Massachusetts Institute of Technology

June 2006

Signature of Author . . . .
Department of Mechanical Engineering
May 22, 2006

Certified by . . . .
David E.Hardt
Professor of Mechanical Engineering
Thesis Supervisor

Accepted by . . . .
Lallit Anand
Chairman, Department Committee on Graduate Students

BARKER   - 1 -

Process Window and Variation Characterization of the Micro Embossing Process

By

Qi Wang

Submitted to the Department of Mechanical Engineering
on May 22, 2006 in Partial Fulfillment of the Requirements for the
Degree of Master of Science in Mechanical Engineering

ABSTRACT

The micro embossing process on polymethylmethacrylate (PMMA) is demonstrated experimentally to be a useful process to produce micro fluidic and optical devices. Because this process is a one step thermoplastic deformation process, it is possible to reach high production rates and low cost in manufacturing compared to the standard clean room processes. Currently, the research about this process is still on the feasibility level, with not a quantitative work to optimize the process parameters and assure product quality.

In this thesis, an experimental study on process window and variation of Micro Embossing is presented. This study includes the design and manufacturing of an embossing die, the development of an embossing product quality assessment protocol, the process window characterization and the process variation identification.

The research results based on the experimental set up in this thesis show that we should apply constant 800N embossing force at an embossing velocity of 1000N/min in order to obtain well formed parts to maintain low process cycle time. An embossing temperature of 120°C and de-embossing temperature of 55°C are shown to be the optimal embossing condition to yield good replication and repeatability. These embossing parameters operating window can change with the variation of working piece material, die material and die design.

Thesis supervisor: David E. Hardt
Title: Professor of Mechanical Engineering

ACKNOWLEDGEMENTS

This acknowledgement completes my thesis. It is just like that the support and help I obtained from the wonderful people around me complete my experience at MIT.

I would love to express my deep and sincere gratefulness to my supervisor Professor David E Hardt. I have been under his supervision since 2003. During the three years, Professor Hardt has impressed me with his enthusiasm and integral view on research. His father-like patient caring of his students makes him the best supervisor I have ever met. I am extremely glad that I have this chance to work with and learn from Professor Hardt.

My lovely lab-mates also make my life easier and research work more interesting. Kunal Thaker and Grant Shoji are the best ones to have as colleagues. Both of them are always standing by me and are willing to help out at any time. I can never forget how many times they have helped in uninstalling and reinstalling the old embossing platen for me; I can never forget how many times they have helped in revising my presentation slides for me. Mathew Dirckx and Adam Rzepniewski are very supportive too. They have been very generous in sharing their opinions in improving my research work.

My gratitude also goes to my friends, Yexin, Rongling, Poh, Jon, Yihui, Gianpietro, Lei, Hua, Miao, Chao, Do, Baiyu. I am totally sorry if you have been receiving my phone calls in the midnights, but who let you become my best friends!

I would also like to thank the SMA program and the Department of Mechanical Engineering for funding this research and making my work at MIT possible.

To My dearest family:

Grannies, Mom & Dad, Brother & Sister-in-law, and Leonide Saad

TABLE OF CONTENTS

LIST OF FIGURES

LIST OF TABLES

1

<u>Background and Research Motivation</u>

1.1   Introduction

It has been demonstrated experimentally that micro embossing polymethylmethacrylate (PMMA) is a viable method of producing micro fluidic and optical devices. Because it is a single-step thermoplastic deformation process, it is possible to achieve high production rates with low cost compared to standard clean room processes. Research into PMMA micro embossing is currently on the feasibility level and there has not yet been much investigation into quantitative ways of optimizing the process parameters and ensuring the product quality.

In this thesis, the embossing experimental set up in our Manufacturing Process Control Laboratory is introduced. A product geometry quality assessment protocol is developed. Design of experiments with variable process parameters, such as embossing temperature, de-embossing temperature, embossing velocity and embossing force, is carried out. By analyzing qualities of the products that are embossed in different embossing situations, a process window characterization of the PMMA micro embossing process for manufacturing is presented. The throughput and the range of variability seen in embossed parts are also presented in this thesis.

In this chapter, applications of micro embossing are introduced, and basic micro embossing processes are described. Based on a review of current research and industrial applications, potential research topics are raised. The focus of this thesis is addressed. Finally, the structure of this thesis is outlined.

1.2 Background

1.2.1 Micro Devices

With the development of biological, chemical and optical engineering and fields such as telecommunications and energy generation, demand for micro devices is increasing. Compared to traditional large-scale devices, micro devices are accompanied by high cost efficiency, high throughput and high precision. These devices tend to fall into four major categories:

1. Micro fluidic delivery and separation devices;

2. Micro chemical reaction devices;

3. Micro computing devices;

4. Micro optical devices;

In the following section, these devices are introduced, along with basic theories of their operation and example applications.

Micro Fluidic Delivery and Separation Devices

In several bioengineering fields, such as pharmaceutical and biomedical fields, micro fluidic devices are already playing important roles in fluidic delivery and separation operations. Many existing devices, including the DNA separation and sequencing chip [1], nano-pore membrane chip[2], biosensor chip[3], and drug discovery chip[4], are made of micro fluidic networks that basically comprise micro channels and wells.

Take the DNA separation and sequencing chip for example. The design of this microchip is shown in Fig. 1-1. This chip is composed of four wells of radius 1mm, labeled I-IV which is connected by intersecting channels. The channel that connects wells

I and II is the separation channel, and the one that connects III and IV is the injection

channel. The channels are100μm in width and 40μm in depth.

Unit : mm
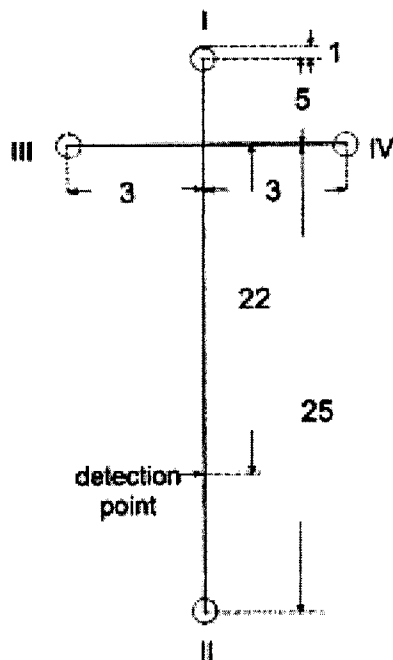
Figure1-1 Design of Microelectrophoresis Microchip (from [1])

As a high voltage is applied between wells III and IV, the DNA solution sample

is driven electro kinetically across the intersection of the channels from well III to well

IV. With appropriate switching of this voltage and the application of another high-voltage

between wells I and II, DNA sample fragments with various length are injected into the

separation channel and runs toward well II. An optical or electrochemical detection

method is applied at the detection point to detect the sequence of sample fragments [1].

Micro Chemical Reaction Devices

Micro fluidic devices that have micro pumps, valves, compressors, heat

exchangers, chemical reactors and chemical separations units are used as micro chemical

reaction devices in chemical, thermal, and solar systems [5][6]. These devices enable the exploration of microscale phenomena rapidly, directly and effectively, because only a small amount of chemical is involved and thus heat and mass transport can be done rapidly.

Take the micro chemical device that performs the Berthelot reaction for example [7]. Berthelot reaction is a reaction of ammonia with phenol-hypochlorite to give indophenol so as to analyze ammonia concentration in body fluid. The device structure is shown in Fig. 1-2. The layout of the chip is shown on the left and a schematic cross-section is shown on the right. S, R1, R2, and R3 are the inlet connections for the sample and reagents 1, 2 and 3, respectively. W is the waste outlet. In between each T-junction (where reagents are merged with sample) there is a mixing coil (channel cross-section: 30 μm×220 μm). Once all additions are done and all reagents mixed, the sample plug enters the reaction coil (channel cross-section: 200 μm×220 μm). The absorbance of the solution is measured at the end of this coil as it passes through the optical cuvette. Volume of the reaction coil is 10 μl.
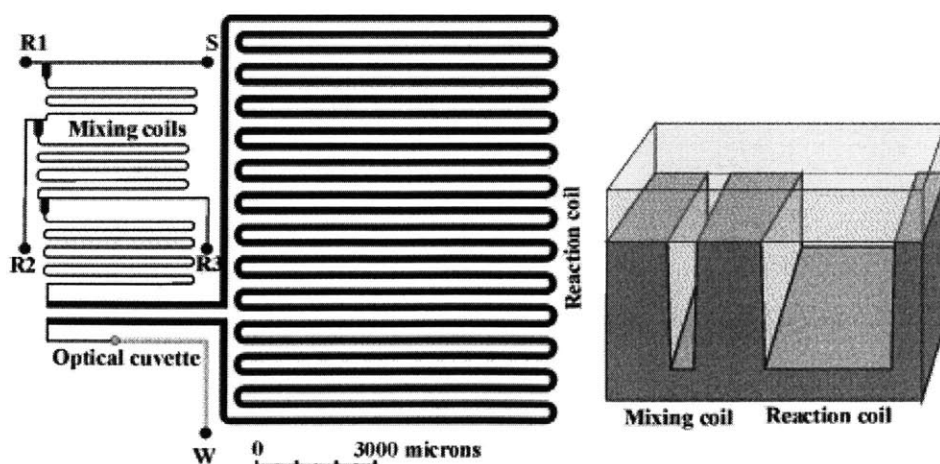
Figure 1-2   Micro Chemical Reactor Chip (from [7])

Micro computing devices

Micro computing devices are generally composed of highly integrated arrays of micro fluidic modules, analogous to electronic integrated circuits. These devices contain fluid networks with thousands of micromechanical valves and hundreds of individually addressable chambers [8]. One key component of these devices is the multiplexer, shown in Fig. 1-3 (a).

A multiplexer is a combinatorial array of binary valves that exponentially increases the processing power of a network by allowing complex fluid manipulations with a minimal number of inputs. The blue lines represent flow channels containing the fluid of interest; the red lines represent control lines that can be hydraulically actuated. Valves are formed at the intersection of the wide part of a control channel with a flow channel. The actuation pressure is chosen so that only the wide membranes are fully deflected. Each combination of open and closed valves in the multiplexer selects for a single channel, so that n flow channels can be addressed with only $2log2(n)$ control channels. The cyan channel is working as a flow channel when integrated to another multiplexer.
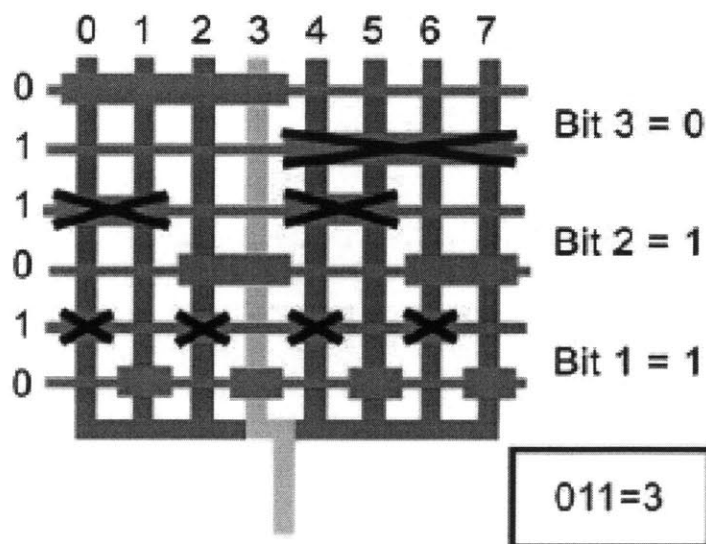
(a)   Microfluidic Multiplexer

A

Row multiplexor

Horizontal compartmentalization valve

Sample input

Wash buffer input

Purge buffer input

Sample output

Column multiplexor

Vertical compartmentalization valve

5 mm
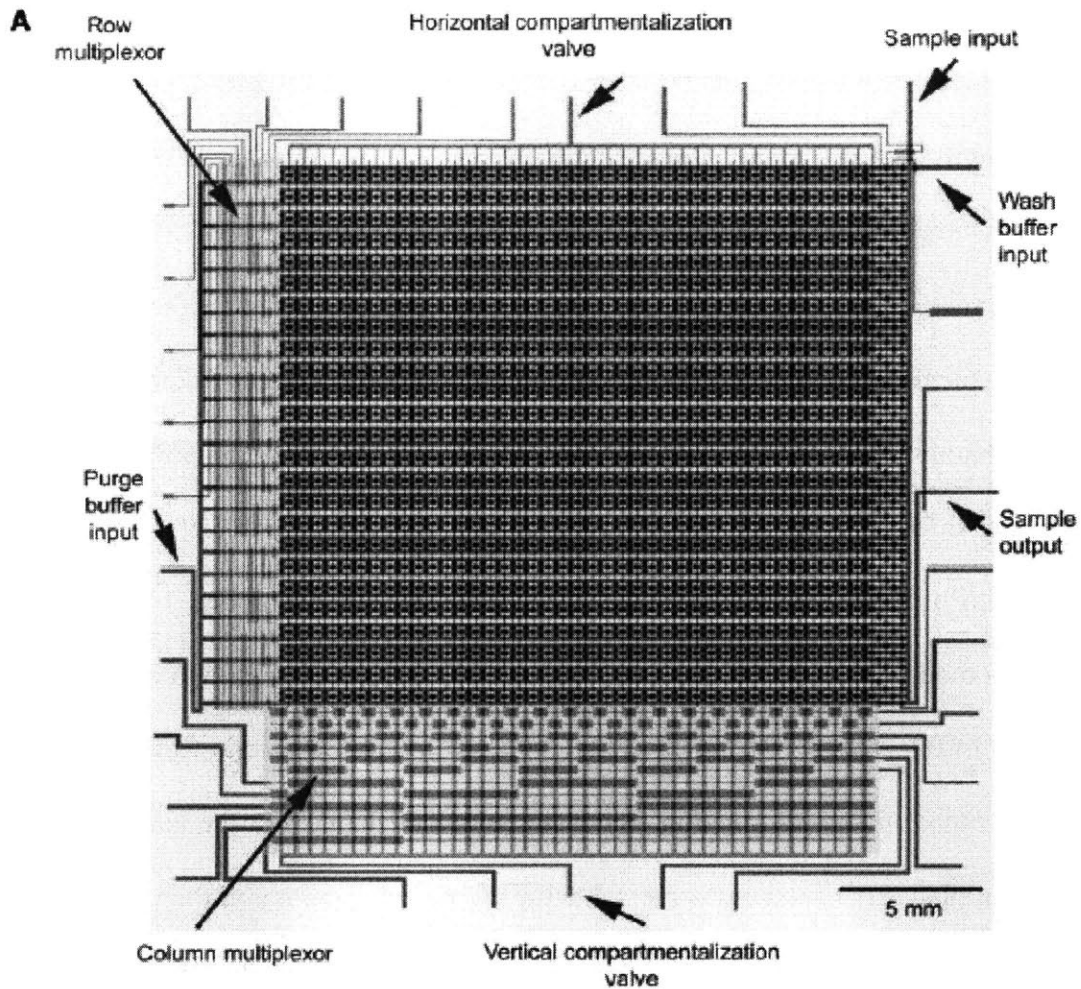
(b)   Highly Integrated Microfluidid Memory Storage Device

Figure1-3   Microfluidic Computing Device (from [8])

The flow channel is 100μm wide and 9μm high. The valves are 100μm wide and

100μm high, and the crossover regions are 50μm wide and 100μm high. The integrated

device is shown in Fig. 1-3(b). It is 4 inches in diameter.

Micro optical devices, such as one or two dimensional diffraction gratings, subwavelength gratings, micro lenses, and micro prisms, have the advantage of being lightweight, compact, and efficient. They are widely used in optical sensors, energy generators, medical image scanners and other optical instruments.

A typical micro optical module, the double-sided refractive/diffractive hybrid element is shown in Fig.1-4[9]. The optical module is actually a combination of refractive or diffractive surfaces on opposite sides of a lens. By using different combinations of surfaces, different optical functions can be realized. Fig. 1-4(a) illustrates a module designed to have achromatic properties for imaging in outdoor conditions. In Fig. 1-4 (b), the single module in (a) is replicated several times: this array can handle more optical information than a single module alone. For the lenses shown in Fig. 1-4, the planarity of the base layers and the alignment accuracy of the optical axes on both sides need to be within $\pm 2 \mu$m.
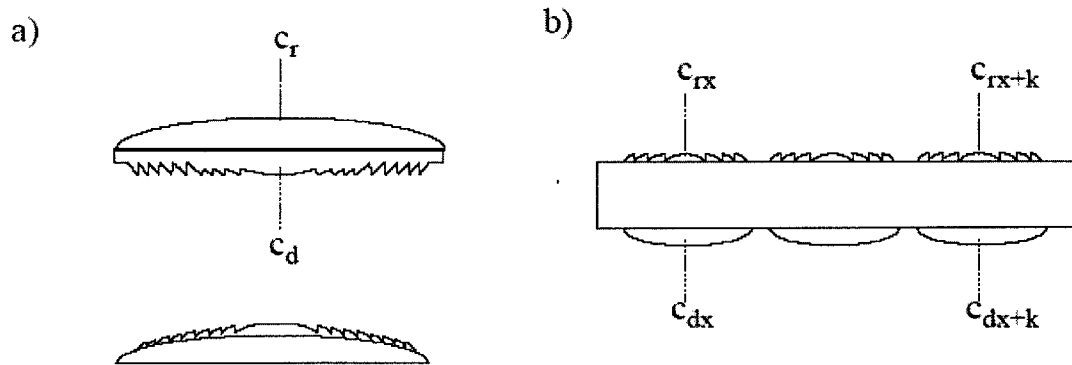
Figure1-4 Double Sided Refractive/Diffractive Combination Micro Optical module (from [9])

1.2.2 Micro Manufacturing Processes

Many processes, such as conventional Clean Room Processes/lithography, soft lithography, micro injection molding and micro embossing molding, can be used to manufacture micro features in the devices discussed above. However, demanding requirements, including high surface finish requirement, high dimensional precision requirement, high aspect ratio requirement, high alignment requirement and high feature density requirements are observed in some or all of micro devices. These requirements raise manufacturing challenges. Also because of some other special requirements, including biocompatibility, the ability to resist chemical erosion, good optical properties, high productivity and low production cost, some manufacturing methods may be better suited to their manufacture than others. In this section, four potential manufacturing processes are discussed.

Clean Room Processes

Clean room processes are those lithography processes involving deposition, patterning and etching processes. One or more patterned masks are required in these processes. These processes are most often used to produce silicon or glass chips. Because clean room processes have been thoroughly studied, and are capable of producing the needed feature dimensions with good precision, they are strong candidates for the manufacture of micro devices. Some existing commercial micro fluidic devices, the DNA separation LabChip® developed by Caliper LifeSciences in 1999 [10], for example, are manufactured in a clean room on a glass substrate.

However, it is not clear that traditional clean room processes are the first choice for the fabrication of microfluidic devices. Bonding of silicon or glass requires high temperatures, which may damage delicate surface chemistry of many micro biomedical devices. For micro fluidic devices with moving parts, like a micro accelerometer, the intrinsic stiffness of silicon or glass becomes a barrier to fabricate smaller and thinner parts. Additionally, it's very hard to maintain planar uniformity when using wafers larger than 4 inches in diameter, which decreases the processing yield. High priced masks and processing facilities and slow processing speeds make disposable products very expensive.

One way of compensating for these drawbacks is changing the materials and modifying the manufacturing processes. Compared to silicon and glass, soft polymer materials, such as PMMA, PDMS, and PVC, offer many advantages. Firstly, the properties of these materials are strongly temperature-dependant. By controlling the temperature, the strength and formability of the materials can be manipulated. This makes them easy to be formed or sealed in reasonable temperature ranges. Polymers are round 50 times cheaper than silicon, and mass production of polymer micro devices can bring down the per-unit cost even more.

By using polymers with soft lithography, injection molding, or hot embossing, manufactures may be able to avoid almost all the drawbacks of traditional clean room processes. These new processes are discussed briefly in the following sections.

Soft Lithography

Soft lithography is an alternative to silicon-based micromachining technique. In soft lithography, polymer materials are patterned by curing a solution in a micro machined mold. By controlling the temperature, and the proportion of reagents, the curing time and the product stiffness can be controlled. The most popular soft lithography material is PDMS. Soft lithography has been successfully used in making micro gratings [11], microfluidic devices [12] and other micro devices.

The advantages of soft lithography are the capacity for rapid prototyping, easy fabrication without expensive capital equipment, and forgiving process parameters. By doing precise alignment, multilayer devices can be made [13].Using this technique, some moving parts, such as on-off valves, switches and pumps, which are hard to pattern in a single layer, can be manufactured. The softness of materials allows the device area to be reduced by more than two orders of magnitude compared with silicon-based devices the desired strength and flexibility could be realized.

Soft lithography also has disadvantages. Because soft material is prone to shrinkage, the manufactured part exerts some force on the mold. This makes peeling soft materials from rigid molds more likely to damage products. This happens more often when aspect ratio is big and features are dense. The curing stage of soft lithography can take from 1 to 4 hours, which lowers production rates. Since soft lithography parts start as a solution, bubbles often remain in the parts, which affect optical properties as well as mechanical strength of the parts.

UV light sometimes is used to assist and accelerate the curing process [14]. In order to exile the air bubbles, vacuum can be applied [15]. Soft lithography sometimes is also called UV or vacuum assisted micro casting.

Micro Injection Molding

Micro injection molding is an industrialized manufacturing process to manufacture micro scale parts from plastic materials. As reviewed in Ruprecht's paper [16], it has been a major technique to produce CDs since 1986. Micro injection molding techniques have improved over the years and now many micro optical and fluidic devices are produced in micro injection machines [17] [18]. Materials used for micro injection molding are mostly PMMA or PC. Dimensions of the injected parts fall into a region from 500 nm to several hundred micrometers.

Many advantages of micro injection molding make it a very attractive technique. The fast process cycle that can be brought down to just a few minutes enables cost effective mass production. By controlling the injection pressure applied to the material, good surface uniformity of manufactured parts can be ensured. Because the working materials are injected into the cavities in a quasi liquid state, the high mobility of the material makes it possible to produce devices with aspect ratios larger than 10. [19].

However, because working materials are processed under a wide range of temperatures from room temperature to 10 or 20 degrees above the polymer melting temperature, shrinkages of materials are large, and hence good uniformity in walls of different thicknesses is hard to achieve.

A more advanced injection molding, reaction injection molding, is now becoming popular. In reaction injection molding acryl based polymers are added to working materials. The reaction of injection materials with acryl based polymers makes injected parts easier to be released from the mold because the lubrication effect due to the reaction of injection materials [20].

Micro Embossing

Hot micro embossing is a single-step material deformation process, in which soft material is shaped with a featured die under pressure at a temperature above polymer glass transition temperature. Its application to manufacturing micro fluidic and optical devices has been successfully demonstrated [22] [23]. The most common materials for micro embossing are PMMA or PVC. Sizes of devices made with micro embossing range from several micrometers to hundreds of micrometers.

Micro embossing is performed over a smaller temperature range than soft lithography and micro injection molding. The materials experience one phase change from solid to quasi solid; hence there is less shrinkage of the material than in soft lithography and micro injection molding. The resulting improved uniformity of the embossed features makes this process stand out. The small range of operating temperature also makes this the most energy efficient process.

In micro injection molding, the material's temperature increases in the screw cavity of the machine while the screw is turning but in micro embossing, the temperature of the material is increased by external heat transfer. Thus, the heating time of the

injection process is shorter than that of the micro embossing process. This is a

shortcoming of the micro embossing process that should be overcome.

In this section, clean room processes and three major micro machining processes

based on soft materials were introduced and compared. Advantages and disadvantages

were discussed. It concludes that the soft materials have good bio-compatibility; optical

properties, mechanical properties and machining abilities, and thus they are very suitable

for making micro devices. Micro embossing is the most promising process because of its

low temperature range, good product uniformity and short cycle time.

1.2.3 Micro Embossing Process Research Review

Embossing, also known as imprinting or imprinting lithography[24][25], is

gaining more and more attention from researchers and industry because of the advantages

discussed in the previous section, and also because of the rich potential for improvement

of embossed products with continued research. In this section, the current research on the

micro embossing process is reviewed, and the research focus of this thesis is described.

The typical thermal and force cycles of micro embossing are shown in Fig.1-5. A

polymer piece is heated up from the ambient temperature to the embossing temperature.

This temperature then remains constant while the contact force between the polymer and

the die is brought up to the embossing force. After holding this force for a certain time,

the polymer and the embossing die are both cooled down to the de-embossing

temperature. Then the polymer piece and the die are separated, and the embossed part is

cooled down naturally in the ambient air from the de-embossing temperature.
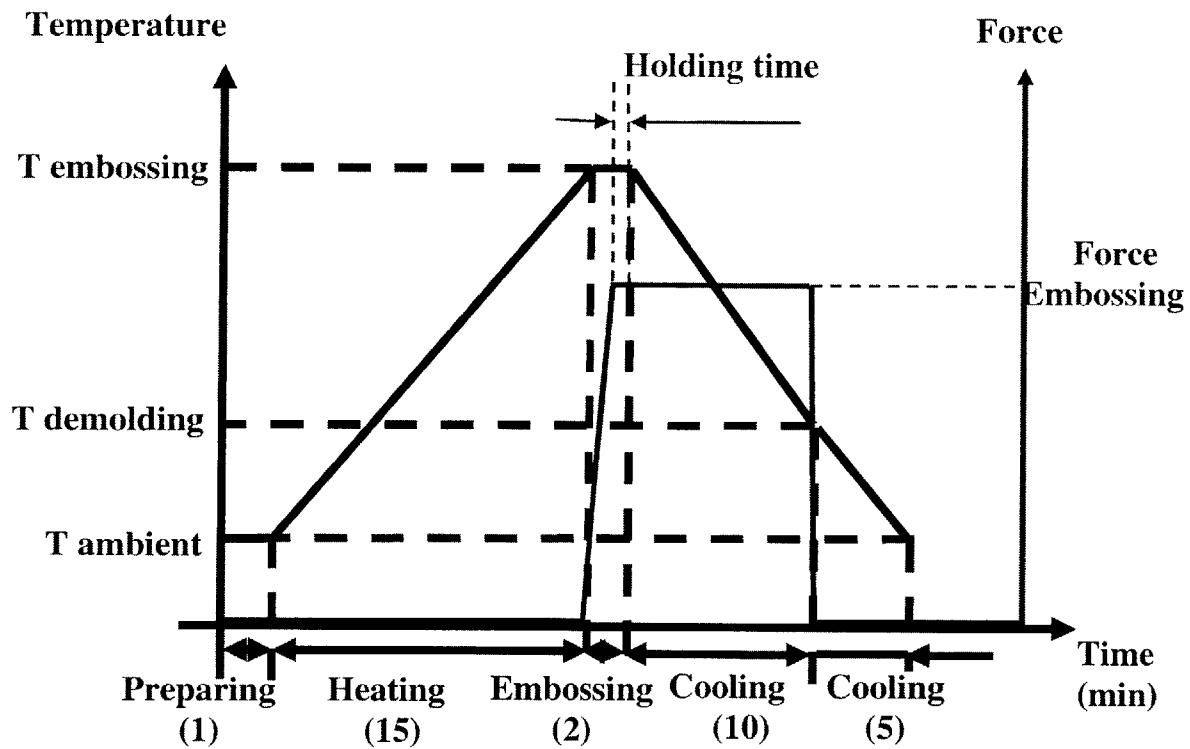
Figure 1-5   Thermal and Force Cycle of Typical Micro Embossing Process

Thermal Path

In a typical micro embossing process, the die and polymer piece are always heated up or cooled down simultaneously, which is defined by Juang [26] as isothermal process. The thermal paths for the heating and cooling time shown in Fig. 1-5 are both ramp lines, but they need not always be ramps. They can be any reasonable curves that bring the temperature up or down to the embossing or de-embossing temperatures. Whether and how variation of the heating and cooling paths affect the part quality is still unknown, and no research has been done on this problem.

Juang [26] also discusses non-isothermal processes, in which there is a temperature difference between the die and the polymer piece. In this case, the embossing die is normally heated up and pressed against the room temperature polymer piece. The experiment concluded that for the isothermal process, the replication accuracy depends on the embossing conditions, such as the embossing temperature and force, while in the non-isothermal process the replication accuracy is excellent as long as the transfer of the pattern on the die is completed, since a high temperature can be achieved locally.

The selection of the embossing and de-embossing temperature, or thermal path range, is a vital topic, and much research has been done on it. In [26], the isothermal embossing temperature range is $T_g + 10\,^\circ\text{C}$ to $T_g + 30\,^\circ\text{C}$, while the embossing and de-molding pressures are 4.16×10^5 and 1.04×10^5 Pa, respectively. The corresponding embossing time varies from 5 to 10 minutes. Displacement curves of the channel depth as a function of time are measured. These curves illustrate the temperature impact on the polymer displacement, and they show that higher embossing temperatures lead to faster material displacement. The de-embossing temperature is between 25 °C to 40 °C in [26] to minimize the thermal residual stress. This is a guess based on analysis of the polymer and no specific experiments were actually done on the selection of the de-embossing temperature.

Some researchers [45] set the embossing temperature to a higher value: $T_g + 90\,^\circ\text{C}$, with the corresponding pressure of 125×10^5 Pa. Atomic Force Microscopy (AFM) is used to image the embossed features, and some flow patterns, like wave-like

cross sections, and spot-like and mound-like fillings, are observed. No variations of embossing temperature or embossing pressure were applied in these experiments.

Yao reports in paper [46] that the embossing process can be done on polymers at room temperature. However, the die wearing is more severe than for the dies used at higher temperature. Also, the embossing force required is much larger than in the typical hot embossing process. Heyderman [41], on the other hand, uses an embossing temperature as high as 270°C or 290°C in order to minimize the viscosity of the polymer and obtain the easiest material flow.

The research work discussed above displays a large range of embossing and de-embossing temperatures. No systematic study has been done to compare the impact of the different embossing temperature ranges on the final embossed products.

Force Path

The force path shown in Fig. 1-5 is a typical micro embossing path. Juang [26] explores a different force path. Instead of using the ramp force path, stepped forces are adopted in the experiments. Since there is no comparison in that paper, the impact of the force path is not elaborated. However, the good replication accuracy shows that this step change in force does work in the micro embossing process.

The force range is another major embossing parameter. The magnitude of the force needed strongly depends on other embossing parameters. For example, in Juang's work [26], for different embossing temperatures, different embossing forces are required. Embossing at room temperature requires a larger embossing force [46]. The required embossing force can also vary with embossing time [26]. With dense feature design, a

larger embossing force is needed to ensure complete material flow [36]. By changing the

embossing force, the dynamic filling of the material into the cavities can be frozen so that

the material filling path and mechanism can be observed.

In the research performed so far, no minimum embossing force has been pointed

out. This is partially because it is not more expensive for current embossing machines to

exert larger forces. However, when using a ramp force path, increasing the embossing

force means the increase of the process cycling time. In order to reduce the embossing

cycling time, it is best to use the minimal functional embossing force.

Thermal Cycling Time

The thermal cycling time, which determines the throughput of a micro embossing

process, is typically around 30 or 40 minutes for the machine set up in our lab. Fig1-5

shows that the heating and cooling times occupy more than 90% of the total cycling time.

Thus decreasing the heating and cooling times is the key to improving the process

throughput.

Comparing the two major commercial embossing machines, Jenoptick[27] hot

embossing machine 'HX' serials and EV Group[28] micro embossing machine EV

520HE, the first generation machine in our lab has longer heating and cooling time. A

group similar to our own, the bioMEMS lab of the University of Texas at Arlington [29],

has already worked towards obtaining an optimal heating time, and developing a method

for preventing hot spots and achieving uniform heating on the tool and the polymer. They

used a 'heating cartridge' approach that divided the polymer surface area into 5 zones.

They controlled the heat flux of the 53 different cartridges separately to achieve uniform

heating. By running a Finite Element Analysis simulation they obtained an optimal

heating time of about 3 minutes and a cooling time of around 2 minutes.

Temperature non-uniformity is another problem associated with the thermal

system of the machine. It is an important problem because it can greatly influence the

quality of the final product [29,30]. While both [29] and [30] recognized the importance

of this particular factor, neither of them actually performed experiments to evaluate how

the lack of uniformity affects the quality of the product. In [29], temperature uniformity

across an 8-inch polymer piece was within $3°$ C. In [30], the temperature uniformity was

maintained within $\pm1\%$ ($\pm2.25°$ C /$255°$ C) within a 4 inch wafer size. Since our first

generation machine only produces 2cm×2cm parts, the uniformity is not a big concern yet,

but our goal is to be able to produce parts 4 inches in diameter. Thus, the temperature

uniformity will be a major factor in achieving quality uniformity over the larger area.

The improvement of the embossing machine to decrease the experiment cycle

time is the priority for this research project. Initial exploration of the second generation

is studied in my early stage research, but is not a major part of this thesis. It is given in

Appendix I. Please refer to Mathew Dirckx master's thesis [31] for more detailed design

of second generation machine.

Die Fabrication

The patterned die is the primary manufacturing tool in the micro embossing

process. Its fabrication technique determines its surface finish, thermal and mechanical

properties. Variations in these qualities may have an impact on the embossed parts.

Esch[32] compared the parts made by dies fabricated with three different techniques: deep reactive ion etching (DRIE) of silicon, wet etching of silicon and SU-8 processing. The results of this paper show that the dies fabricated out of silicon are more resistant to tool wearing than those made with SU-8, but the surface finish of the silicon die is rougher than that of SU-8. Because the thermal expansion coefficient of SU-8 is close to that of the polymer, the feature distortion is minimized during the de-embossing process. Scallops are created on the side walls of the features on the dies made with DRIE process. The scallops create undercut for the embossed parts, and this makes it difficult to de-emboss the parts from the dies. This problem occurs more often when the aspect ratio is high. Since there is an angle of 54.7^0 for the side walls of the wet etching due to the inherent properties of the silicon wafer, it is easy to de-emboss the die from the polymer. The wet etching silicon produces irregularly shaped outside corners on the silicon, however, which is not desirable in the die design.

Therefore, silicon die made from DRIE stands out because of its resistance to wearing. This capability is crucial for cost reduction, throughput improvement and product reliability assurance of the process. If each step of DRIE is well controlled, the scalloping on the side walls can be minimized. Nickel or Cobalt [33] [34] coating of the die can additionally strengthen resistance to die wearing. Teflon film or spray [35] deposited on the die can lubricate the die surface and make the de-embossing process easier.

Dimension and Material Flow

Not only the fabrication of the die, but also the die design, can affect the part replication. Feature dimensions and the spacing between the features are the major die design parameters. Die features with a variety of different dimensions and spacing have been studied. Fig.1-6 shows the results of the experiments [36].

(a) Non Uniform Pattern Height

(b) Non Uniform Residual Layer Thickness

(c) Incomplete Pattern Replication
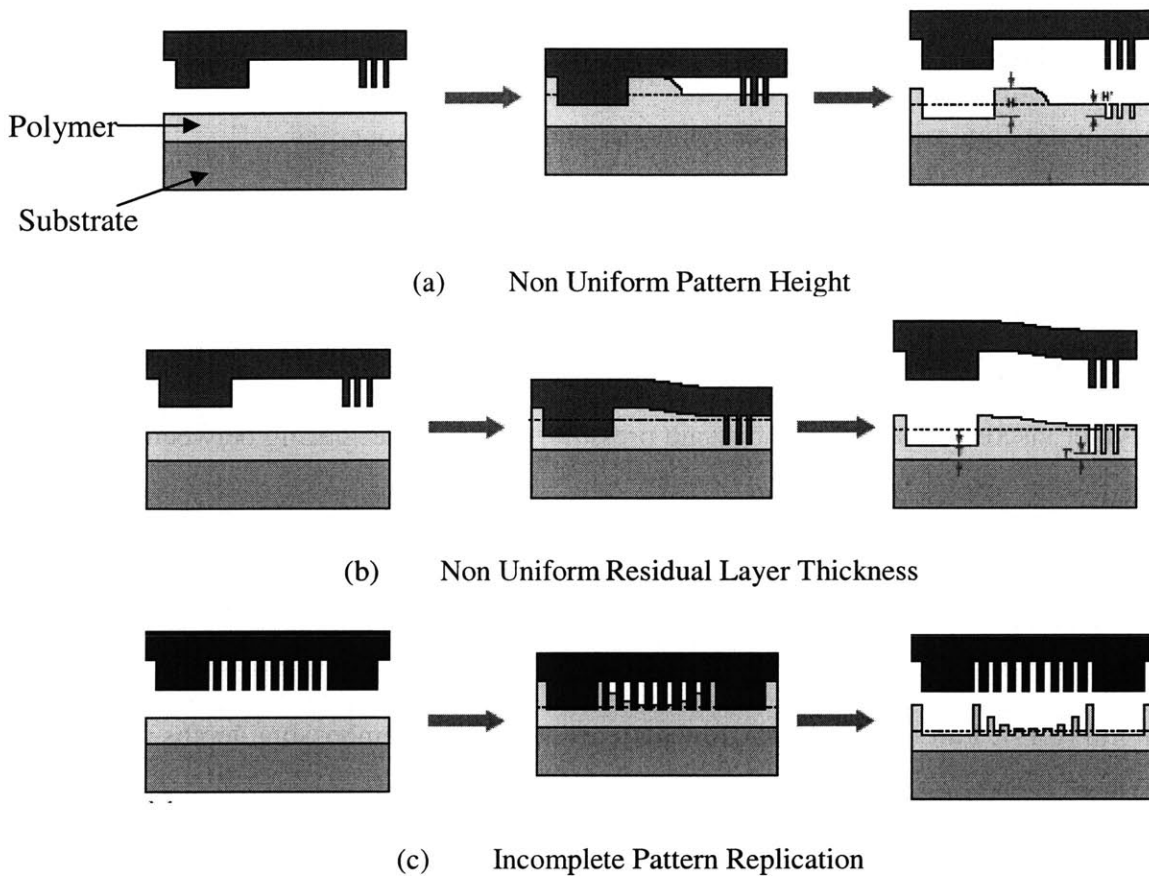
Figure 1-6 Die Dimension Impact on Part Replication (from [36])

Due to the viscous polymer flow and the lack of material of the polymer layer on the substrate, there are some cavities of the die that do not fill with polymer, as shown in Fig.1-6 (a). By decreasing the volume of the cavities close to dense features, as shown in Fig.1-6 (b), the cavities can be filled more completely. In Fig.1-6 (c), the dense and uniform design of the features leads to incomplete filling of the middle cavities. It is

foreseeable that the variance of the aspect ratio would affect the cavity filling as well [37].

However, currently, there are no strong conclusions to guide feature design quantitatively.

Similar research can be found in [38] and [39]. Some researchers investigated the

material flow both theoretically and experimentally to develop proper die design pattern

rules. This investigation normally starts with the research of the mechanical properties of

the polymer [40]. Based on the constitutive models of the polymer, theoretical

calculations are carried out. The time it takes to fill the die cavity is expressed as a

function of die dimensions, embossing pressure and polymer properties:

$$T_f = \frac{\eta_0 S^2}{2p}(\frac{1}{h_f^2} - \frac{1}{h_0^2}) \ , \tag{1-1}$$

where h_0 is the initial height of the polymer, h_f is the final height of the polymer, η_0 is

the polymer viscosity, p is the embossing pressure, and S is the spacing between

features[41]. This equation is applicable to die with uniform features.

Sometimes, instead of making theoretical models, researchers use experimental

data to build models of the flow pattern [38] [42]. The flow pattern measured in [38] is

shown in Fig.1-7. Part (a) shows the flow patterns at 9different embossing depths using

the color laminate substrate under isothermal embossing. This flow pattern resembles a

biaxial extensional flow. This flow pattern appears at a temperature of 140°C, and an

embossing pressure of 1.04×10^5 Pa. In the non-isothermal case, Fig. 1-7 (b), the die

temperature is 200°C and the polymer is at room temperature. Only the portion of the

polymer that is in contact with the mold insert can flow easily. Hence, the molten

polymer flows along the side wall of the mold feature and is compressed and spread out

once it reaches the surface of the mold.
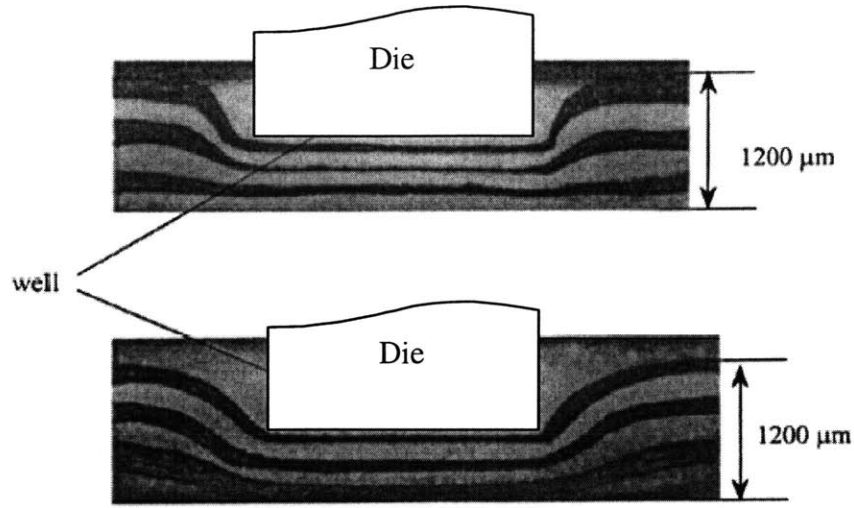
(a)   Isothermal Embossing
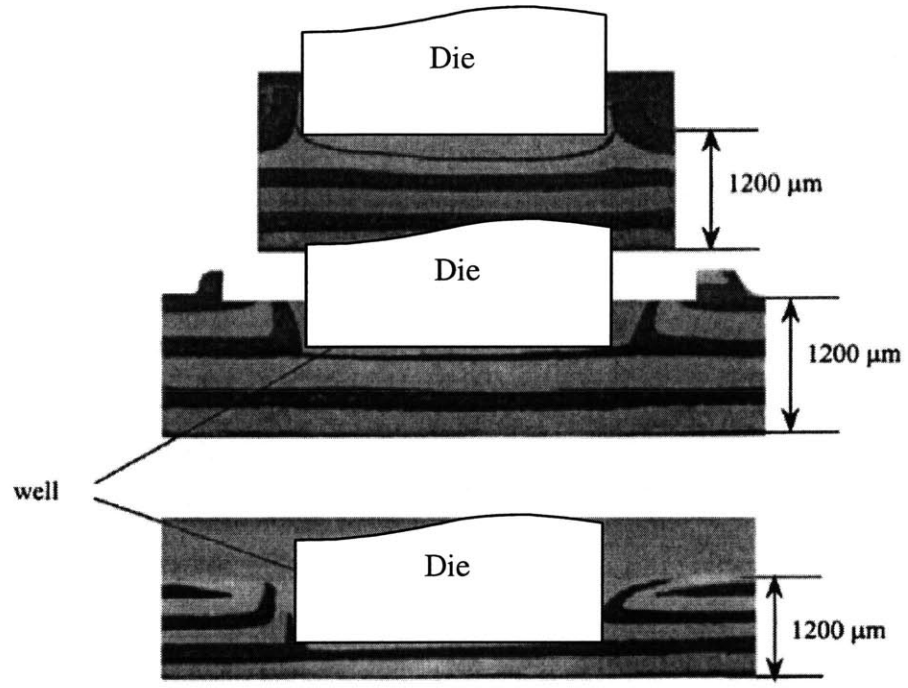
(b)   Non Isothermal Embossing

Figure 1-7   Flow Pattern of Polymer (from [38])

In order to predict the flow given a particular die design and set of embossing conditions without doing the experiment, finite element analysis (FEA) is imperative.

Some research work has been done in this area. Papers [42] and [43] did simulations using commercial FEA code DEFORM®. The simulated material flow pattern matches the experimental flow pattern well in the material filling stage. However, simulation of deformation of the embossed features during the cooling stage has not been studied yet.

This thesis will be primarily concerned with studying the flow pattern experimentally rather than through simulations. More literature review on polymer flow patterns and their theoretical study is given in Appendix II of this thesis, and some simulation results are included.

Multilayer

For many applications, particularly integrated circuits, multilayer micro embossed parts are essential. Unger [13] successfully demonstrated the manufacturing of microfluidic on-off valves, switching valves and pumps using a micro casting process. There is no relative movement between the featured die and the polymer in micro casting, so the alignment of layers is ensured.

However, in the micro embossing process, ensuring the alignment accuracy between the moving die and the static polymer is an inevitable problem. For a parallel anvil embossing system, a large and uncontrollable relative shift and rotation between the die and polymer is observed [44], as shown in Fig. 1-8. The reason for the misalignment is that the moving anvils and the fixed anvil are not exactly parallel, which leads to none uniform pressure over the anvil, and this results in rotation and relative position shifts. There are two options for solving this problem: make an embossing machine that does

not cause the relative shift and rotation, or dynamically align the die and the polymer.

The first solution is adopted in [44].
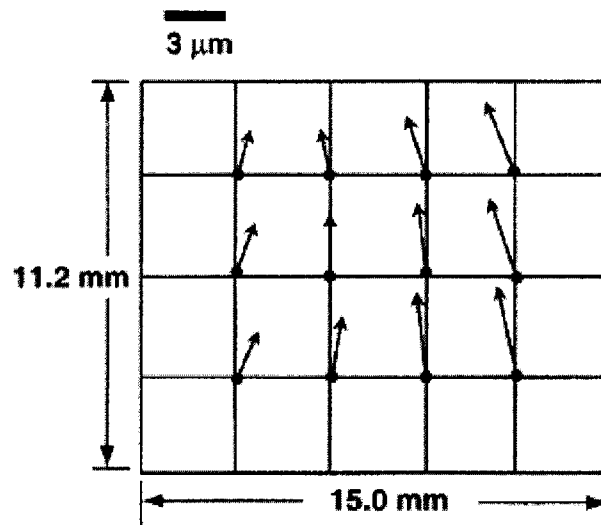
Figure 1-8   Misalignment Map of Relative Shift and Rotation (from [44])

The new design of the embossing machine in reference [44] results in a half micro

alignment accuracy in a 4 inch area. Obviously, the new design of the machine requires

an investment in new hardware. The dynamic self alignment mechanism has yet to be

developed.

Quality Assessment

In the research review presented above, it is clear that researchers have broadly

explored the micro embossing process. Many micro fluidic and optical instruments have

been embossed successfully. In order to determine the success of these experimental

embossing processes, many imaging and measurements have been done to evaluate the

quality of embossed parts.

The basic imaging approaches are Atomic Force Microscopy (AFM) imaging and

Scanning Electron Microscopy (SEM) imaging. Heyderman [46] freezes the filling flow

of the polymer material into the cavities, and observes the state of the polymer under AFM to obtain the basic flow pattern.   Fig. 1-9 shows the results of this process with different embossing parameters.
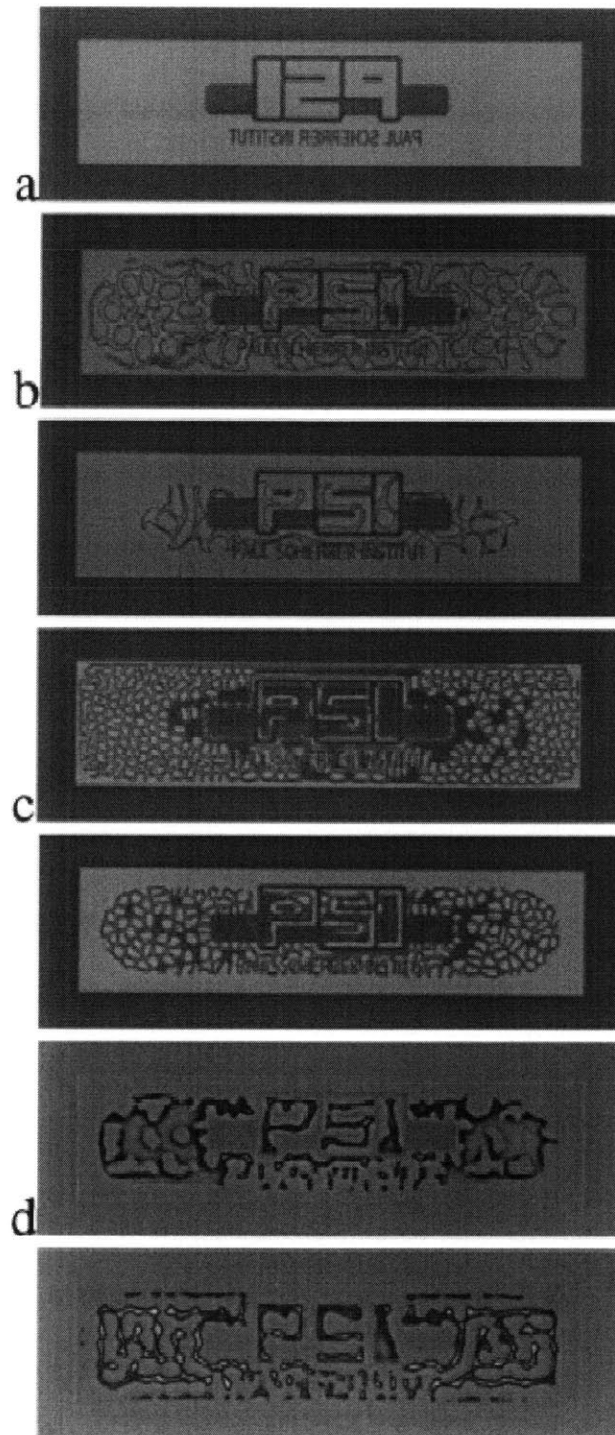
Figure 1-9   AFM Images of Embossed Features (from [46])

These images are: (a) stamp with Paul Scherrer Institut Logo design and corresponding embossed polymer showing complex filling: (b) 100 nm thick 25 kg/mol PMMA, $T = 170\,°C$, $F = 150\,KN$, $t = 10\,min$, (c) 100 nm thick 75 kg/mol PMMA, $T = 200\,°C$, $F = 150\,KN$, $t = 2$ min and (d) 385 nm thick 75 kg/mol PMMA, $T = 150\,°C$, $F = 150\,KN$, $t = 15$ min. These images provide a visual assessment of how well the embossing process has worked, but it is hard to describe the image without quantitative presentation.

More detailed images can be obtained using SEM shown in Fig. 1-10 [46].
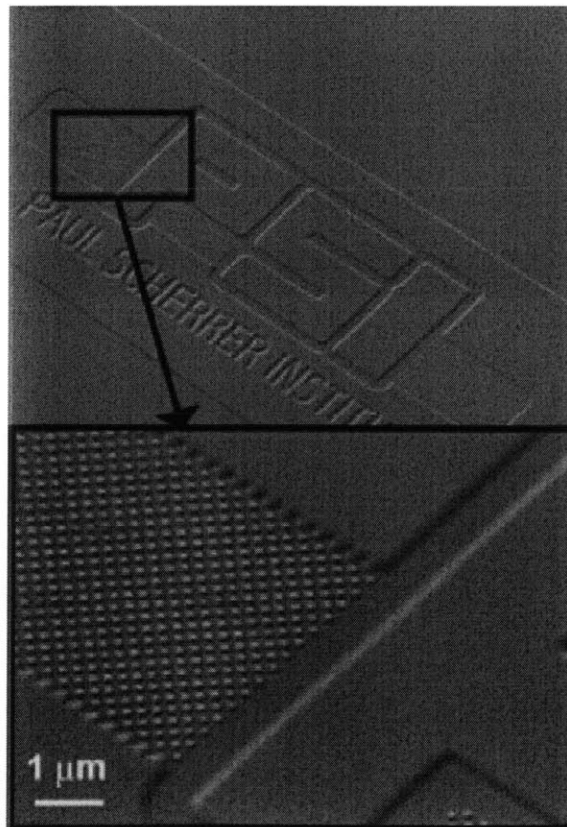
Figure 1-10   SEM Images of Fully Embossed Feature (from [46])

SEM images are capable of bigger magnification. There are triggers available to do some simple dimensional measurements, but SEM does not provide numerical data for each pixel in the picture. The three dimensional effect strongly depends on the measuring

angle, which means that some feature details can only be captured in specific orientations. Because of this orientation problem, measurements can only be approximate.

Other than the imaging and simple dimensional measurements, birefringence pictures are also taken to show the residual stress patterns in the embossed parts, shown in Fig.1-11 [26]. The birefringence pattern assists the selection of the embossing temperature and part quality.
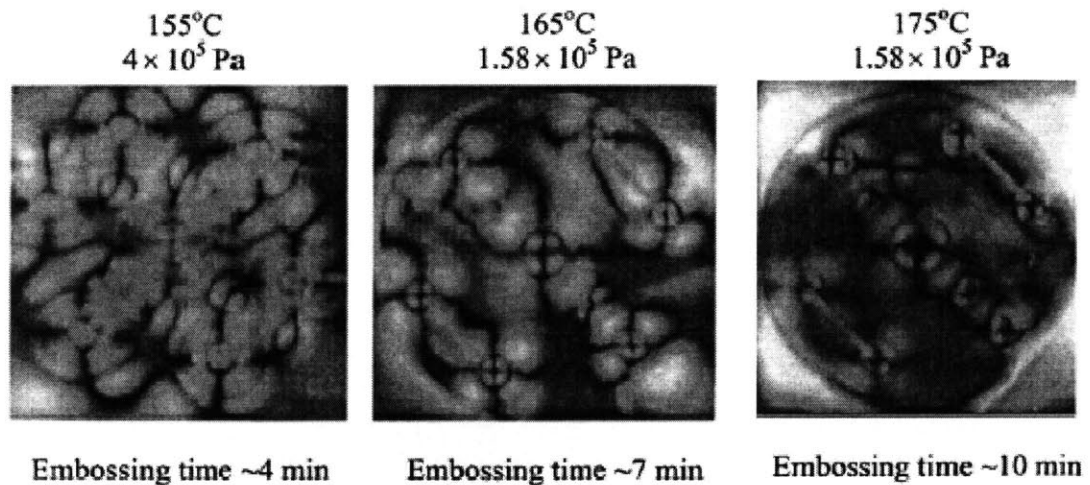
Figure 1-11   Birefringence Pattern in Molded PC Parts (from [26])

1.3   Research Focus

Section 1.2 gives background on the application and manufacture of micro devices. Several potential micro manufacturing processes are introduced. Based on the analysis of the pros and cons of those processes, micro embossing process stands out as a promising manufacturing approach.

Much research has been done in exploring the micro embossing process in order to increase its productivity, improve the part dimensional accuracy and residual stress by choosing the right process parameters.

However, some fundamental problems of the micro embossing process are unsolved:

1. Is there a systematic quality assessment criterion for the embossed parts?

2. Is there a measurement instrument that can provide numerical data indicating part quality?

3. What are the optimal embossing and de-embossing temperatures?

4. What is the minimal embossing force required for a given design and how does it vary with different designs?

5. What is the proper embossing speed that minimizes embossing cycling time while maximizing product quality?

6. As a mass production micro manufacturing process, what is the process capability?

These questions will be answered in this thesis.

1.4 Thesis Layout

This thesis consists of six chapters. The first chapter talks about the background and the research motivation of this thesis. The experimental set up will be described in Chapter 2. That will be followed by the development of the protocol to extract dimensional data for assessing the product quality. In order to balance the trade off between part quality and process productivity, the processing window is identified in

Chapter 4. Within the range of the processing window, embossing experiments are repeated and process capability is studied in Chapter 5. In Chapter 6, conclusions of the whole research work are drawn, and future work is discussed.

The initial consideration and experimental work of embossing machine system modification will be given in Appendix I. Theoretical model and experimental simulations of the material flow into die cavities is given in Appendix II.

2

Experimental Set UP

2.1 Introduction

Micro embossing process is a promising micro chip manufacturing process, during which polymer deforms and conforms to the featured die under pressure at a temperature above polymer glass transition temperature. By separating the embossed polymer from the die at a temperature below the glass transition temperature at the end of this process, an embossed part is obtained. The equipment for this process comprises two sub systems: a compression sub system and a thermal sub system. When embossing products are produced, metrology equipment provides the initial quality assessment data.

In this chapter, the design, manufacturing and set up of the equipment of the hot micro embossing process will be described. The choice of metrology instruments will also be discussed.

2.2   Compression sub system

2.2.1 System Introduction

There are some commercial integrated systems available for the micro embossing process, such as the Jenoptick hot embossing machine 'HX' serials [27], and EV Group [28]. However, because of machine cost most of the laboratory embossing process set ups choose standard material testing machines to exert and control embossing force, such as the bioMEMS lab of University of Texas at Arlington[29] and Department of Chemical Engineering of Ohio State University [26].

In our lab, Ganesan [47] initially designed and assembled our embossing system, shown in Fig. 2-1 the Instron 5800 series machine was chosen to be the force and displacement control element because of its fine force and displacement control capability. Two load cells with different force ranges (1KN and 50KN) are available to adapt to different die design. The measurement accuracy is $\pm 0.04N$ and $\pm 2N$ for them respectively. The displacement accuracy is $\pm 0.02mm$.

2.2.2 Control Console

An integrated set of software supplied with the Instron machine, including a control console and application development tool Merlin, play the role of machine human interface, shown in Fig. 2-2.
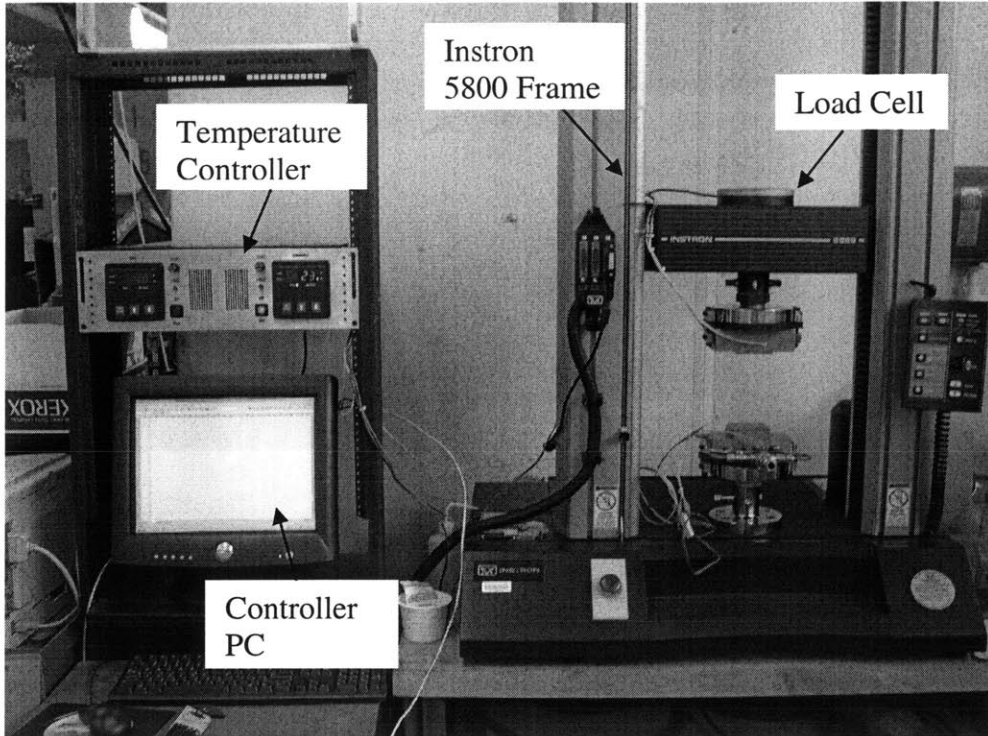
Figure 2-1 Micro Embossing Machine Set Up
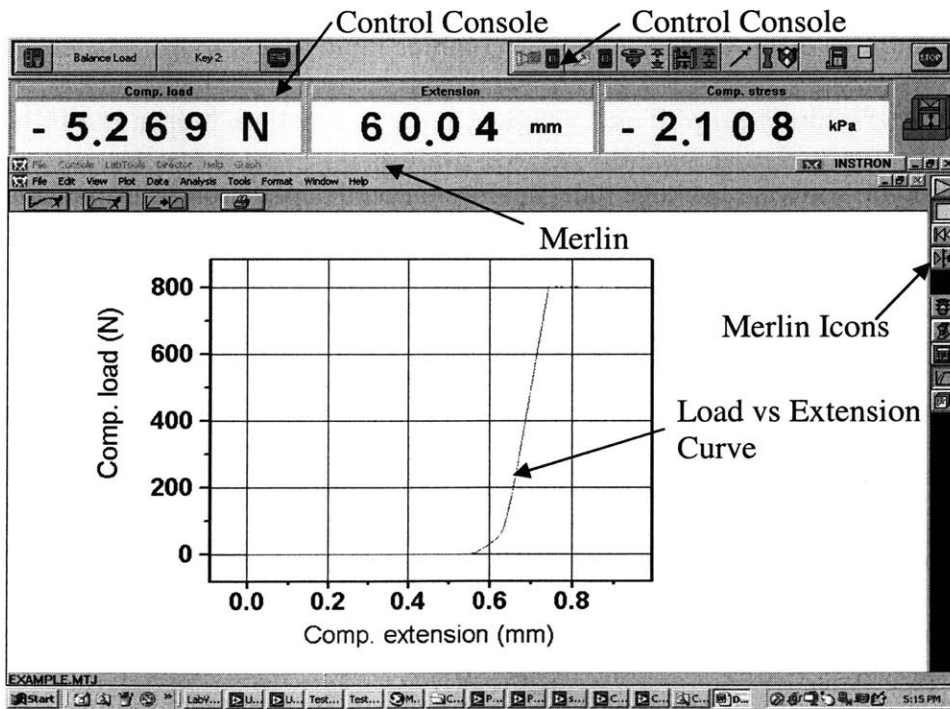
(a) Instron Console and Merlin Interface
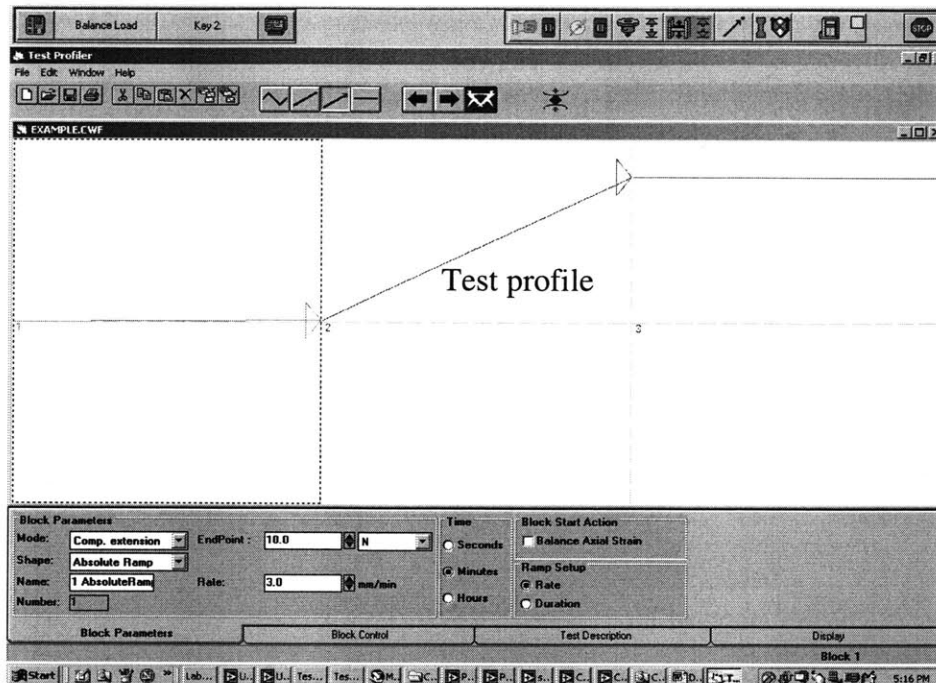
Figure 2-2   (b)   Merlin Test Profiler

The control console is the home base for setting up system parameters, transducers, and live displays. The icons can combine rapid access to transducer settings, system parameters, limits etc with an 'at-a-glance' status situation. Merlin is a fully integrated module software package that provides tailored application solution for a wide range of static and cyclic tests. It enables the design of the test profile with diverse control methods and paths, shown in Fig. 2-2(b). It records and presents the experimental data, shown in Fig. 2-2(a).

Instron machine has two different control modes: force control and extension control. In force control mode, the control system controls the force to follow a path designed in Merlin. Alternatively, a displacement path can be specified and followed. . Fig. 2-3 shows the relative extension of the embossing anvils and the working piece (PMMA) under the two control modes.
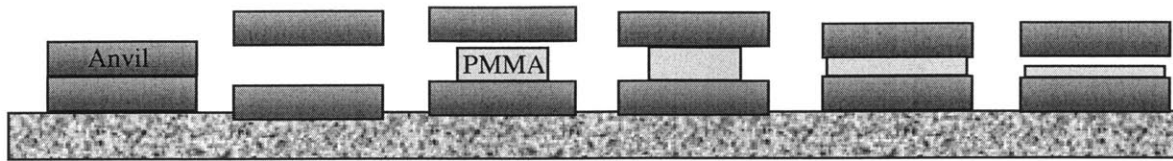
Figure 2-3 (a)   Relative Extension of Anvils and PMMA under Extension Control
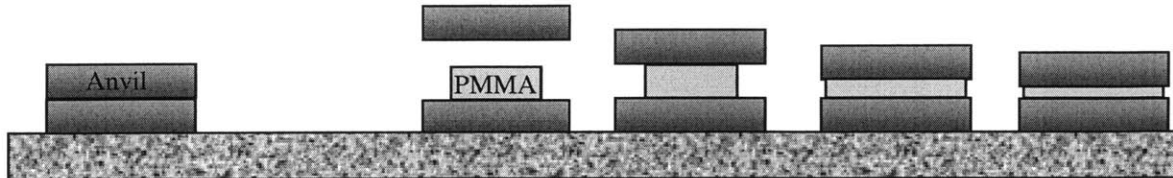
Figure 2-3(b)   Relative Extension of Anvils and PMMA under Force Control

At embossing starting stage, the movable anvil is moving toward the fixed anvil under extension or force control until it reaches the 'touching criteria'. The 'touching criteria' in both force and extension control mode is either a preset contacting force between the movable anvil and PMMA or a preset extension of the movable anvil. Under the preset force, the movable anvil is assumed to have good contact with the PMMA. The preset force is determined based on the calibration of the anvils and the estimation of the thickness of the PMMA at embossing temperature.

Preliminary embossing experiments are done to explore the appropriate control mode at embossing starting stage. A force versus time curve of an embossing process is shown in Fig. 2-4. This curve is obtained under force control mode. It shows that there is a force overshoot when the force approaches the 'touching criteria', which is 2N in this experiment. When the force increases suddenly from 2N to 20N, there might already be some polymer deformation. After that, the force decreases back to 2N again, which leads to withdraw of extension of the movable anvil, and these results in the back flow of the deformed polymer. After this, the polymer deforms again with increasing force. In this whole process, the polymer is deformed twice, which is not consistent with the definition

of the embossing process. This problem does not occur under extension control mode. Therefore, in order to get a consistent embossing process, extension control should be applied at this starting stage.
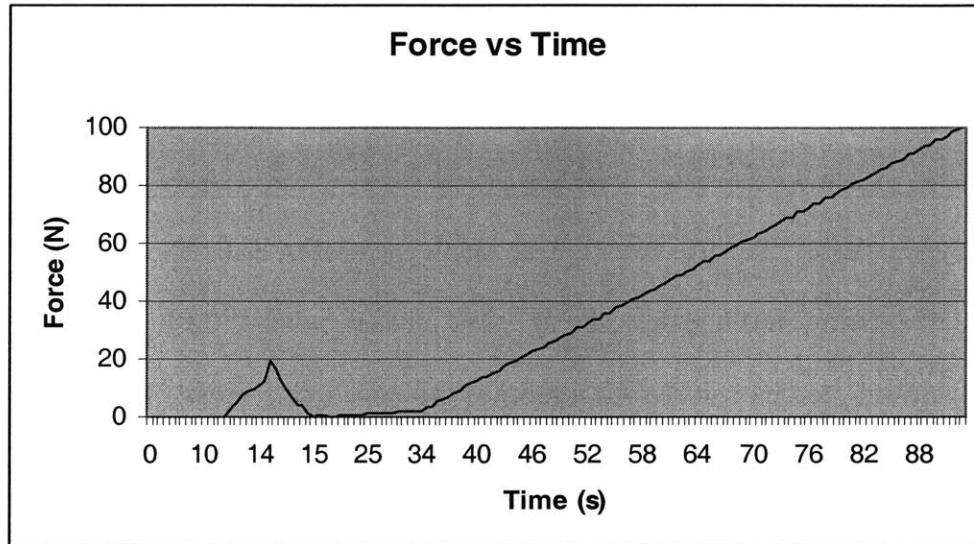
Figure 2-4   Embossing Starting Stage under Force Control Mode

Pure compression tests with only Instron machine anvils (without PMMA in between) were done under both control modes to evaluate the applicability during embossing stage. Fig. 2-5 records the force-extension relationship of the anvils. The Instron machine frame deforms around 0.2mm under a force of 800N; hence the compliance of Instron machine frame is not negligible. This means the extension reading does not represent the absolute relative displacement of the anvils during the embossing stage. Because of this, because of the limited 20 micron displacement accuracy and because of the potential for polymer relaxation under load, force control should be applied in the embossing stage.
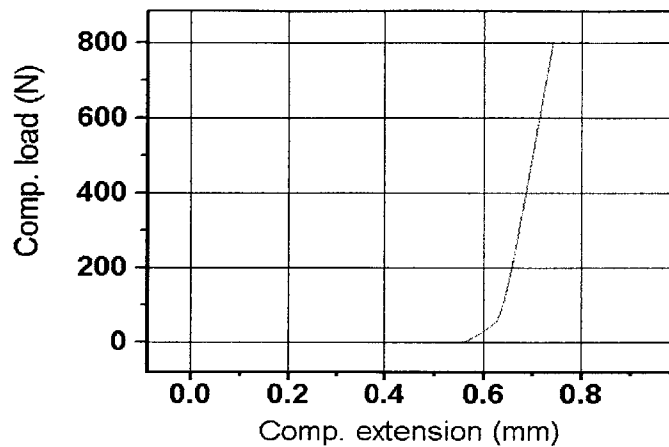
Figure 2-5   Instron Machine Frame Load Extension Curve

At cooling stage because it is hard to estimate shrinkage rate and total shrinkage

of PMMA, the movable anvil is normally held stationary in extension control mode. By

contrast, while in force control mode, the force between the movable anvil and the

PMMA remains constant. As a result, the surface of the PMMA shrinks freely during

cooling under extension control mode, but stays in control under force control mode.

Therefore, during cooling, force control should be applied.

In conclusion, extension control should be applied during the starting stage, and

force control should be applied during the embossing and cooling stages.

2.2.3 Control Console Output Data

The console records force and displacement simultaneously at a frequency of

5kHz. A set of data is recorded, and can be extracted into a spread sheet. A force versus

extension figure is the best way to present the recorded data, shown in Fig. 2-2(a). There

is first a long extension of the anvil with zero force. A curve with changing slope follows

afterwards, which records the characteristics of the embossing process. During the

holding and cooling cycle the motion is very small, so we must look at the detailed data

to determine holding time, holding extension, cooling time and cooling extension.

2.3 Thermal sub system

2.3.1 System Introduction

The thermal system heats the featured die and polymer to a specified embossing

temperature, and then cools the die and polymer to a desired de-embossing temperature.

This thermal cycle occupies 90% of the whole embossing process cycle time, and hence

reducing the thermal cycling time is a key to reduce the process time, which directly

relates to the manufacturing productivity and cost.

Researchers in different labs have examined this issue [27] [28], and the solutions

falls into three categories:

1. Use a concentrated heat source to heat up the die and polymer, and cool down the

   die and polymer naturally in ambient air.

2. Use a concentrated heat source to heat up the die and polymer, and use fluid to

   accelerate the cooling time.

3. Use fluidic heating and cooling to heat up and cool down the die and polymer.

   Ganesan [47] designed and assembled a thermal system in his thesis, shown in Fig.

2-1. Cartridge heaters were chosen as heat source. Since the heaters are concentrated in

one small area and can get very hot, calculation was carefully made in order to assure

uniform temperature distribution. This resulted in a selection of four 200W heaters and a

copper block of around $14\times6\times6$ cm^3. Four parallel channels were designed to flow city water to assist the cooling of the copper block. The design details are shown in Fig. 2-6.
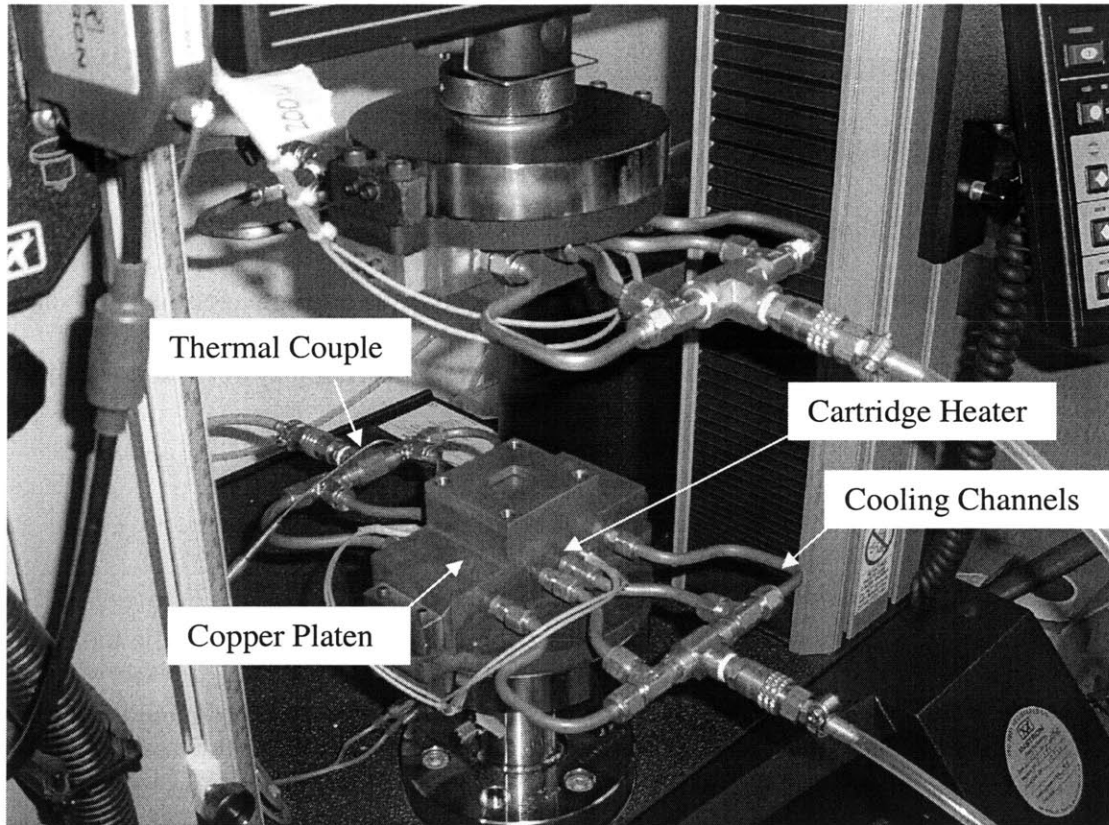
Figure 2-6   Details of the Thermal System

During the heating time, the copper platen is heated up from room temperature to an embossing temperature, which could vary from 10 to 60 ^{0}C above the PMMA glass transition temperature. The heating time is around 10 minutes. During cooling, the copper platen is cooled down to 20 to 50 ^{0}C below the PMMA glass transition temperature. The cooling time is around 30 seconds. These are the data of our first generation thermal system. Mathew Dirkx [31], Grant Shoji [51] and Kunal Thaker[52], designed a second generation thermal system, which adopts the fluidic heating and cooling method and shortens the heating time by a half to two thirds compared to the first generation thermal system while increasing the embossing area to 4 inch. The second generation thermal

system also enables the control of heating and cooling rate. In this thesis, first generation machine is used.

2.3.2 System Control

The Chromalox controller, cartridge heaters, and the thermal couples that embedded in copper platen form a closed thermal control loop. This first order system can assure $\pm 1^0C$ temperature accuracy. However, because the cooling agent is city water, and it can not be included in the control loop in the first generation system, and it is hard to control the cooling rate and the exact de-embossing temperature.

2.3.3 Thermal Control Output Data

The first generation thermal system does not have temperature and time data acquisition capability. By recording the temperature of the copper platen manually, the open loop heating curve is obtained and it is shown in Fig. 2-7. It shows that the open loop steady state temperature is around 280 °C, and the time constant is 20 minutes.
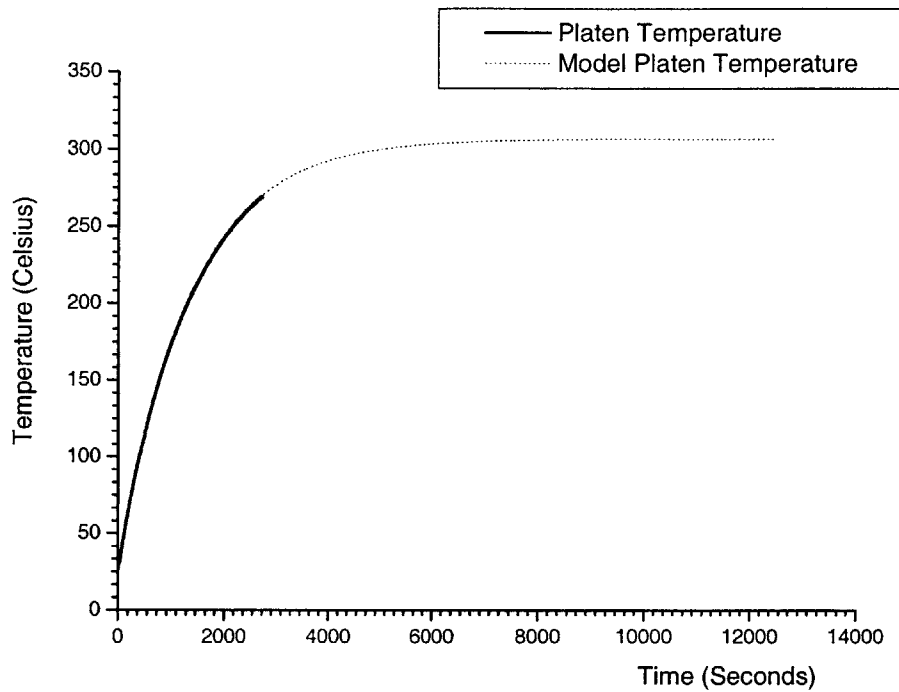
Figure 2-7   Open Loop Heating Curve

Because of specific historic problems, the top copper blocks has bigger thermal masses than the bottom one. This discrepancy results in a faster temperature rising speed of the top copper block than that of the bottom one during the heating cycle. Thanks to the controller, the temperature of both copper platens can reach the same embossing temperature at some time point. The discrepancy of cooling speed and temperature of the copper blocks also exists during the cooling cycle. However, because of the lack of control of the cooling speed and temperature, the temperatures of the top and bottom copper blocks will not be the same when the parts are de-embossed from the die. The average of the two temperatures is defined as the de-embossing temperature in this thesis.

2.4 Die Design

2.4.1 Die Material Selection and Manufacturing

Potential die materials include silicon, nickel, copper and aluminum. Selection of the die material is based on the resistance to wear, the easiness of de-embossing and the manufacturability of the tool.

Silicon and nickel dies are normally fabricated in a clean room, and they are more expensive than other die materials. Deep Reactive Iron Etching (DRIE) is a common approach to manufacture micro features on a silicon wafer [32]. In order to increase the resistance to wear, nickel can be coated on the silicon wafer [48]. If the nickel layer wears, the base can be cleaned and recoated. Both silicon and nickel dies can have good surface finish. However, because of the inherent properties of the DRIE process, scallops on the side-walls of deep features are created, which makes de-embossing difficult. Teflon film or and anti-adhesive spray can be added to the dies to help de-embossing [35].

Copper and aluminum can also be used to manufacture embossing dies using a CNC machining process. Due to dimension constraints of typical CNC machine tools, individual features of a die can be as small as 100 microns, but the smallest spacing between features is typically 200 microns. The depth, on the other hand, can vary in a pretty wide range from 20 to 300 microns. This leads to the possibility of manufacturing features with low aspect ratios. However, obvious machining marks and burrs will be observed on the die surface. The surface roughness is demonstrated to be around 3 microns in the later sections of this thesis. This is a drawback of manufacturing embossing dies using conventional CNC machining tools relative to lithography processes.

2.4.2 Die Design

Ganesan[47] studied the embossing process with his silicon die with 'MIT' logo. Those features are around 100μm width and 1μm depth [47]. Other than an 'MIT' logo feature, the features in this thesis will be simply straight channels, which are more representative for commercial micro chips. The size is bigger as well, and it is designed to be 500 microns in width and 50 microns in depth. The die design is shown in Fig. 2-8.

(a) Featured Die   (b) Base Die

PMMA

(c) Relative Position of Copper Die Pair and PMMA
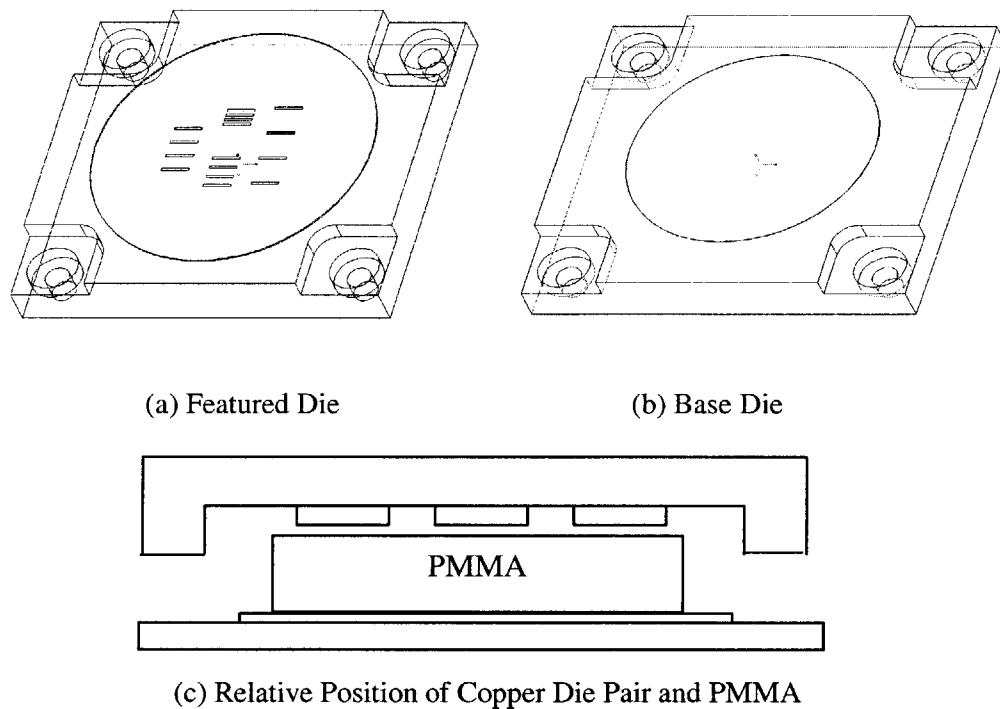
Figure 2-8   Die Pair Design

This die pair comprises a base and a die. All the channels are 500 microns wide, but with different spacing, varying from 3×, 5× to 10× of the channel width, which enables the study of the impact of the spacing on the embossed part quality. Because the size of the features falls into the CNC machining category, the die pair was made of copper on a Bridgeport Toro-Cut TC3 CNC machine. The edges of the base and the die are carefully machined to so as to assure the parallelism of the die pair.

2.5   Polymer Material Selection

The traditional working material is Polymethylmethacrylate (PMMA). This material has the advantages of low glass transition temperature, good optical properties, biocompatibility, hydroscopic properties, thermal mechanical properties, and low cost. These properties make PMMA stand out and it becomes a strong candidate for micro embossing of micro fluidic, bio microelectronics, and optical devices.

The most general form of the workpiece is PMMA thin film that is deposited on silicon substrate [36]. Because of the constraint of deposition time, a small film thickness, normally on the order of 100 micron, is desired. However, many researchers have reported the lack of material in the embossing experiments with thin films. If the thickness of the PMMA film is increased to 1mm, which can be considered as infinite thickness relative to the depth of 50-100 microns, that lack of material problem will not exist anymore. Thus, in this thesis, the working material is 1mm thick off-the-shelf PMMA sheet. Corresponding to the specific die design, our working piece is 30 mm in diameter. Fig. 2-9 shows a typical embossed part.
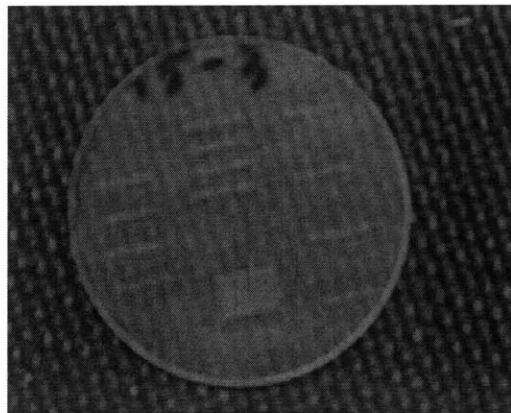
Figure 2-9   Embossed PMMA Part

2.6 Measuring Instruments

In order to assess the quality of embossed parts, quantitative measurement of the parts must be done. One of the most important criteria of assessing the part is dimensional accuracy. So, the primary requirement of the measuring instrument is the ability to quantify the geometry profile of features. Microscopes, Atomic Force Microscope (AFM), Scanning Electron Microscope (SEM), contacting profilometers, and optical interference profilometers are all potential measuring instrument candidates.

2.4.3 Optical Microscope

An optical microscope, M2 LabScope, is a two dimensional imaging tool, that can tell the width of the channel approximately with the magnification number and the scale marked on the microscope table. Likewise, but changing the plane of focus it is possible to get the approximate depth of a channel.
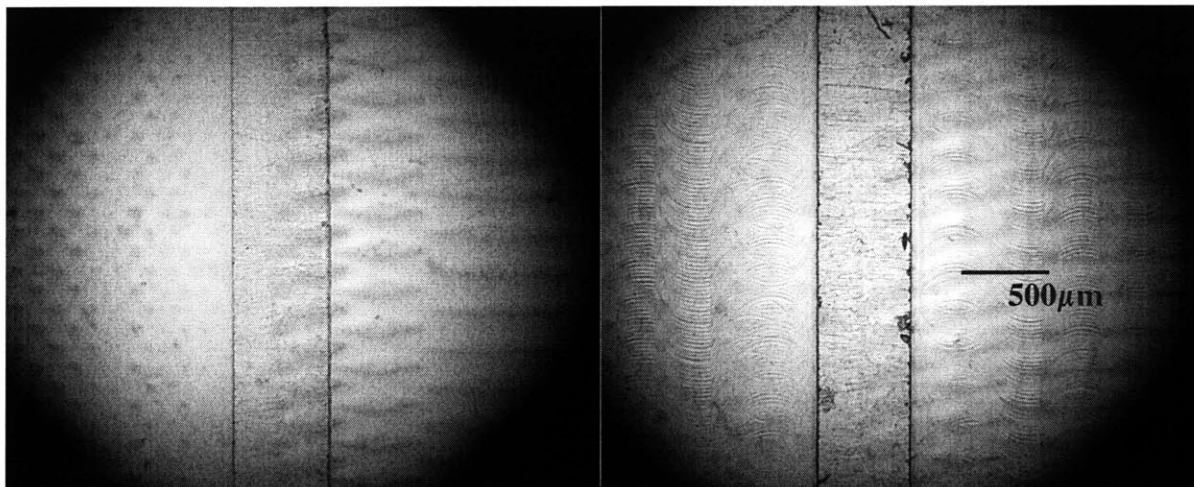
(a) Partially Filled Channel   (b) Fully Filled Channels

Figure 2-10   Optical Microscopy Image of Part Channels

Fig. 2-10 shows the picture of two embossed parts under the microscope. Some qualitative evaluation can be obtained by using the microscope. For example, the channel edge in (a) is not as clear as that of (b). Also, in (a), there are not obvious machining marks in the rest of the area other than the channel, whereas, machining marks beside the channel in (b) part are clearly observed. This shows that (b) is better formed than (a) as it was in full contact with the die in all regions.

2.5.2 Atomic Force Microscope

The Atomic Force Microscope (AFM) is a mechanical contacting profilometer, which operates by measuring atomic level attractive or repulsive forces between a probe and a sample. AFMs can achieve a resolution of 10pm in the vertical dimension. Fig. 2-11 shows the AFM image of parts made in Ganesan's thesis [47].
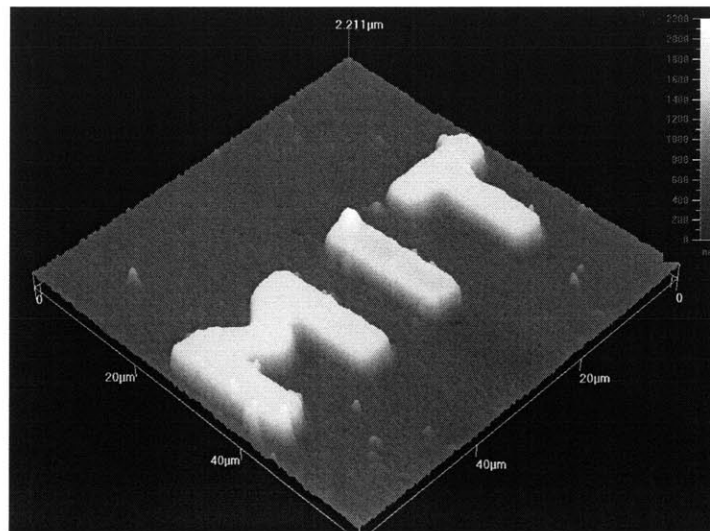
Figure 2-11   AFM Image of a Part with Features of 10μm Wide and 1μm Deep (from [47])

The scan range varies with the design of the AFM. The AFM that our lab has access to(Quesant Q-Scope Model 250) only measures features in a range of around 80 microns in width. This measurement capability does not fit the features considered in this thesis. Because the measurement of AFM is a serial process, it takes around 40 minutes to measure a whole part such as shown above.

2.5.3 Environmental Scanning Electron Microscope (ESEM)

The Environmental Scanning Electron Microscope (ESEM) is a very popular instrument to image transparent polymer parts three dimensionally. An example is the Philips/FEI XL30 FEG-SEM. It is good for visual qualitative assessment, but it is not a quantitative measurement, and cannot be used for precise process metrology. However, as shown in Fig. 2-12, it does clearly show surface is finished and details that demonstrate where the material contacts the tool and where it does not.
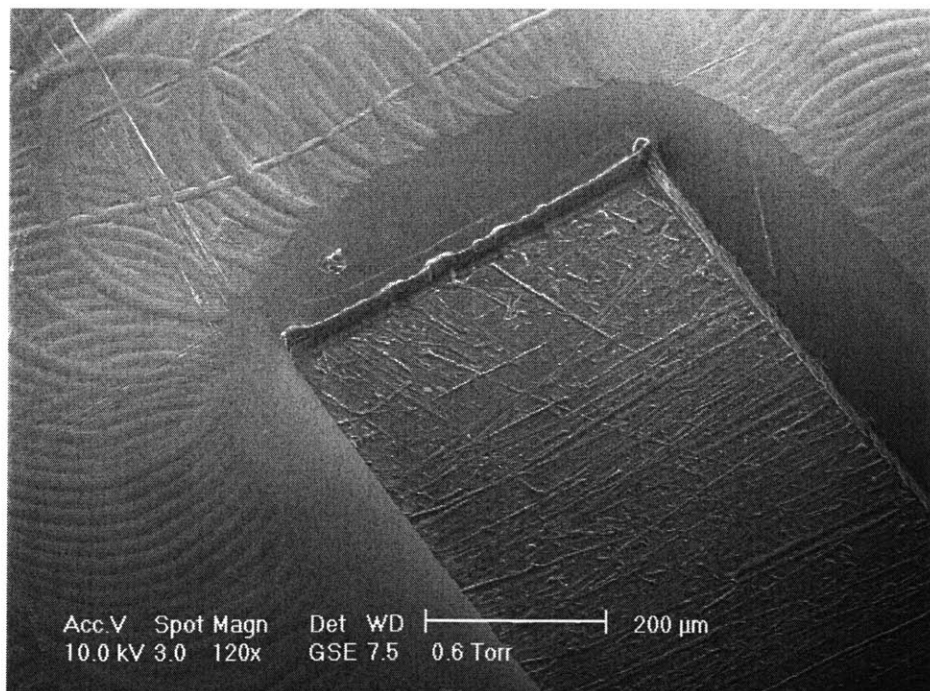
Figure 2-12   ESEM Image of a Part Channel

2.5.3 Contacting Profilometer

A Tencor profilometer (Tencor P-10 surface profilometer) is also a potential candidate to measure the exact profile of a cross section. This instrument is mainly used to measure step heights and to view the surface of the processed device microscopically. Similar to the AFM, the Tencor profilometer is a contacting profilometer. The dimension of the stylus is small with respect to that of the part channels, so that it is possible to get a good quantitative profile of the channels, as shown in Fig. 2-13. However, like many other serial measuring instrument, the profilometer is very slow in mapping the 3D image of the entire profile of a channel. It normally takes more than an hour to map a 3D image for a channel on my embossed parts.
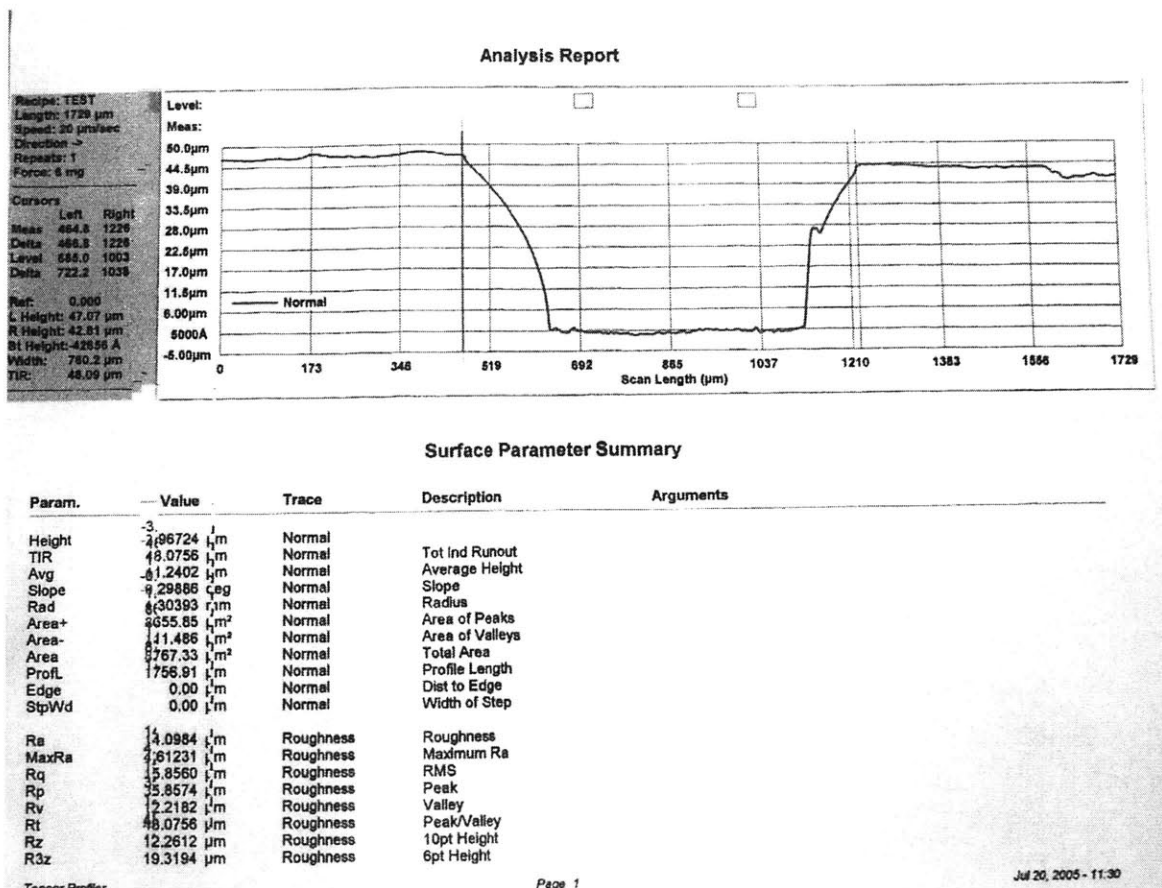
Figure 2-13   Tencor Image of a Part Channel

2.5.4 Optical Interferometer

The optical interferometer Zygo (Zygo Newview™ 5000) is an interferometer based on scanning white-light. It is a technique in which a pattern of bright and dark fringes result from an optical path difference between a reference and a sample beam. Incoming light is split inside an interferometer. One beam goes to an internal reference surface and the other goes to the sample. After reflection, the beams recombine inside the interferometer, undergoing constructive and destructive interference and producing the light and dark fringe pattern.

Fig. 2-14 is an example of the interferometer measurement of a channel in a well-formed PMMA part. The upper right picture is the three dimensional image of a channel. It shows that the scan width is 1.44mm, and the length is 1.08mm. The scan picture resolution is 640×480 pixels in the scan area. There are quantitative coordinate values associate with each pixel. Because of the limitation of the dimensions, the object magnification of this measurement is set to be 2.5×. In this configuration, the lateral measurement resolution is $5\mu m$, and the vertical measurement resolution is 1nm.
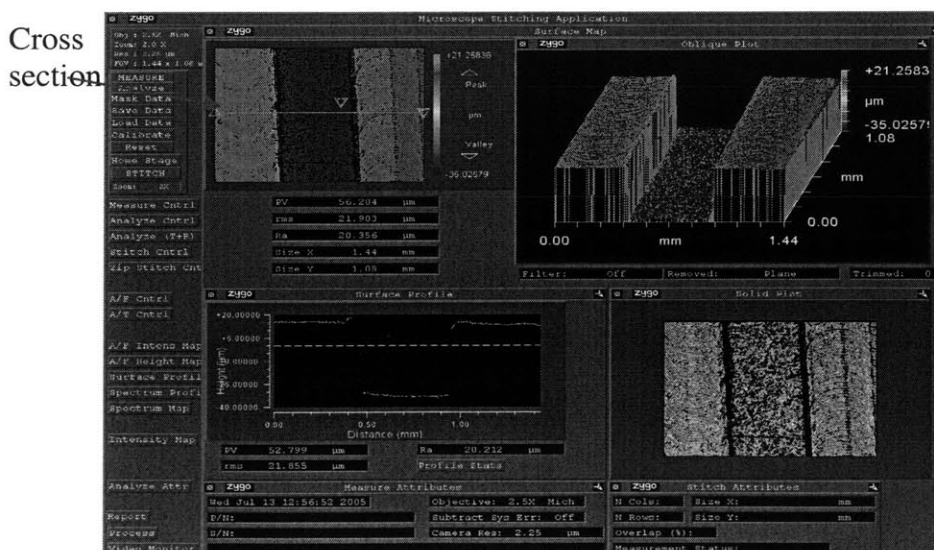
Figure 2-14　　　　Optical Interferometer Image of a Part Channel

Different colors in Fig. 2-14 show different depths of the part surface. The bottom left sub-figure is the surface profile picture, and it shows the profile of the cross section that corresponds to the cross section line in the upper left sub-figure. Black bands around the channel are observed where the profilometer receiver can not see the reflecting beams. Also, some black spots within the colorful area are observed indicating no data in the black area as well. Thus, in this measurement, some information is lost. This drop-out from sloping walls is one of the biggest drawbacks of this measurement approach.

The scanning time of the measurements depends on the depth of the channel, and for the scans used in this thesis is around 34 seconds. Compared to other metrology processes, the optical interference profilometer has the advantages of being fast and quantitative. These advantages make it the main measuring instrument in this thesis, and all the quantitative analysis is based on the analysis of these measurements.

However, the quantitative data recorded in the measurements does not provide the desired part feature dimensions (i.e. depth and width) directly. For this, a data processing protocol needs to be developed to extract the feature dimension information.

3

Dimension Quality Assessment Protocol

3.1 Introduction

There has been much research on applications and laboratory feasibility of the micro embossing process. However, proper quality evaluation is also essential in order to improve the accuracy and capability of micro embossed products. Accordingly, developing a systematic quality assessment criterion is imperative.

The dimension accuracy of embossed parts relative to the embossing dies is one of the most important of all qualities that ensure functioning of micro devices. In chapter 2, the Zygo interferometer was is chosen to measure embossed parts because it is fast and provides quantitative data. However, the raw data recorded by this device does not directly provide useful dimensions of the embossed features. For that a data processing protocol needs to be established.

In this chapter, details of the raw interferometer data are described, and the development of a data processing protocol is established.

3.2 Measurement of Part

The Zygo optical interferometer is chosen to conduct quantitative measurements. In order to keep consistency, the same region of the embossed parts is measured each time. That particular region is shown in the red circle of Fig. 3-1. This particular location is chosen because the channels that are close to the circled channel are at a sufficient far distance from it, so that the replication of the feature next to it will not be affected.
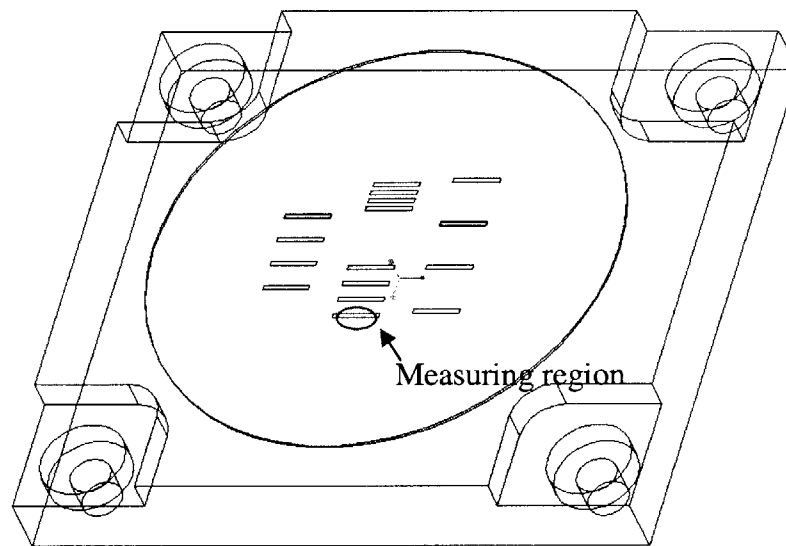
Figure 3-1   Measuring Region of Part

In order to maximize the accuracy of the measurements, the highest possible screen resolution for the interferometer, 640×480, is selected, and an object length of 2.5× is set. The measurement plot is shown in Fig. 3-2. From the upper right sub-figure, the horizontal axis shows that the figure covers a width of 1.44mm, and a length of 1.08 mm. The whole length of a single channel is around 5mm, and hence each channel is divided into 5 non overlapping regions. In later discussion, it will be shown that the

middle segment of the channel will be measured and the analysis in this thesis will be based on these measurements.
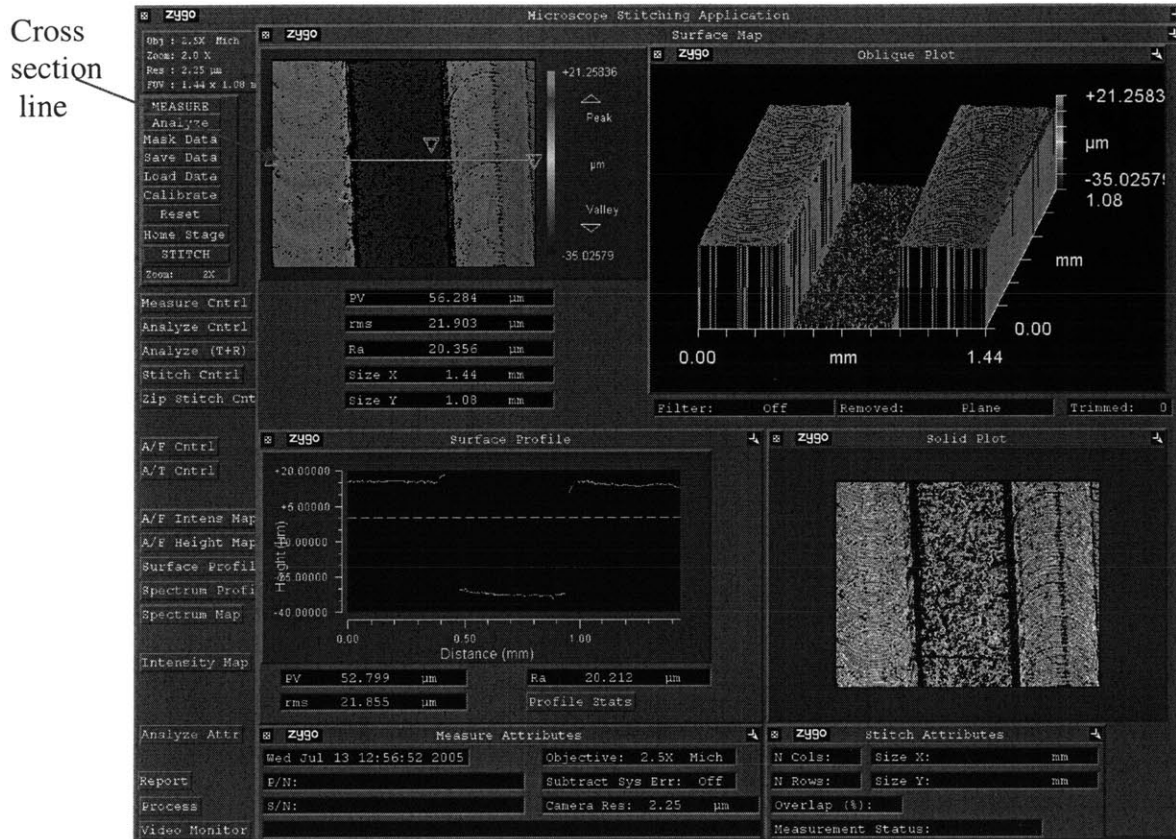
Cross section line

Figure 3-2   Zygo Figure of a Middle Segment Channel

3.3   Channel Data Extraction

The green dots in the bottom left sub figure of Fig. 3-2 form the corresponding channel profile of the cross section identified by the 'cross section line' in the upper left sub-figure. It is magnified in Fig. 3-3. For each measurement, the interferometer records (X,Y,Z) coordinates of 640×480 points in the '.xyz' file.
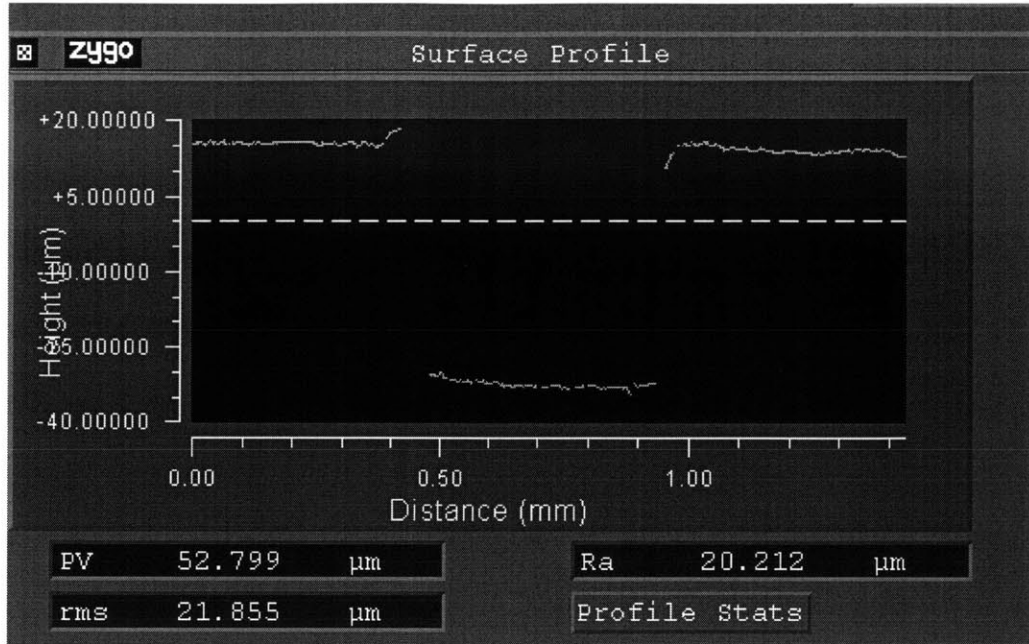
Figure 3-3   Profile of Cross Section

Since the interferometer itself does not provide analytical tools for these coordinates raw data, Matlab code was created to extract dimension data of the channel profiles from the '.xyz' file. First, a set of '.xyz' data is read into Matlab. Next, the code generates a mesh figure with this data and a 3D channel figure is thus obtained, shown in Fig. 3-4.
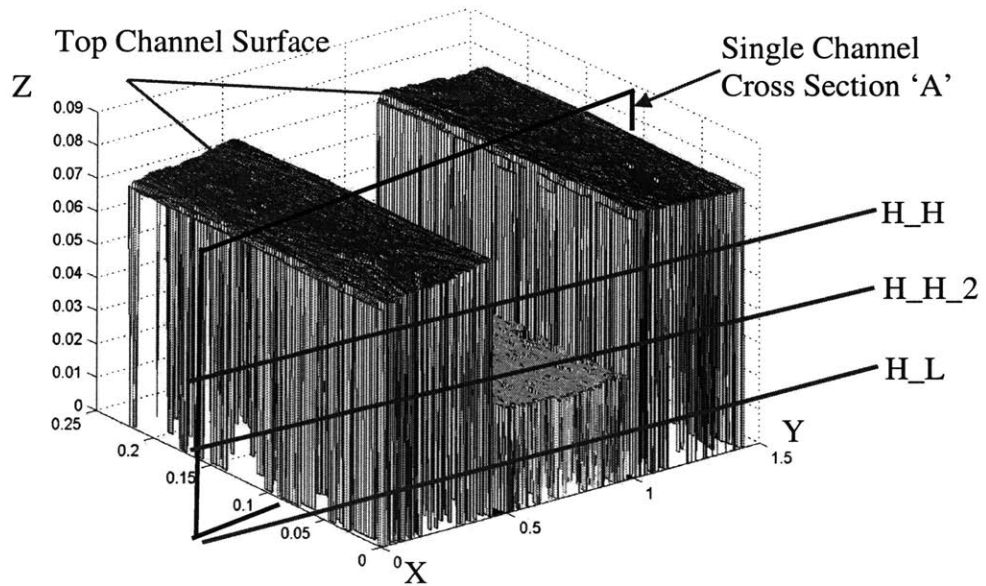
(a)   Channel Data Mapping
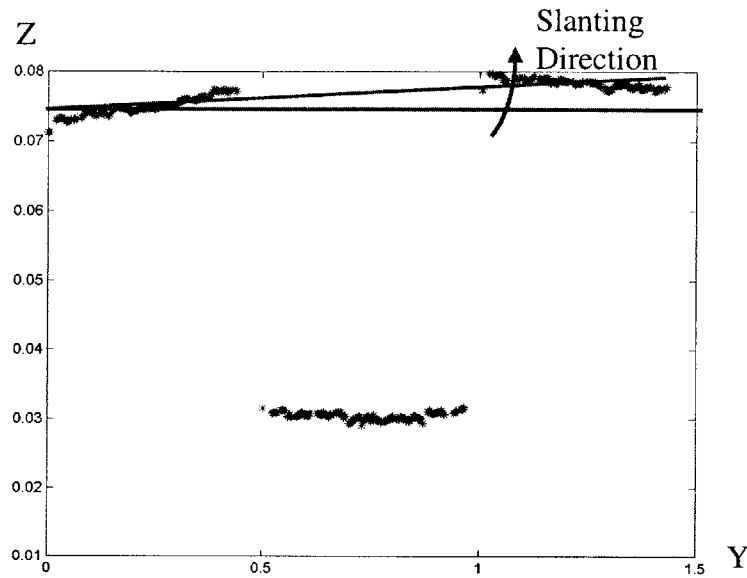
(b)   Channel Profile 'A'

Figure 3-4   Channel Data Regeneration in Matlab

In the CNC manufacturing process of a copper die, it is more accurate to control the bottom surface of the feature on the die than its top surface. Accordingly, during the measurement of a part, the top channel surface, shown in Fig. 3-4 (a), should be the focal surface in order to get fast and accurate measurement. Adjusting the orientation of the interferometer measuring table directly results in better coverage of birefringence on the focal surface, and it produces a well-leveled scan image.

However, even with careful operation of the interferometer, there is still some possibility to get a slanted channel profile. The slanting direction is shown with a red arrow in Fig. 3-3 (b). In this case, extra effort should be after the parts are measured under the interferometer.

In the direction of the length of a channel, slanting occurs because this alignment is done manually based on eyeball estimation. Adjustment in this direction is imperative too, so Matlab code is developed to help reorient the channel.

3.3.1 Reorienting the Channel
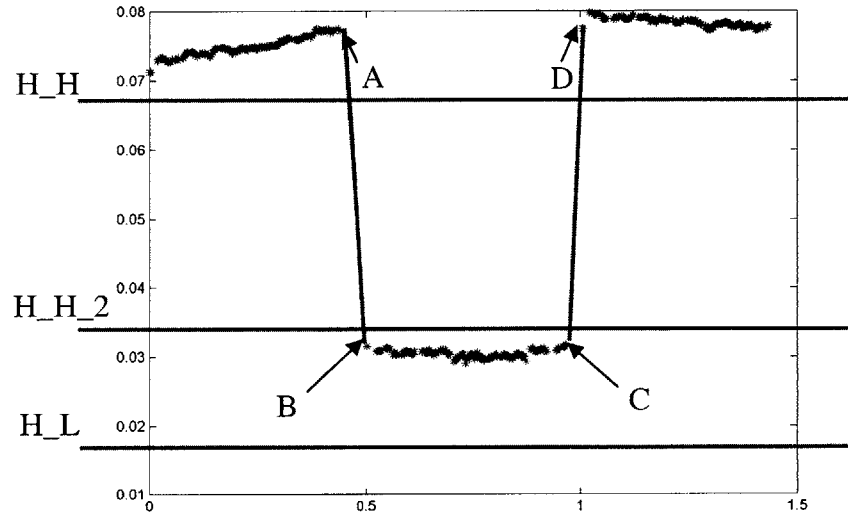
Figure 3-5   Channel Cross Section Critical Point Identification

Three red bars are set by the code operator each time based on the shape and

value of the whole scan of a channel when they are running matlab code to reorient a part.

The bars are shown in Fig. 3-4(a) and Fig. 3-5. These bars are used to divide the cross

section profile into three parts, shown in Fig. 3-5. The locations of the three red bars

remain the same for all 480 channel cross section profiles of the same scan. Any point

higher than the H_H bar is considered to be on the channel top, and any lower than the

H_H_2 bar and higher than H_L bar is considered to be on the channel bottom. Any point

between the H_H bar and H_H_2 bar is considered to be on the channel side, which does

not occur often, since most of these locations have null data. Point A and D are found to

be the extreme points that are closest to channel bottom on the channel top. Point B and C

are the extreme points that are closest to channel top on the channel bottom, shown in Fig.

3-5. For each channel cross section, there is a set of points of A, D, B, and C. As a result,

there will be 480 different sets of points of A, D, B and C for each channel scan.

When the channel is well formed, as in the situation shown in Fig. 3-5, the positions of the three red bars can vary across a large range. For example, the H_H bar can be placed any where between 0.032 and 0.07 mm in the Z coordinate; whereas the H_H_2 bar can be placed any where from 0.032 and 0.07 mm too. However, H_H bar should always stay in a position higher than the H_H_2 bar. In this situation, the four extreme points can be identified easily. When the channel is not well formed or the scanning of the channel is not sharp, as in the situation shown in Fig. 3-6, the position of the bars are normally placed according to where the locations of the majority of the profile points are. For example, the side wall dots should not be included in neither in the channel top dots group or in the channel bottom dots group. So the position of the H_H and H_H_2 bars are limited in small ranges. The ranges are between 0.108 to 0.109 mm and 0.067 to 0.068mm respectively.
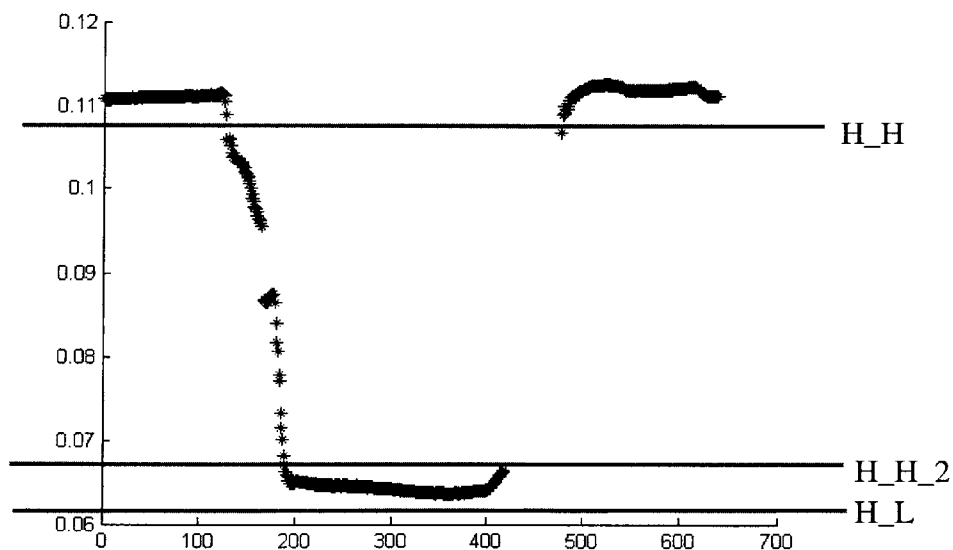
Figure 3-6   Not Well Formed Channel Profile

For each channel measurement, there are 480 cross sections such as the one shown in Fig. 3-5. All these channel cross sections combine into a 3D figure, shown in

Fig. 3-7. The channel bottom surface is always the first contacting surface between the die and PMMA. Points B and C are considered to be more precisely replicated than A or D. Therefore, points B and C are used to determine the orientation with respect to the coordinate frame.
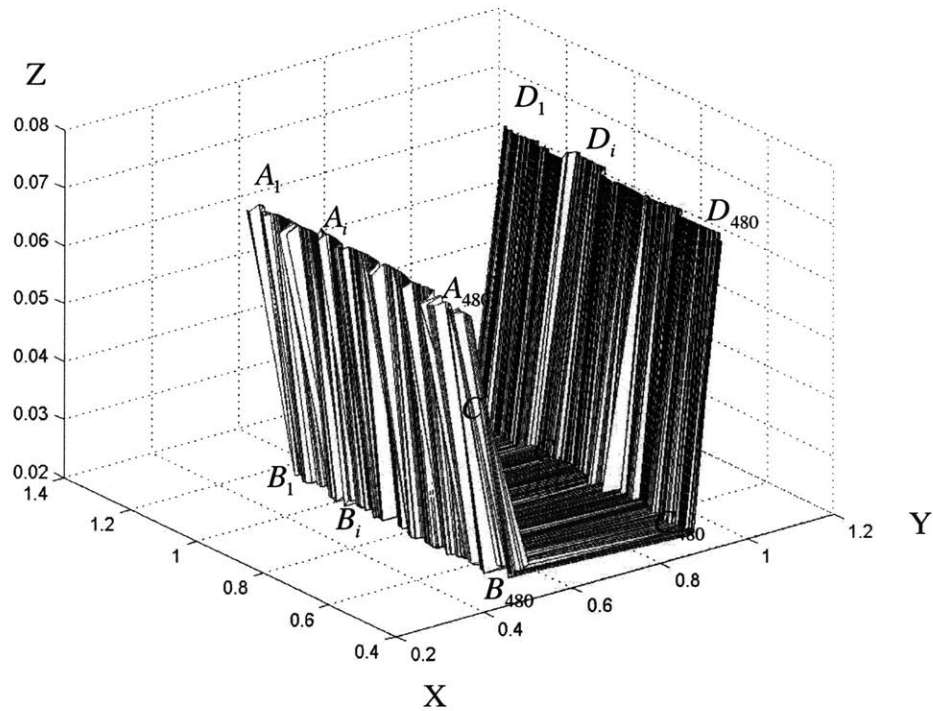
Figure 3-7   Combined 480 Cross Section Figure

Line L1xy and L2xy are the projection of the least square fit line for points $(B_1, B_2, \cdots, B_{480})$ and $(C_1, C_2, \cdots, C_{480})$ on XY plane, shown in Fig. 3-8. The angles between the lines and the X axis are α_1 and α_2. The average of α_1 and α_2 is α. It is defined as the angle between the channel and the X axis. A rotation of α angle about the Z axis for the channel will make the channel edges parallel to the XZ plane. This can be achieved through a cross product of channel coordinates matrix with a rotation matrix R_z. This matrix R_z is shown in equation (3-1).
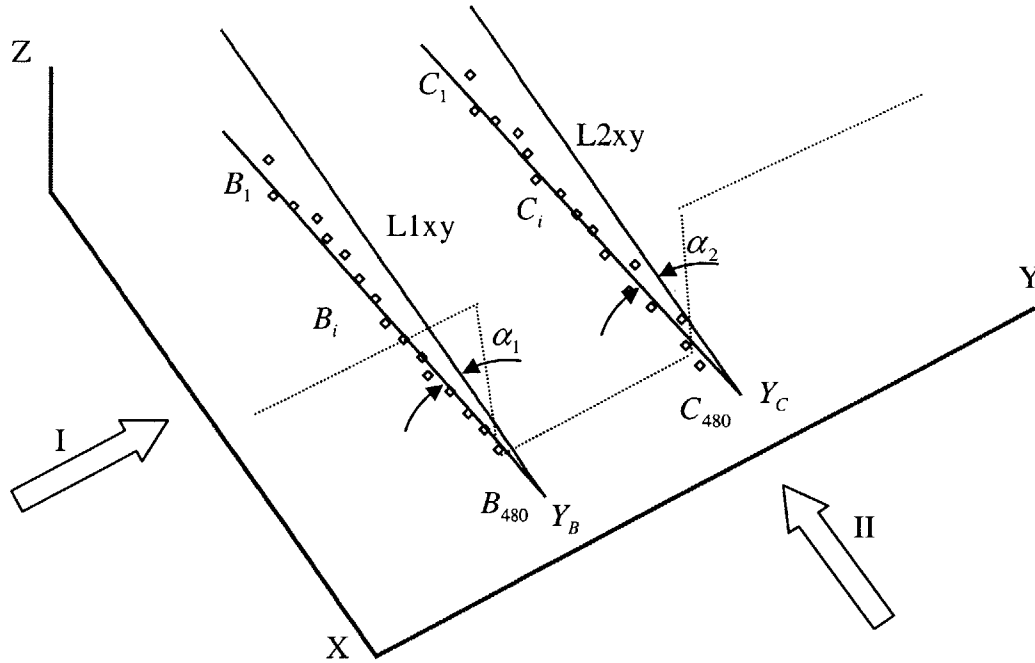
Figure 3-8   Channel Orientation With Respect to Z

$$R_z = \begin{bmatrix} \cos\alpha & \sin\alpha & 0 \\ -\sin\alpha & \cos\alpha & 0 \\ 0 & 0 & 1 \end{bmatrix}$$ (3-1)

The cross product is given by equation 3-2:

$$[X_n \quad Y_n \quad Z_n] = R_z \times [X \quad Y \quad Z]$$ (3-2)

Where X_n, Y_n, Z_n are the new coordinates of all measuring points of a channel scan after

the rotation, and X, Y, Z are the original coordinates of those points.

Lines L1xz and L2xz are the projections of the least square fit lines for points

$(B_1, B_2, \cdots, B_{480})$ and $(C_1, C_2, \cdots, C_{480})$. If seen along the arrow I in Fig. 3.8, lines L1xz

and L2xz are not parallel to the X axis, shown in Fig. 3-9. The angles between these lines

and X axis are β_1 and β_2. Their average β is the angle that the channel should rotate

about Y axis so as to obtain the reoriented channel. Similarly, a cross product of the

channel coordinates matrix $\begin{bmatrix} X_n & Y_n & Z_n \end{bmatrix}$ with a rotation matrix R_y can result in the

parallelism of the channel edges to X axis. The rotation matrix R_y is:

$$R_y = \begin{bmatrix} \cos\beta & 0 & -\sin\beta \\ 0 & 1 & 0 \\ \sin\beta & 0 & \cos\beta \end{bmatrix} \qquad (3\text{-}3)$$

The cross product operation is shown in equation (3-4)

$$\begin{bmatrix} X_{n1} & Y_{n1} & Z_{n1} \end{bmatrix} = R_y \times \begin{bmatrix} X_n & Y_n & Z_n \end{bmatrix} \qquad (3\text{-}4)$$

Where X_{n1}, Y_{n1}, Z_{n1} are the new coordinates of all measuring points after this rotation, and

X_n, Y_n, Z_n are the previous new set of coordinates of those points.
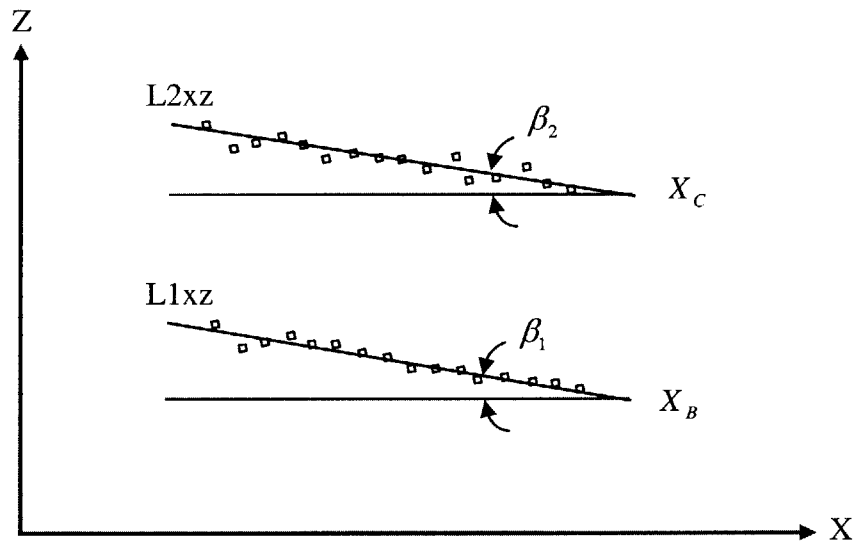
Figure 3-9   Channel Orientation With Respect to Y

Lines L'1xz and L'2xz are the results of the rotation of lines L1xz and L2xz about

Y axis. If seen into the YZ plane along arrow II direction of Fig. 3-8, one cross section of

the channel orientation with respect to X axis is seen as Fig. 3-10.
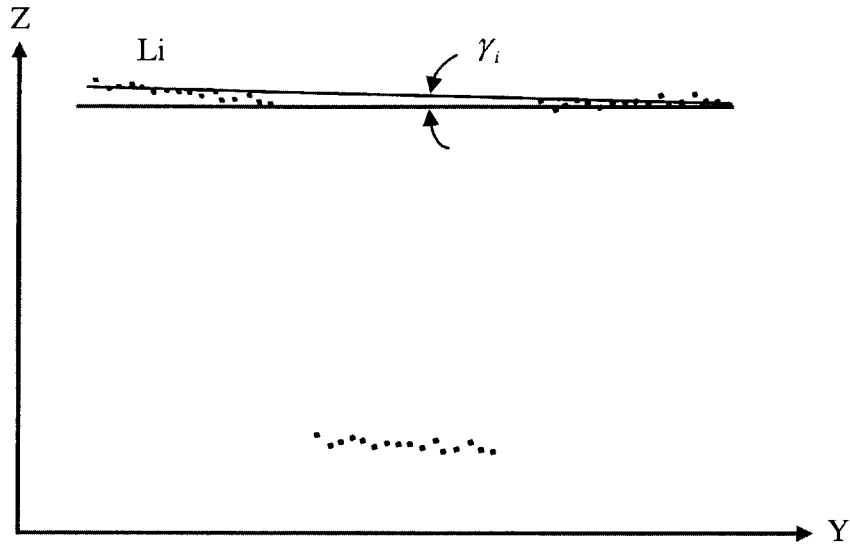
Figure 3-10   Channel Orientation With Respect to X

Li is the least square fit of the dots on channel top of γ_i is the angle between line

Li and Y axis. The average of the 480 γ_i is γ. A rotated channel coordinate matrix can be

obtained by a cross product operation too. This operation is shown in equation (3-5).the

angle the channel should rotate about X axis. Similarly, by taking the right product with a

rotation matrix R_x, the channel top is parallel to the XY plane:

$$[X_{n2} \quad Y_{n2} \quad Z_{n2}] = R_x \times [X_{n1} \quad Y_{n1} \quad Z_{n1}] \tag{3-5}$$

Where X_{n2}, Y_{n2}, Z_{n2} are the new coordinates of measuring points after this rotation, and

X_{n1}, Y_{n1}, Z_{n1} are the previous new set of coordinates of those points. The rotation matrix

R_x is:

$$R_x = \begin{bmatrix} 1 & 0 & 1 \\ 0 & \cos\gamma & \sin\gamma \\ 0 & -\sin\gamma & \cos\gamma \end{bmatrix} \tag{3-6}$$

After the three rotations, the channel edges are parallel to YZ and XY plane, and the channel top surfaces are parallel to XY plane. The final channel coordinate matrix $\begin{bmatrix} X_{n2} & Y_{n2} & Z_{n2} \end{bmatrix}$ is now valid for the later analysis.

3.3.2 Extracting Channel Dimension Information

The edges of the reoriented channels are perpendicular to YZ plane, which makes it valid to take the average of the 480 cross sections as the general representative channel cross section. For $Y_{n2}(i)$, $i = 1, 2, \cdots, 640$, the corresponding $\overline{Z}_{n2}$ is given in equation (3-7):

$$\overline{Z}_{n2} = \frac{Z_{n2}(X_{n2}(1), Y_{n2}(i)) + Z_{n2}(X_{n2}(2), Y_{n2}(i) + \cdots + Z_{n2}(X_{n2}(360), Y_{n2}(i))}{480} \tag{3-7}$$

The averaged channel cross section profile is shown in Fig. 3-11.
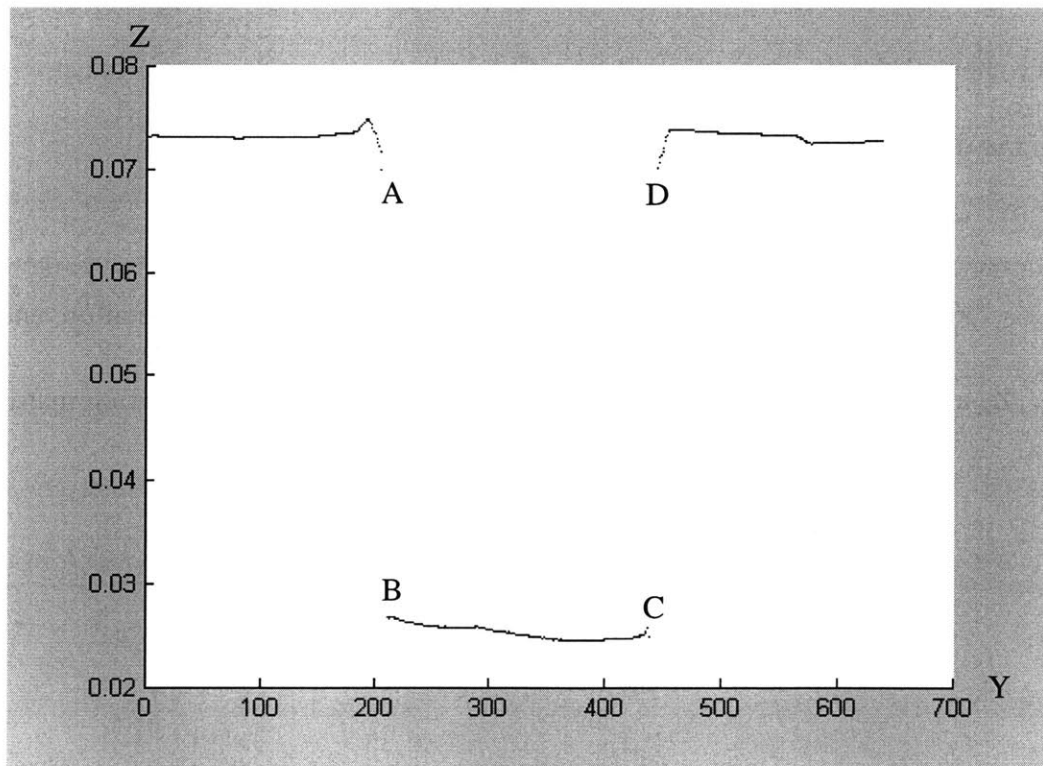
Figure 3-11   Average Channel Profile

Three major dimensions of this channel are defined as:

$$Depth = Z\_H_T - Z\_L_B \tag{3-8}$$

$$ChannelWidth = \frac{(Y_A + Y_D) - (Y_B + Y_C)}{2} \tag{3-9}$$

$$ChannelWallAngle = a\tan\left(\frac{(Y_B - Y_A) + (Y_D - Y_C)}{2} / \frac{(Z_A + Z_D) - (Z_B + Z_C)}{2}\right)$$

$$\tag{3-10}$$

where Z_H_T is the average Z coordinate of the channel top dots, and Z_L_B is the average Z coordinate of the channel bottom points. Coordinates Y_A, Y_B, Y_C, Y_D and Z_A, Z_B, Z_C, Z_D are the Y and Z coordinates of points A, B, C, and D points respectively. All the three channel geometry dimensions are used to evaluate the replication of the channels.

3.3.3 Channel Average Shape

Besides the quantitative data, the Matlab code also provides the final average channel shape. The average values of the Z and Y coordinates of channel bottom for the case of F=200N are set to be the target Z and Y positions of the other cases. The discrepancy of the target Z and Y positions and the average values of the Z and Y coordinates of channel bottom of another case with a different embossing force are $(\Delta Z, \Delta Y)$. This vector defines the distance and direction for other cross section profiles to move toward the target position. The movement of the profiles will result in a superimposed figure, shown in Fig. 3-12. By observing the curves, we can obtain a general sense of the material flow pattern for the particular die design. The detailed explanation of this figure will be given in Chapter 4.
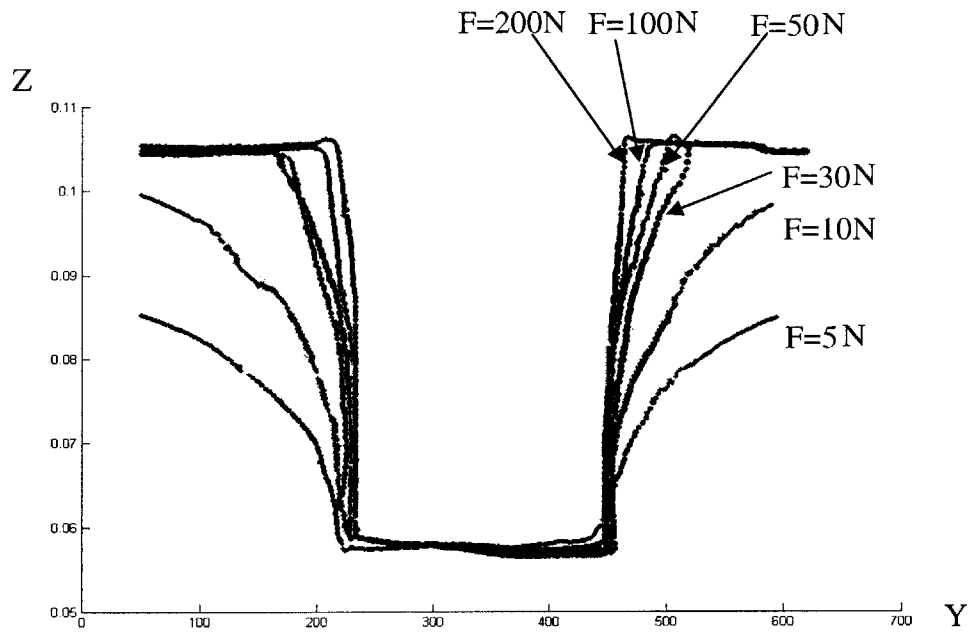
Figure 3-12   Channel Cross Section Profiles under Different Embossing Force

4

Process Window Identification

4.1 Introduction

As mentioned at the outset, the focus of micro embossing process research has been on the exploration of its applications and feasibility. Successful applications of micro embossing process under variable embossing parameters are demonstrated and reported. As reviewed in the first chapter, embossing parameters in papers [26][36][41][45] and etc cover a range of embossing temperature from room temperature up to 290 °C, and embossing pressure from 1 MPa to 125 MPa. Some other parameters, such as de-embossing temperature, embossing velocity, also vary a lot.

Within the range of embossing parameters, there could be a suitable processing window that yields good product parts, and maximizes product throughput and minimizes production costs at the same time. In this chapter, the procedure of identifying such a process window is presented.

4.2　Candidate Critical Process Parameters

Given the current embossing machine setup, PMMA properties and die design, the product quality is limited by the properties and states of the machine and material. In this section, these constrained limits are discussed.

4.2.1　Material Limits

PMMA is a synthesized polymer chain with a repeating molecule. The individual molecule is [C6H10On] n, shown in Fig. 4-1.
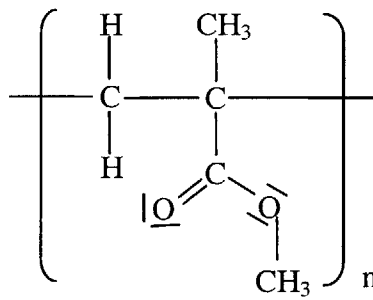
Figure 4-1　　PMMA Molecule

When the PMMA is heated to a temperature of around 100°C, this chain starts to become loose and enables the reorientation of the chain under pressure. This reorientation is not permanent, which means there is spring back when it is cooled down. When the temperature increases to around 150°C, the bond between the chains starts to break. This makes it possible for the PMMA to deform permanently under a small pressure. Moreover, it can be cooled down without residual stress because the molecules reorient themselves according to the die shape.

A set of compression tests was done by Ames [49] to identify the PMMA properties. In the tests, a cylindrical PMMA specimen that is a quarter inch in diameter

and half inch in length. The specimen is compressed with constant compression strain rate in constant temperature condition. With variant strain rate and embossing temperature, a set of experimental stress strain data is obtained and presented in Fig. 4-2.
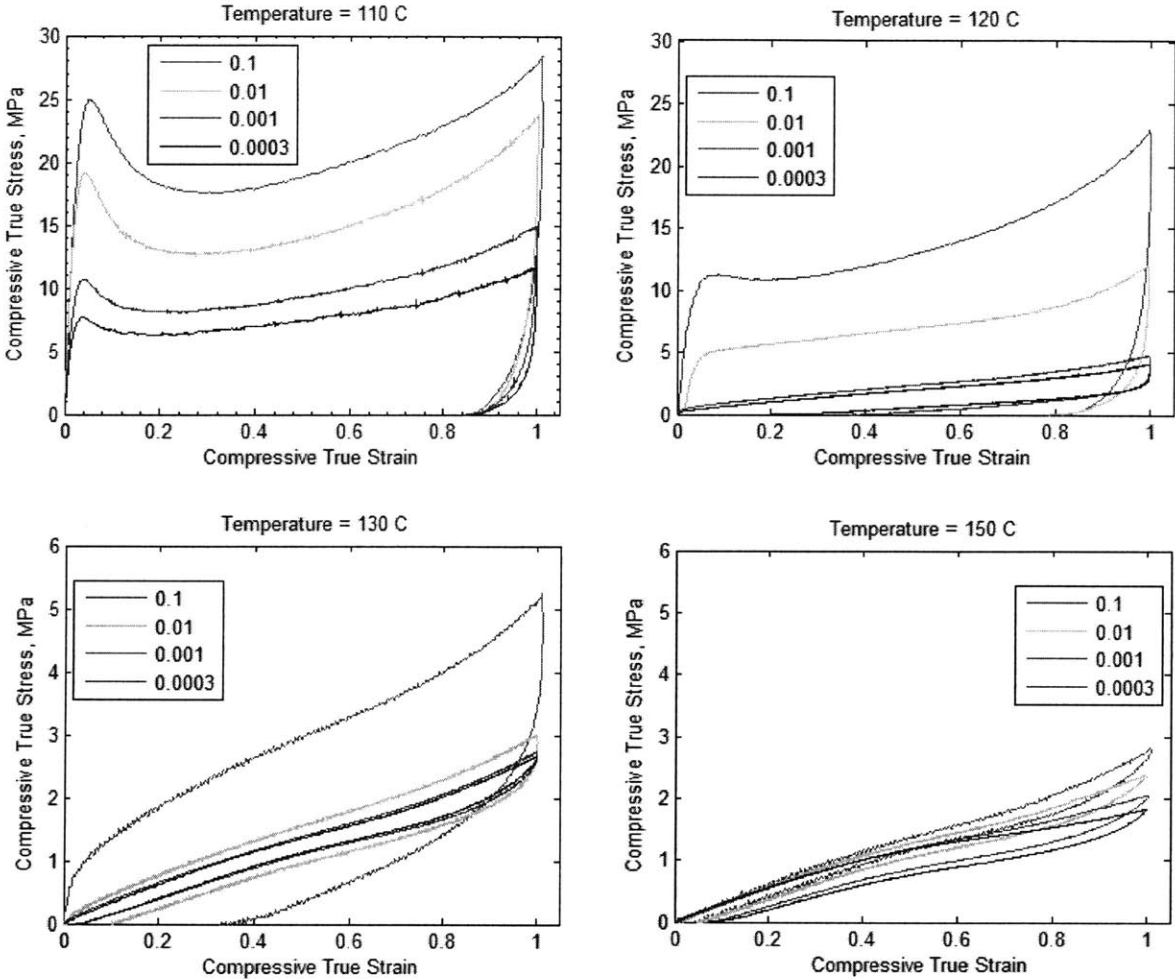
Figure 4-2   Stress Strain Curve of PMMA at Different Temperature (from [49])

The figure above shows that in the situation when the temperature is 110 °C, the stress ramps up quickly to a peak value under a small strain, and drops down fast and then ramps up slowly as strain increases. At the end of the unloading curve, there exists large residual strain. This trend is repeated with the varying strain rate from 0.1 to 0.0003. However, when the temperature is 120 °C, that trend repeats only when the strain

rate is between 0.1 and 0.01. Besides this, there is no peak stress in low strain region, and there is very small residual strain at the end of unloading curve when the strain rate drops to 0.001 or lower. When the temperature reaches 150°C, the stress strain curves remain the same as strain rate is varying from 0.1 to 0.0003. At the end of the unloading curve, there is almost no residual strain.

The information conveyed in Fig. 4-2 shows that embossing temperature, embossing strain rate will impact PMMA properties in a certain way. For our first generation machine set up, it takes around 10 and 18 minutes to heat the die and PMMA up to 110°C and 150°C respectively from room temperature. It takes around 30 to 60 seconds to cool the die and PMMA from these embossing temperatures down to a certain de-embossing temperature. In order to minimize the embossing thermal cycling time, which occupies 90% of embossing cycling time, lower embossing temperature is always preferred.

In this embossing temperature range, embossing strain rate has an impact on PMMA mechanical properties [49]. Also, the mobility of the material is not high in this temperature range. Therefore, in order to allow enough time for the material to flow, slow embossing velocities were chosen. Since the Instron machine was in force control mode, the embossing velocities had the unit of N/min. The velocities were 100, 400, 1000N/min.

An experiment was carried out to find out the approximate corresponding extension strain rate of a force velocity. A pure PMMA piece was pressed by the movable anvil at different force velocities until the force reached 800N. The total pressing time for situations with velocities of 100, 400, 1000 N/min was around 8, 2, and 0.8 minutes respectively. The bulk extension of the movable anvil under 800N was around 0.1-0.2mm.

The engineering strain was around 0.1-0.2. However, because the Instron machine has a very compliant frame, the real engineering strain of the PMMA was between 0.01 to 0.03. This lead to strain rate of 0.00004/s, 0.00016/s and 0.0004/s. They were mostly far below the smallest extension strain rate in Ames' data [49].

The effect of residual stress of the function of embossed devices depends on the specific applications. Generally speaking, for micro fluidic devices that operate at room temperature, residual stress won't be a problem for the devices. In this thesis, the residual stress in the embossed devices is not a focus consideration. Therefore, low embossing temperatures that might cause residual stresses, such as temperatures between 110°C and 135°C, are included in our experiments, since lower temperatures have other advantages such as faster cycle time and less process energy.

Higher embossing forces are required to get well formed embossed parts at lower embossing temperatures according to the experiment results in [49]. Since the Instron machine has fast and fine resolution of force control, higher force levels do not cost much in terms of time and expense. Thus, a higher embossing force within the machine range is preferred over higher temperatures, if parts of good quality can be made. .

4.2.2 Force Limits

As stated above, the magnitude of the force is neither significant time nor equipment expense. However, once the die design scales up to 4 inches and the features become denser than the die design in this thesis, much higher force is required. In that case, identifying the minimum embossing force is crucial to reduce the machine set up cost, because there will be no need to buy bigger load cell and anvils, for example.

Accordingly, the constraint of the minimum embossing force can guide a more reasonable die design given the current machine set up.

In order to find out the possible minimum embossing force, a preliminary embossing experiment with the copper die was done at 110°C, and the maximum embossing force was set to 800N. The force-extension curve is shown in Fig. 4-3.

Fig. 4-3 shows that there is a slope change when the force is around 50 N. This indicates that when embossing force reaches 50N, the filling of the material into the cavities of the die is nearly finished and the recessed surface of the die and the channel top surface of the embossed part are starting to contact. Whether a 50N embossing force is enough to get fully replicated part is studied in this thesis.
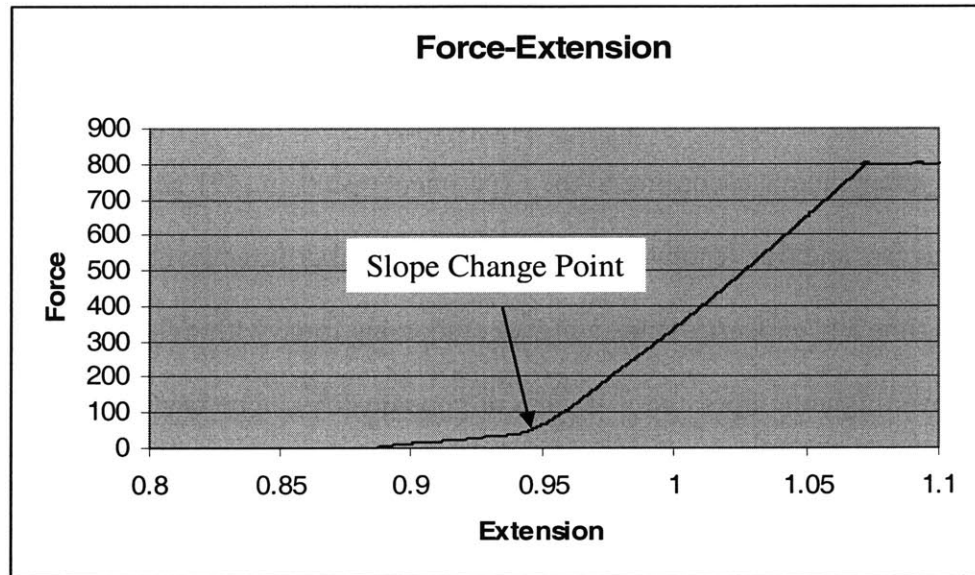
Figure 4-3   Force vs Extension Curve of Embossing at 110 °C

4.2.3 Experiment Parameters

In the following sections of this chapter, experiments that aim to investigate which embossing temperature, embossing force and embossing velocity window will yield a good part will be documented.

The three different embossing temperatures are 95, 110 and 135°C, the force

levels are 10, 50, 100, 200, 800N, and the embossing velocities are 100, 400, 1000N/min.

4.3 Experiments and Results

4.3.1 Experiment Cycle

As stated in Chapter 2, extension control is applied during the embossing starting

stage, and force control is applied during the embossing and cooling stage. The test path

profile is shown in Fig. 4-4.
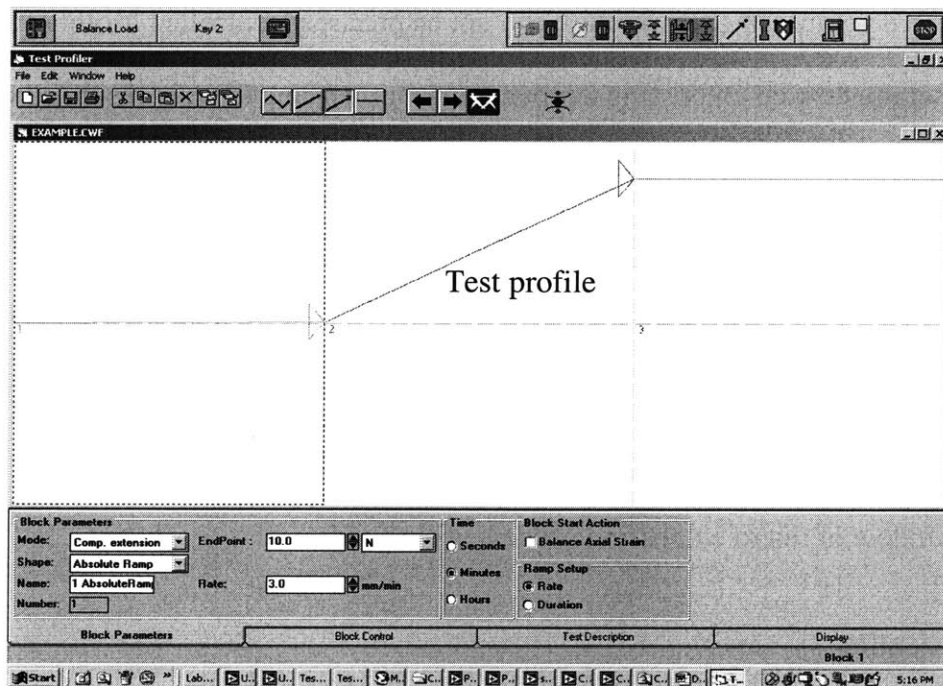
Figure 4-4   Embossing Displacement and Force Control Path

The upper anvil first moves toward the fixed lower anvil at a speed of 5mm/min

under extension control until the contacting force between the die and the PMMA piece is

2N. This initiates the shift from extension control to force control for the Instron machine.

Under force control, the contacting force will increase at a certain constant force rate

until it reaches the preset ultimate embossing force. While maintaining this embossing force, the material eventually stops deforming, this results in the dropping of the extension velocity of the moving anvil. When the extension velocity drops to $1\mu m/5second$, the deformation is considered to be complete and the cooling cycle starts. During the cooling cycle, the embossing force is still maintained at the ultimate level. As soon as the die and PMMA are cooled down to a specified de-embossing temperature, the testing profile run by Merlin software is terminated. With the releasing of the movable anvil and the separation of the PMMA and the die, the whole embossing cycle is finished. Because the de-embossing temperature can not be precisely controlled for this embossing machine set up, how de-embossing temperature is influencing the part result is not a research focus in this chapter. A de-embossing temperature around $55\,^{\circ}C$ is used.

Interferometer measurements of embossed parts are then carried out and the part quality protocol from Chapter 3 is run to extract channel dimension information from the measurement data. Based on this data, the geometry dimension quality of the embossed parts under variant embossing conditions is compared and assessed. Consequently, the process window of micro embossing process is obtained.

4.3.2 Results

Impact of Embossing Velocity and Temperature on Channel Quality

In order to discover the impact of embossing velocity and temperature on channel quality when a relatively big embossing force is applied, a set of experiments with variant embossing temperature and velocity was carried out. A constant embossing force was set to 800N. The resulting relationship between channel depth and embossing velocity and temperature is shown in Fig. 4-5. This figure shows that when embossing force is 800N,

the increase of embossing temperature from 95°C to 110°C results in the increase of 20

to 30 microns for channel depth, whereas the channel depth difference between 110°C

and 135°C is small (on the order of one micron).

Moreover, embossing velocity has an obvious impact on channel depth at an

embossing temperature lower than the glass transition temperature, such as 95°C. The

slower the velocity the deeper the channel tends to be. When the embossing temperature

is above the glass transition temperature, such as 110°C and 135°C, embossing velocity

does not have any obvious impact on channel depth.
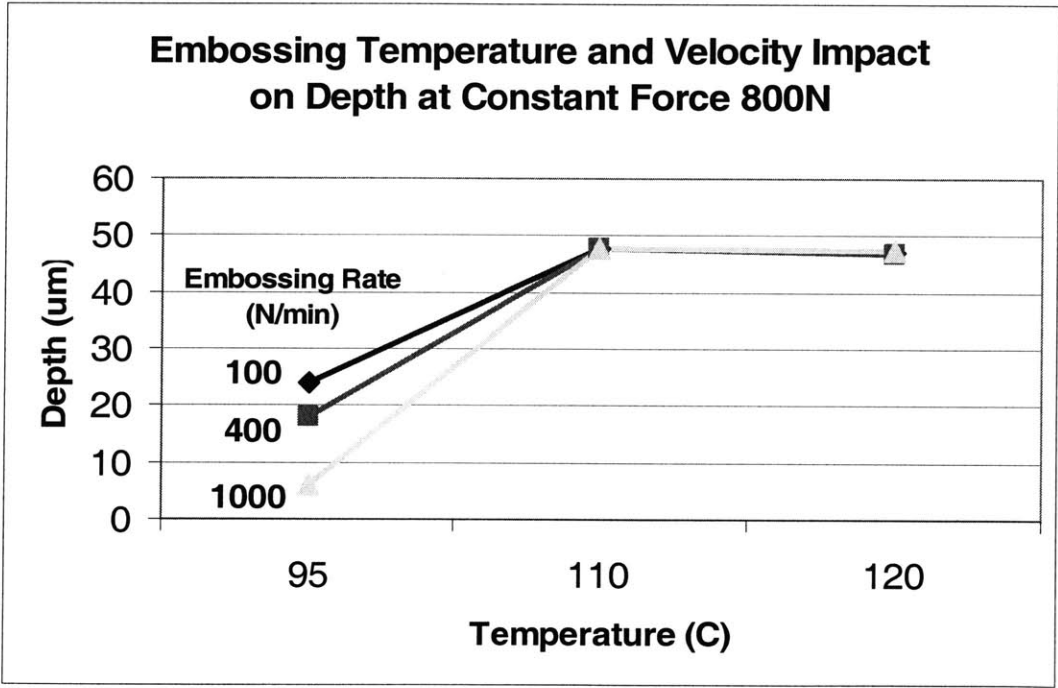
Figure 4-5   Channel Depth vs Embossing Velocity & Temperature

Embossing Temperature and Velocity Impact on Channel Wall Angle at Constant Force 800N
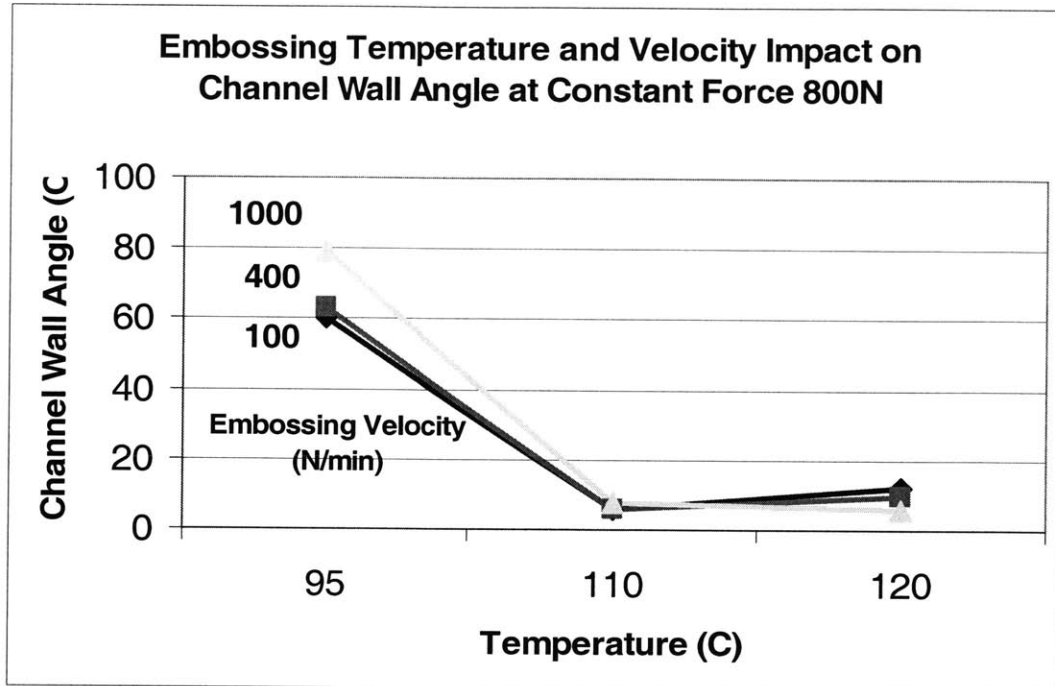
Figure 4-6 Channel Wall Angle vs Embossing Velocity & Temperature

Similarly, channel wall angles drop dramatically from above 60 degrees to around 10 degrees when the embossing temperature increases from 95°C to 110°C. Also, not much difference in wall angle (4 degrees) is observed between 110°C and 135°C embossing conditions.

When the embossing temperature is 95°C, the channel wall angle strongly depends on embossing velocity. Higher embossing velocity leads to larger channel wall angles, which is an indication of a poorly formed channel. When embossing temperature is above 110°C, channel wall angles don't really depend on the embossing velocity.
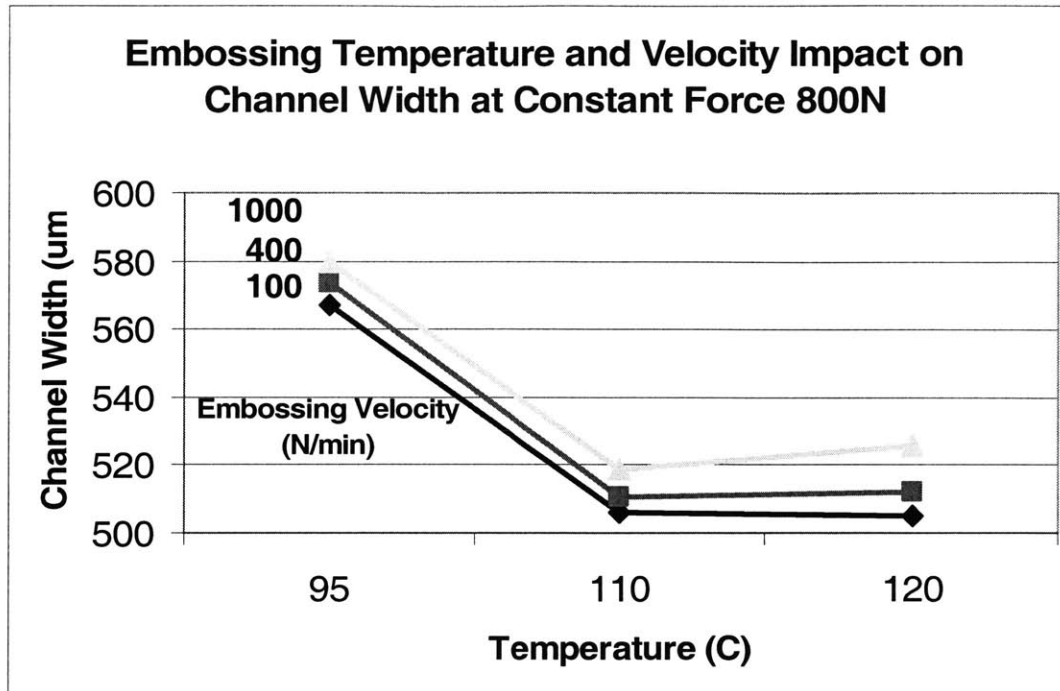
Figure 4-7 Channel Width vs Embossing Velocity & Temperature

The relation between channel width and embossing velocity and temperature is shown in Fig. 4-7. Again, when embossing temperature is lower than the glass transition temperature, there is obvious material under filling into the die, which results in big channel width. When embossing temperature reaches 110°C or 135°C, channel width discrepancy between them becomes small, around 10 microns when embossing velocity is 1000N/min and within 3 microns when embossing velocity is 400 and 100 N/min. . Since the lateral measuring resolution for a single point is around 5 microns, the 10 microns channel width difference is in the same order of the measuring resolution. Thus, it is not very convincing to conclude that there is significant channel width discrepancy between the 110°C and 120°C embossing conditions with different embossing temperatures.

On the other hand, embossing velocities of 100, 400 and 1000N/min are observed to have impact on channel width at any embossing temperature. Fig. 4-7

indicates that higher embossing velocity leads to higher channel width, which means poor channel formation. However, this conclusion is not very strong either, because the discrepancy of channel width introduced by different embossing velocityies at the same embossing temperature is also within 10 microns.

In conclusion to this section, an embossing temperature higher than the PMMA glass transition temperature is required to obtain well replicated parts. Embossing velocity does not impact the part quality in terms of channel depth and channel wall angle when embossing temperature is between 110°C and 135°C.

Because of low lateral measuring resolution, channel width is not sensitive to these process parameters. Thus, channel width is not used to evaluate the impact of process parameters on channel quality in the later chapters of this thesis. Instead we will use channel depth and channel wall angle.

Impact of Embossing Force and Velocity on Channel Quality at Embossing Temperature 110 °C and 125°C

The last set of experiments show that when embossing temperature is 95°C, the PMMA parts do not form well under the highest embossing force available with our current load cell. Consequently, in the rest of this thesis, the embossing condition with embossing temperature of 95°C will not be studied. Subsequently, a set of experiments was carried out at embossing temperatures of 110°C and 125°C in order to discover the impact of embossing force and velocity on channel quality.
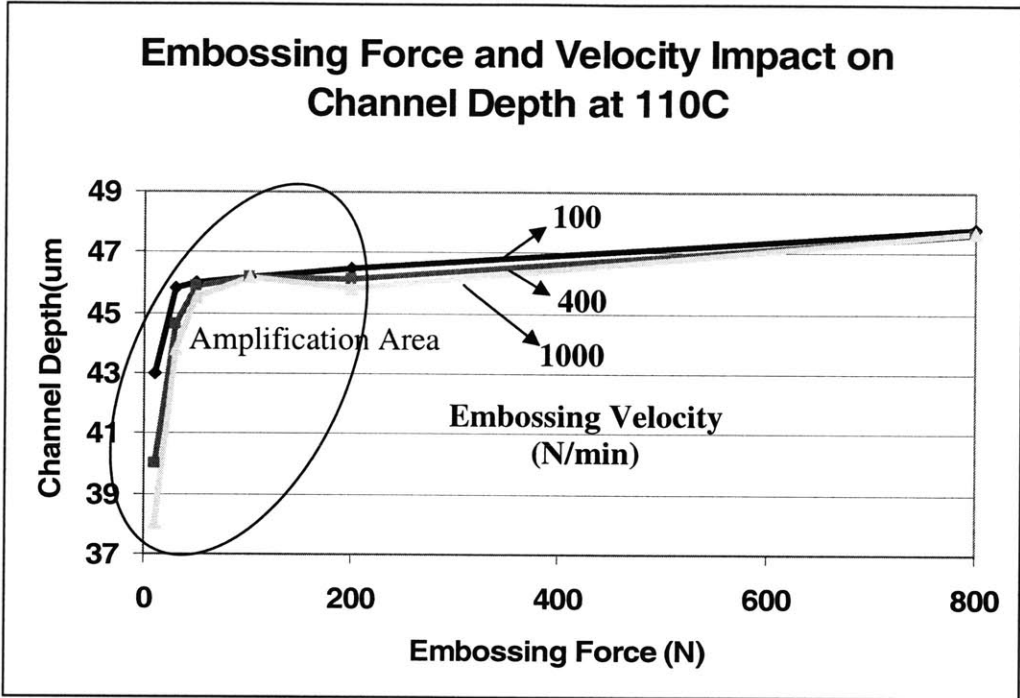
(a)   Force Ranges from 10N to 800N
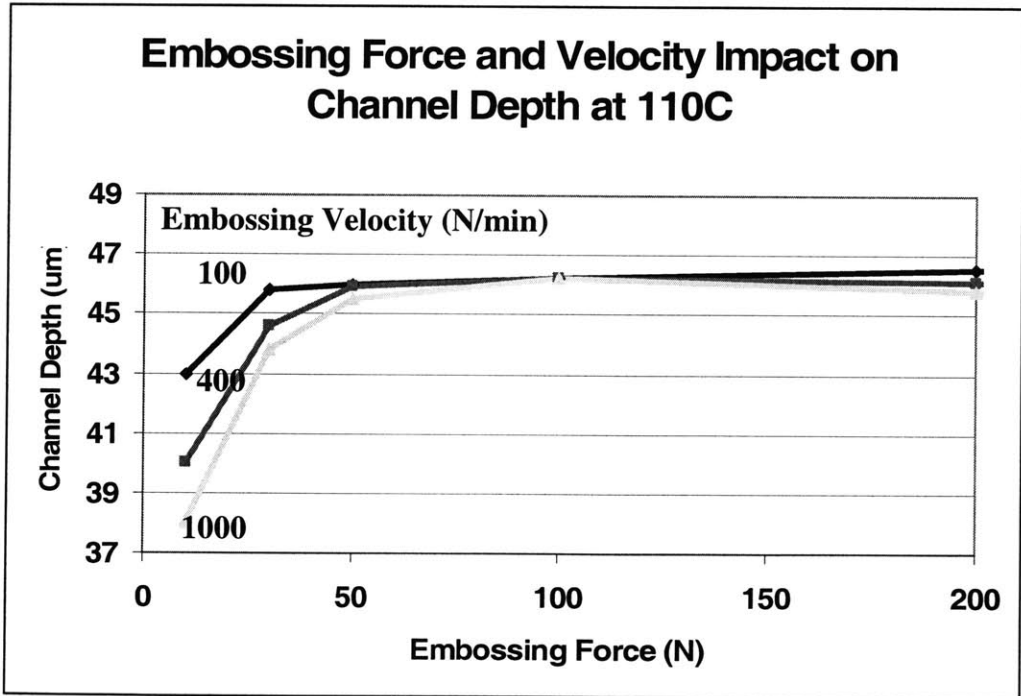
(b)   Amplification Area

Figure 4-9 Channel Depth vs Embossing Force & Velocity at Embossing Temperature of 110 °C

Fig. 4-9 shows the relation of channel depth and embossing force and velocity.

Fig. 4-9 (b) is an amplification figure of the circled part of (a). Take the situation when

embossing velocity is 100N/min for example. It is clear that channel depth starts to

increase with a lower slope when embossing force reaches 30 N. This will be defined as

the "kneeing force" of embossing process. When embossing velocities are 400 and

1000N/min, those kneeing forces are around 50N and 100N respectively.

Fig. 4-10 (a) is a superimposed channel cross section profile of PMMA parts

embossed under different embossing forces at embossing temperatures of 110°C and

embossing velocity of 100 N/min. Fig. 4-10 (b) is a schematic that shows the relative

position of channel profiles to the copper die profile. Fig. 4-10 shows that when

embossing force reaches 30 N, channel top surface is already in contact with die bottom

surface. When embossing forces increase, the channel side walls are moving toward the

tool side walls to finish the deformation of material to copper die.
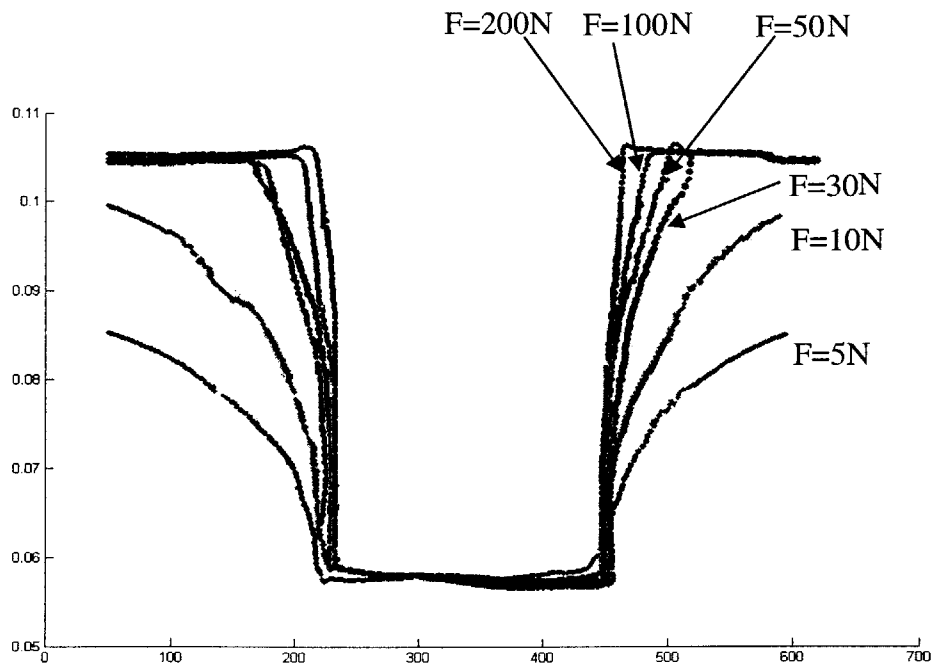
(a)   Superimposed Cross Section Profile of Channels
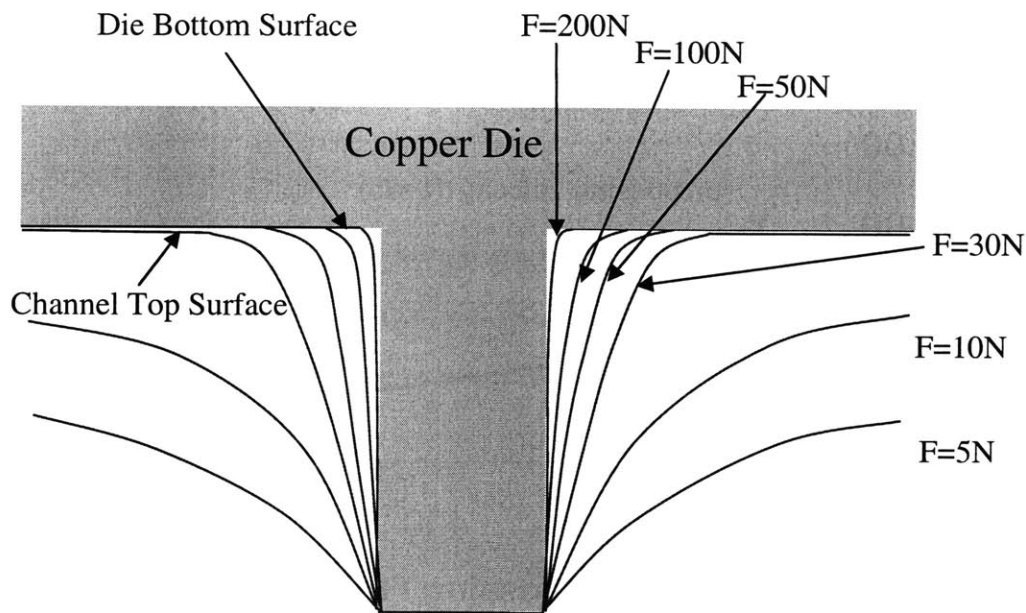
(b)   Schematic of Cross Section Profile of Channel and Copper Die

Figure 4-10   Channel Profiles at Embossing Temperature of 110°C and Velocity of 100N/min

Fig. 4-11 is the channel wall angle chart of PMMA parts embossed under different embossing forces at embossing temperature of 110°C and embossing velocity of 100N/min.

Both Fig. 4-9 and Fig. 4-11 indicate that when embossing temperature is 110 °C, embossing velocity has and impact on channel geometry dimensional quality when embossing force is below kneeing force, and it has little impact on channel quality when embossing force is big enough, around 800N in this case. Thus, whether the embossing force is large enough becomes crucial for part quality. Since embossing force can be exerted with a very fast embossing velocity, 1000N/min, it becomes a low cost process parameter in terms of process cycle time and energy expense. In this thesis, 800N is herein set to be the embossing force.

Embossing Force and Velocity Impact on Channel Wall Angle at 110C
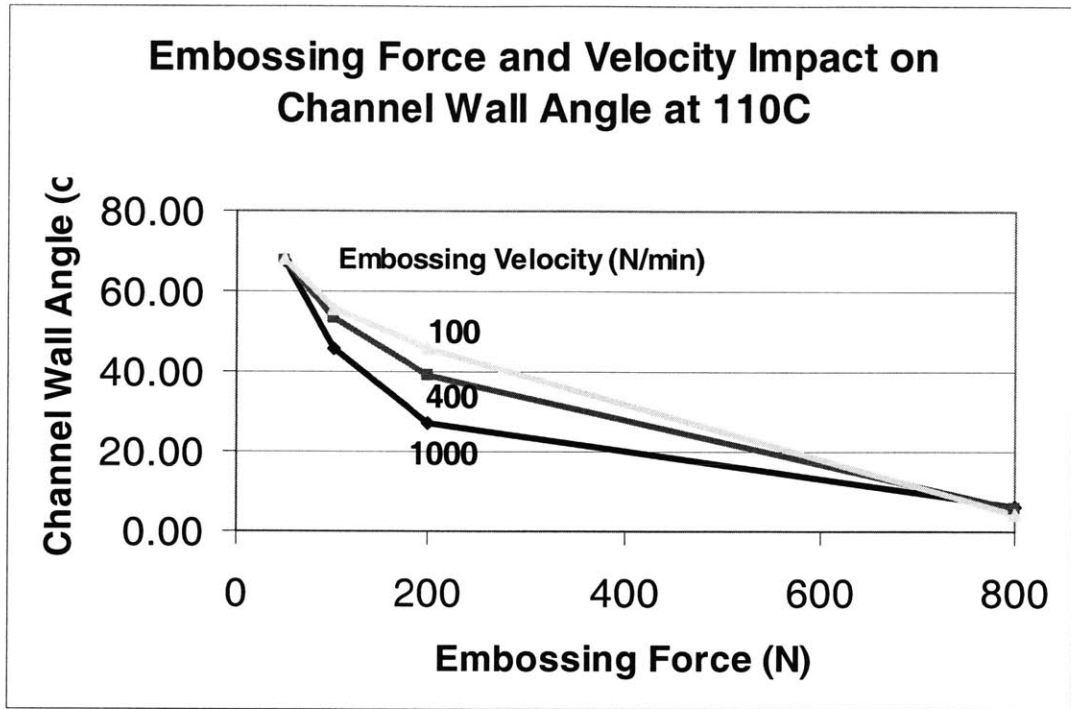
Figure 4-11   Embossing Force and Velocity Impact on Channel Wall Angle at 110°C

Similar experiments are done when embossing temperature is 125 °C. In order to reduce experimental replications, the experiments with embossing velocity of 1000N/min are eliminated. This is because from the experience above, channel quality is not sensitive to embossing velocity. This sensitivity becomes even smaller with increase of embossing temperature according to reference [49]. The impact of embossing force and velocity on channel quality figures are shown in Fig. 4-12. It shows that similar observation is obtained when embossing temperature is at 125°C.
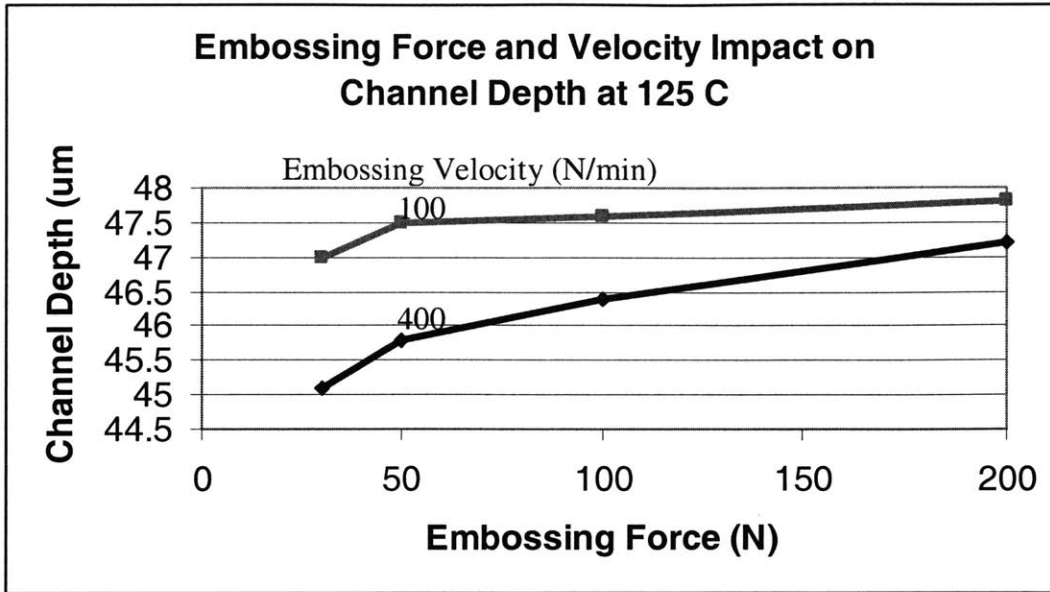
(a)   Embossing Force and Velocity Impact on Channel Depth at 125 °C
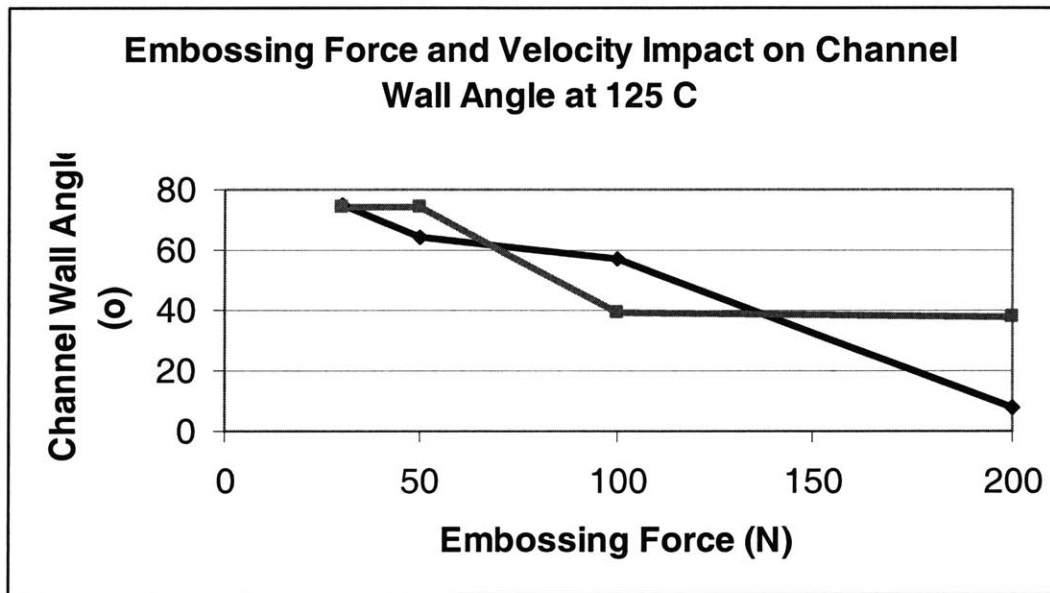
(b)   Embossing Force and Velocity Impact on Channel Wall Angle at 125 °C

Figure 4-12   Embossing Force and Velocity Impact on Part Quality at 125°C

A set of experiments were carried out to study the impact of embossing force and temperature on channel quality with natural cooling.
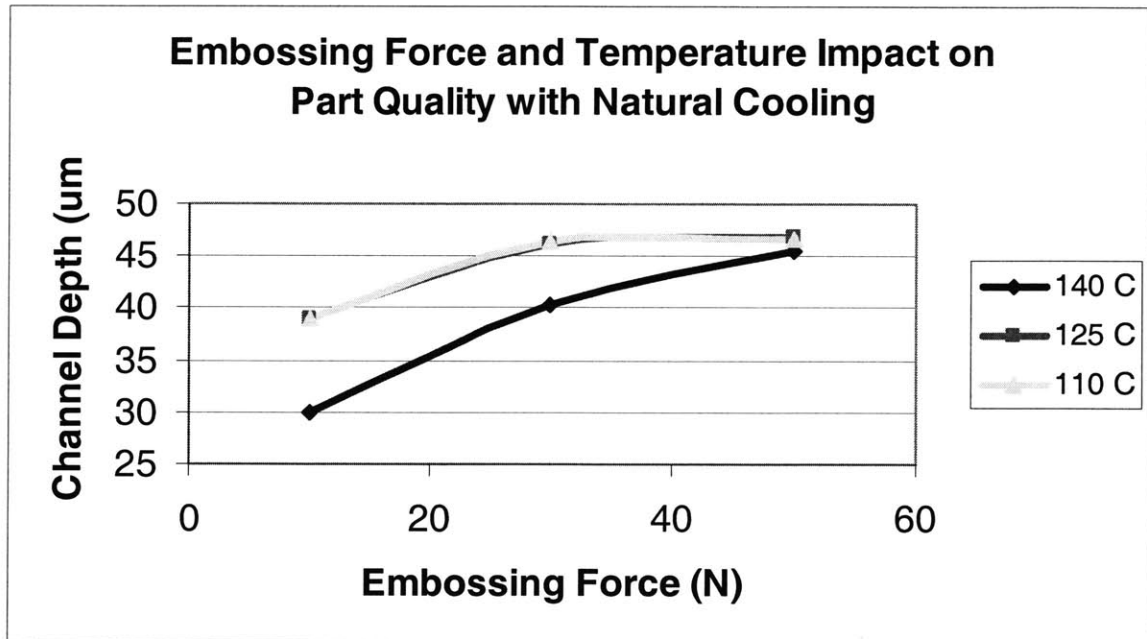
Figure 4-13 Embossing Force and Temperature with Natural Cooling

The first generation machine in our lab cannot control the cooling rate or the de-embossing temperature. However, it is possible to get two extreme cooling rates: full fluidic flow cooling and natural cooling, which is a cooling method without any other cooling assistant than ambient air.

Fig. 4-13 shows that in natural cooling situations, lower embossing temperatures lead to higher channel depth and better channel filling. Compared with the rapid cooling conditions (noted as 'RC') result in Fig4-14, natural cooling (noted as 'NC') blurs the discrepancy of embossing temperature, and it helps the PMMA to deform better. This result shows that the cooling rate does have an impact on the part quality. However

natural cooling from 110 °C to 55°C takes around half an hour, which makes it less

applicable in real productions.

Embossing Force and Cooling Method Impact on Channel Depth
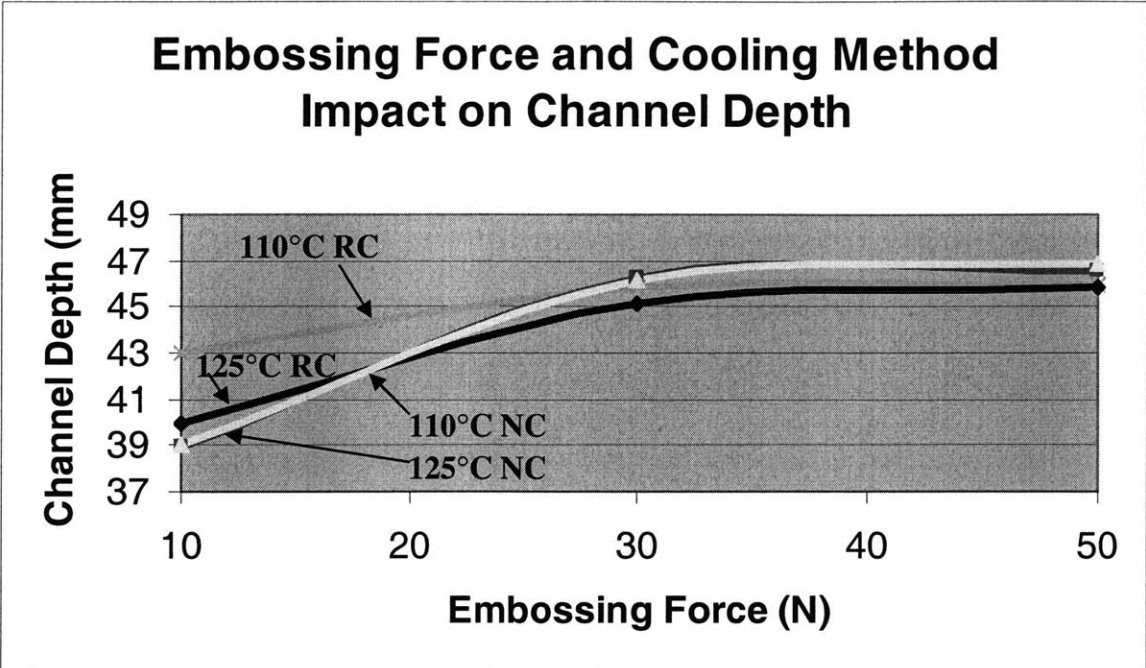
Figure 4-14 Embossing Force and Cooling Method Impact on Channel Depth
at Different Embossing Temperatures

4.3.3 Conclusions

Embossing velocity has no impact on part quality as long as the embossing force

is sufficiently high. For the test part formed in the experiments herein, the embossing

force is chosen to be 800N, which proved to yield good material deformation when the

embossing temperature is above the glass transition temperature. A force of 800N is also

a reasonably reliable control force with a 1KN load cell. Cooling rate also has an impact

on parts quality. Because the current machine set up is not capable to control cooling rate,

it will not studied further in this thesis.

De-embossing temperature is not studied in this chapter because it is also an

approximate process parameter with our machine set up. However, it might be an

important variable that impact parts quality. It will be further discussed in the next chapter. Another important embossing parameter, embossing temperature will also be further discussed in Chapter 5.

5

Process Variation Characterization

5.1 Introduction

The identification of a process window in Chapter 4 indicates that for our part, embossing force and embossing velocity should be 800N and 1000N/min respectively in order to obtain well formed parts and have a minimum process cycle time . More research that relates to processing window identification of embossing temperature and de-embossing temperature will be presented in this chapter.

Process variation, is another important process characteristic to assure consistent quality and productivity. In this chapter, micro embossing process variation is studied.

5.2 Experiment Parameters

The conclusion of Chapter 4 shows that once embossing temperature is above the glass transition temperature, and the embossing force is large enough to deform PMMA with a reasonably fast embossing velocity, the actual magnitude of the embossing temperature does not affect the part quality enormously. Fig. 5-1 shows the stress-strain curve of PMMA under different temperature with the strain rate of 0.003. This figure indicates that embossing temperatures above 120°C tend to fall in one group, which differs from temperatures around 110°C. Therefore, in order to reduce thermal cycle time and reduce the experiment numbers, two embossing temperatures, 110°C and 120°C, are chosen.
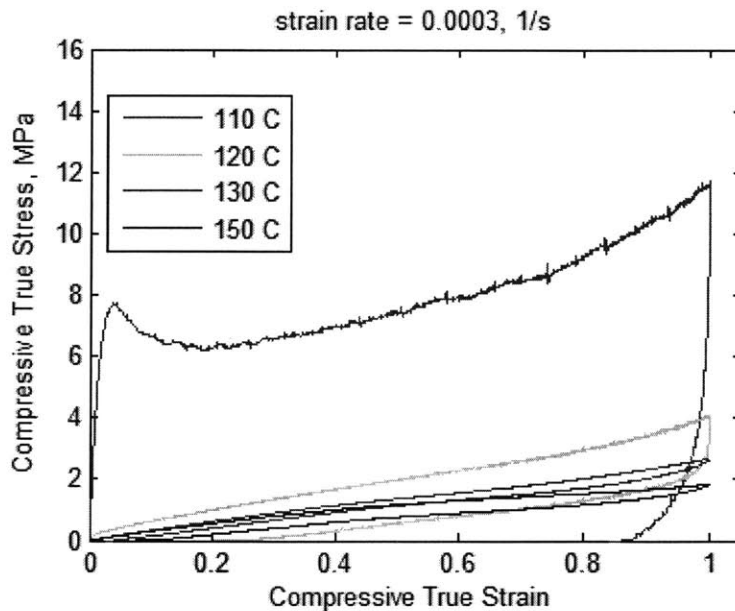
Figure 5-1   Stress Strain Curve of PMMA at Strain Rate of 0.0003 (from [47])

De-embossing temperature also relates to total thermal cycle time. Thus, higher de-embossing temperatures will minimize the total processing time and are therefore desirable. Experiments were carried out to find out if rising the de-embossing

temperature affects part quality and process variation. Two (approximate) de-embossing temperatures 55°C and 75°C were chosen.

Part quality has also been shown to be sensitive to embossing force. Because exerting force to a certain value within the load cell range does not introduce extra cost, either in terms of time or energy the maximum embossing force of 800N is chosen.

Part quality turns out not to be sensitive to embossing velocity, so, the highest embossing velocity in the previous experiments, 1000N/min, is chosen.

In general, the design of the experiments is a 2x2 design, shown in Table 1. The four situations are indicated as 'L/L, L/H, H/L, H/H'. The value to the left of the slash stands for the embossing temperature, and that to the right stands for the de-embossing temperature. Letter 'L' stands for low value, and letter 'H' stands for high value.

Table5-1　　　　Design of Experiments

		Embossing Temperature	
		110 °C	120 °C
De-embossing Temperature	55°C	L/L	H/L
	75°C	L/H	H/H

5.3　Experiments and Measurements Validation

5.3.1 Variation Experiments

In order to do process variability assessment, 8, 8, 6 and 6 replicates of the four treatments in Table 1 are produced. For each part, the same channel as the one used in Chapter 4, shown in Fig. 5-2, is picked to do the measurements. Three scans of the same

channel within one part registration are done. The measurements data are shown in Table5-2.
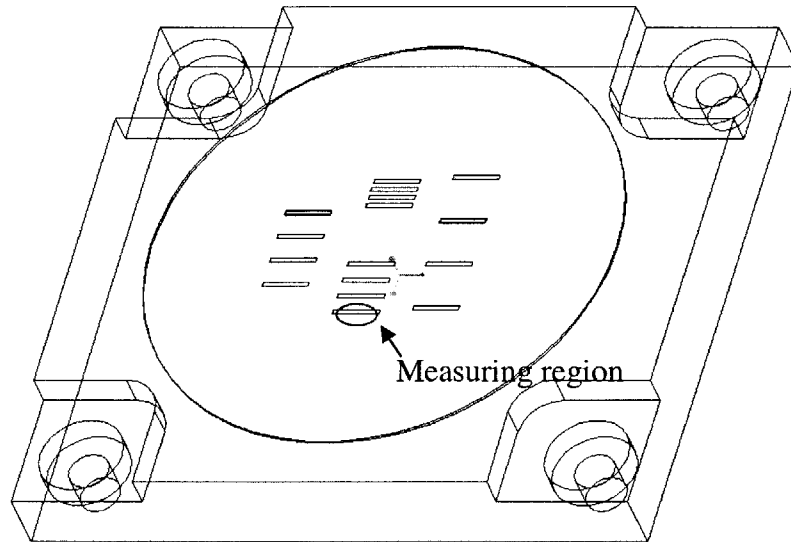
Figure 5-2   Measuring Region of Part

'TE' stands for the embossing temperature, and it can be well controlled to a constant temperature. 'TDE' stands for the de-embossing temperature. It is controlled manually, and it varies in a range of around 5°C. 'Depth', 'CWA' & 'CW' stand for the depth of the channel, channel wall angle, and channel width respectively. The number in the parenthesis indicates the ordinal number of scanning of channel profiles for a same registration of a part.

The average of three measurements of depth, channel wall angle and channel width are calculated for each run. Run charts of these averages are generated, shown in Fig. 5-3. The figures show that there are some variations in all the three part quality metrics. These variations come from process and measurement variations. In order to distinguish the process variation, measurement variance should be well estimated.

Table5-2   Measurements Data of Variation Experiments

#	TE	TDE	Depth(1)	CWA(1)	CW(1)	Depth(2)	CWA(2)	CW(2)	Depth(3)	CWA(3)	CW(3)
15_1	110.00	51.00	46.90	12.21	522.00	46.90	10.93	522.00	47.10	10.87	523.10
15_2	110.00	53.50	47.70	13.42	525.40	47.60	13.49	525.40	47.70	12.01	525.40
15_3	110.00	54.50	47.40	18.28	531.00	47.50	19.46	528.70	47.40	18.60	528.70
15_4	110.00	55.00	47.70	20.02	533.30	47.60	19.98	533.30	47.50	19.96	532.10
15_5	110.00	56.00	47.70	17.30	526.50	47.80	16.04	526.50	47.80	16.02	526.50
15_6	110.00	56.50	47.20	18.73	523.10	47.30	18.79	523.10	47.10	18.85	523.10
15_7	110.00	56.60	47.60	22.28	526.50	47.50	35.65	526.50	47.60	36.43	526.50
15_8	110.00	56.50	47.70	22.03	532.10	47.60	21.95	524.20	47.60	20.91	523.10
15_9	110.00	69.50	45.90	34.64	545.60	45.90	38.02	544.50	45.90	38.09	544.60
15_10	110.00	71.50	47.60	41.70	544.50	47.70	42.20	545.60	47.60	41.29	544.50
15_11	110.00	78.00	46.00	44.55	536.60	46.20	44.67	543.40	46.20	44.63	543.40
15_12	110.00	81.00	46.70	41.94	543.40	46.50	41.90	544.50	46.60	43.02	545.60
15_13	110.00	80.50	46.70	0.05	561.40	46.80	48.01	562.50	46.60	48.01	560.30
15_14	110.00	79.50	47.30	40.54	554.60	47.10	41.22	554.60	47.10	41.22	554.60
15_15	110.00	79.00	46.10	34.36	550.10	46.40	36.13	550.10	46.40	43.27	550.10
15_16	110.00	79.00	46.30	43.27	528.70	46.70	41.35	536.60	46.50	41.35	537.70
15_17	120.00	56.00	47.90	14.54	527.60	48.00	15.53	526.50	47.80	15.27	527.60
15_18	120.00	56.50	47.60	6.82	519.70	47.60	4.73	517.50	47.60	6.13	518.60
15_19	120.00	57.00	48.20	5.69	519.70	48.00	5.58	519.70	48.00	5.61	519.70
15_20	120.00	57.00	47.30	5.89	517.50	47.40	5.97	517.50	47.40	5.96	517.50
15_21	120.00	57.00	46.40	10.95	525.40	46.40	11.04	525.40	46.30	10.98	522.00
15_22	120.00	56.50	45.60	7.90	522.00	45.50	8.01	523.10	45.50	8.27	522.00
15_23	120.00	77.50	46.80	5.95	522.00	46.90	4.74	523.10	46.90	8.74	523.10
15_24	120.00	77.00	47.40	6.00	517.50	47.40	6.02	517.50	47.40	8.68	517.50
15_25	120.00	78.00	47.20	6.06	518.60	47.20	6.02	518.60	47.60	6.03	518.60
15_26	120.00	78.50	45.90	7.39	514.10	46.00	5.94	515.20	46.00	4.46	514.10
15_27	120.00	78.50	47.00	13.36	519.70	47.10	12.14	519.70	47.20	13.22	518.60
15_28	120.00	80.00	47.50	18.39	516.40	47.50	18.39	517.50	47.50	20.73	516.40

Depth vs Run number
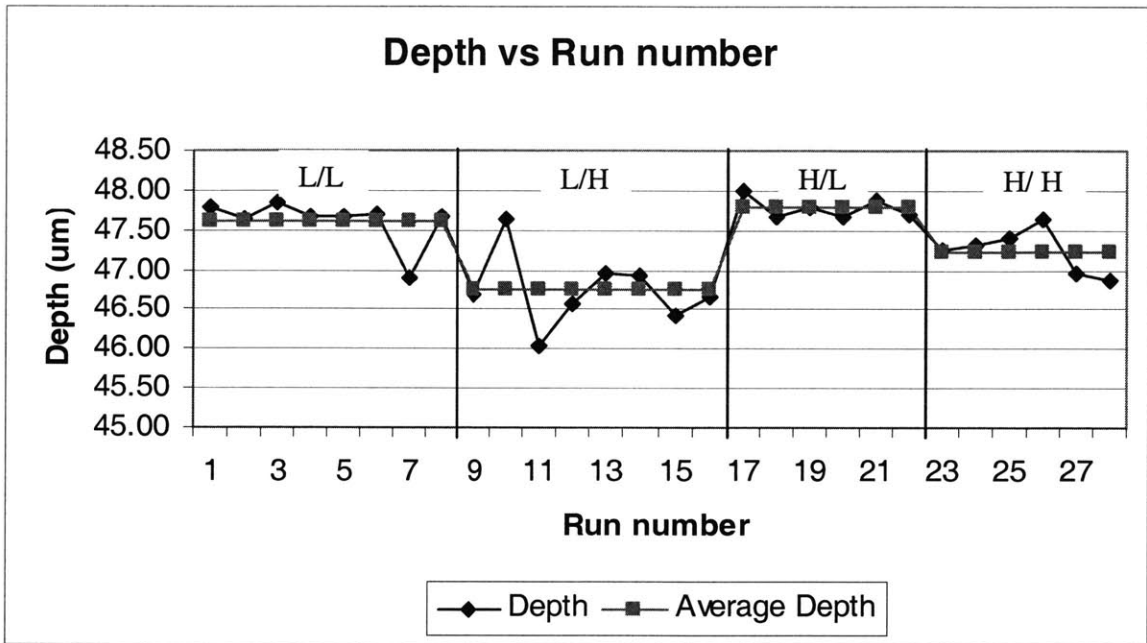
(a)   Channel Depth Run Chart

Channel Side Wall Angle vs Run number
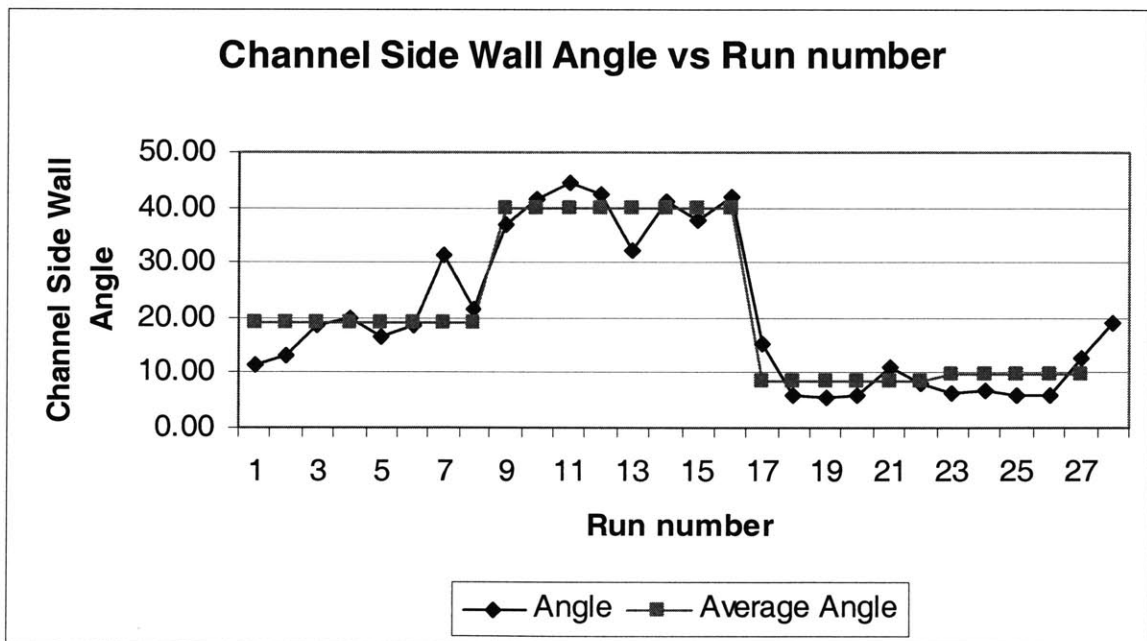
(b)   Channel Black Band Width Run Chart

Channel Width vs Run number
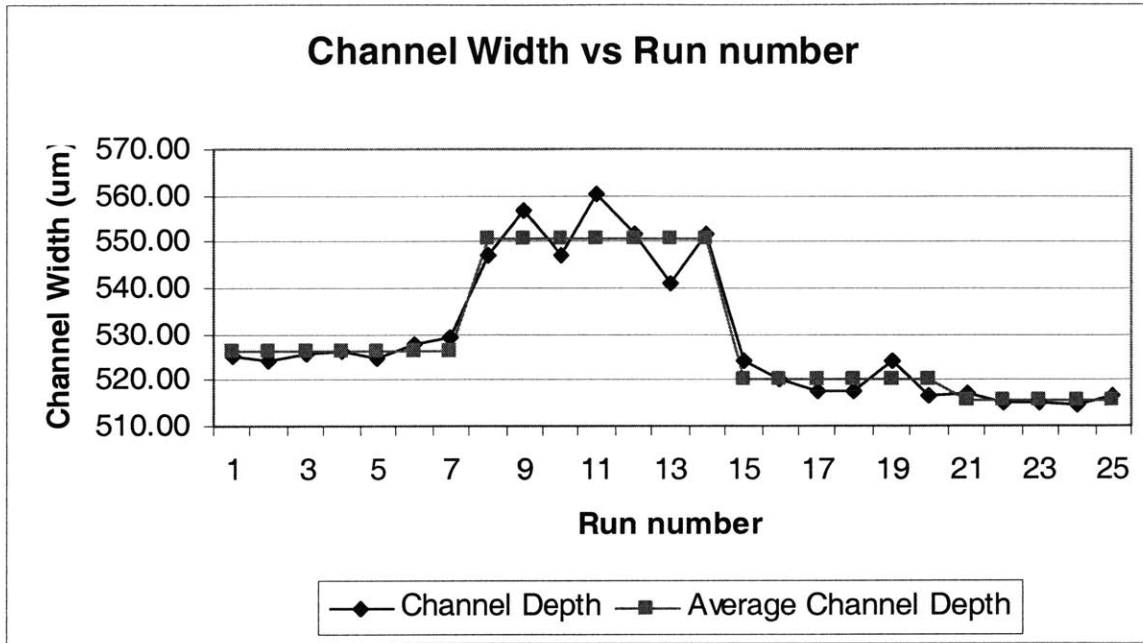
(c) Channel Width Run Chart

Figure 5-3   Channel Dimension Run Chart

5.3.2 Die Measurement Validation

Because the embossing die is made of copper, whose reflectivity is higher than that of PMMA, the measurements of the copper die with optical interferometer is more precise than that of PMMA parts. Thus, the copper die is used to do the measurement validation study.

There are three possible variation sources for the measurement variation: registration variation, scanning location variation, and scanning variation.

Registration variation occurs when reloading the die on the measuring table. Because each time when reloading happens, there is a need to adjust the orientation table to obtain uniform birefringence across focusing surface. This leads to a new scanning, and hence it results in different dimension data.

Each scan occupies only one fifth of the channel length (shown in Fig. 5-4).

Because the shape of the part is varying and there is no obvious mark to locate the

channel on the measuring table, it is hard to measure exactly the same part of the channel

in multiple registrations. In this situation, scanning location variation happens all the time.

~1m

5mm

Scan Position
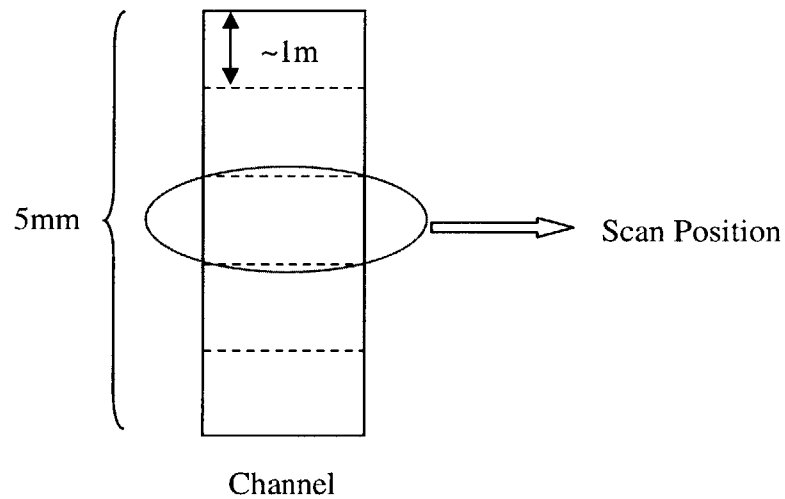
Channel

Figure 5-4   Scan Position on a Channel

The scanning variation is cause by non perfect repeating scanning of the Zygo

profilometer at the same channel location in the same registration. This is an inherent

measuring variation with any measurement instrument.

Experiments were designed to determine the registration, location, and scanning

variations. Each part is measured in 6 different registrations; since the length of the

channel is around 5 mm and the length of the interferometer scan is around 1mm, each

channel is divided into 5 non overlap 1 mm sections, and hence the 5 sections are

measured in each registration; for each section, 3 consecutive scanning are done.

The average of the three consecutive scans is calculated, and the relationship of

the tool depth, channel wall angle and channel width with the measurement position and

registration are shown in Fig. 5-5.
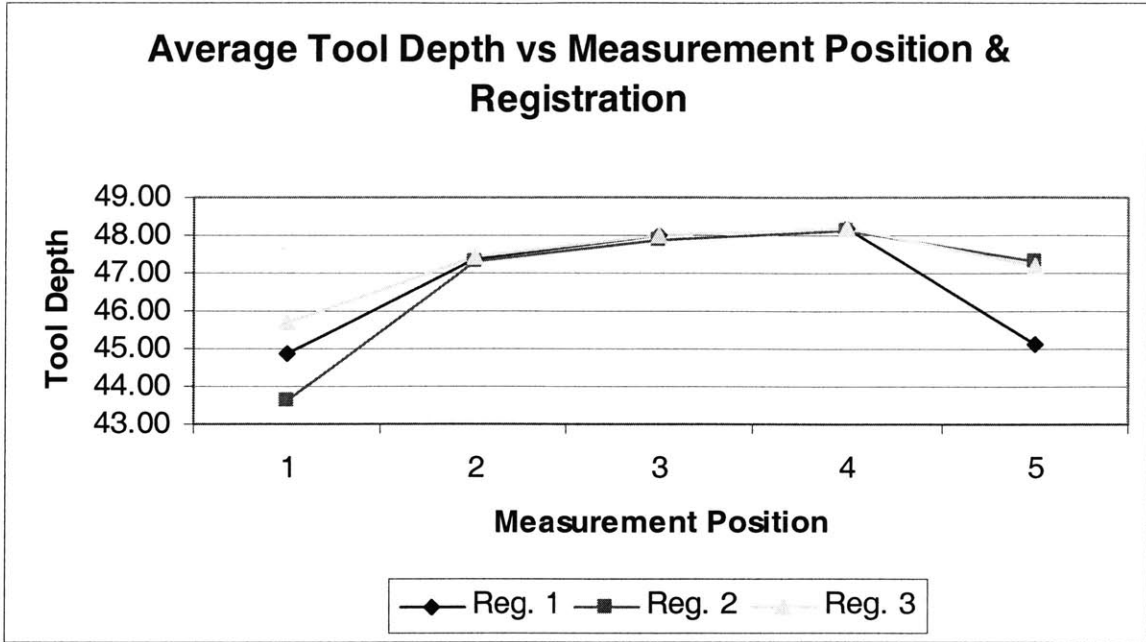
(a)   Tool Depth vs Measurement Position & Registration

(b)   Tool Channel Wall Angle vs Measurement Position & Registration
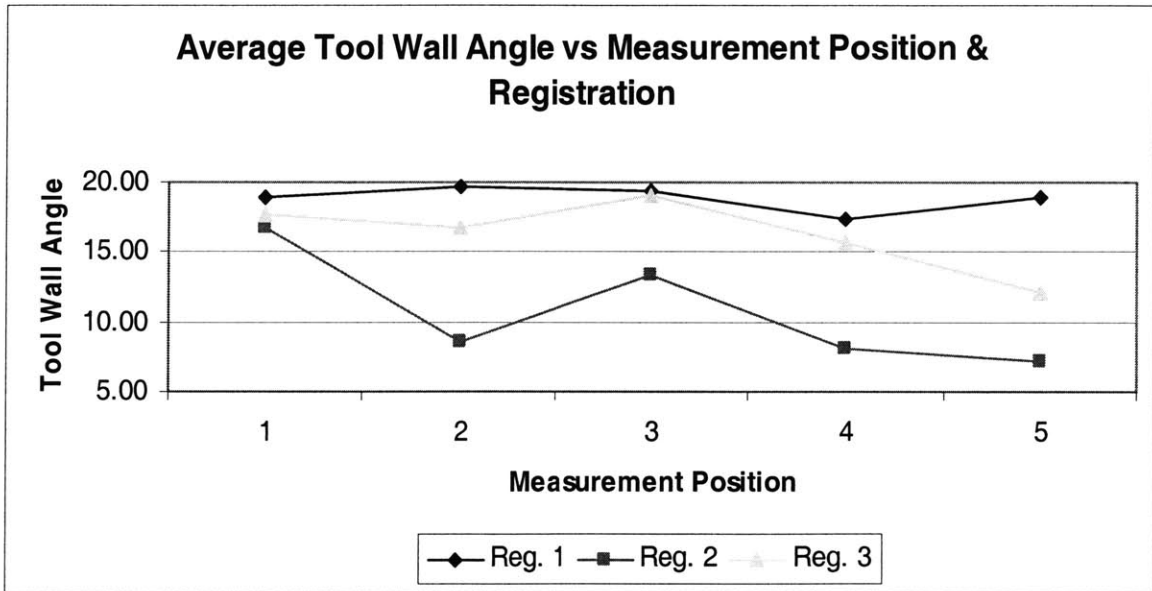
Average Channel Width vs Measurement Position & Registration
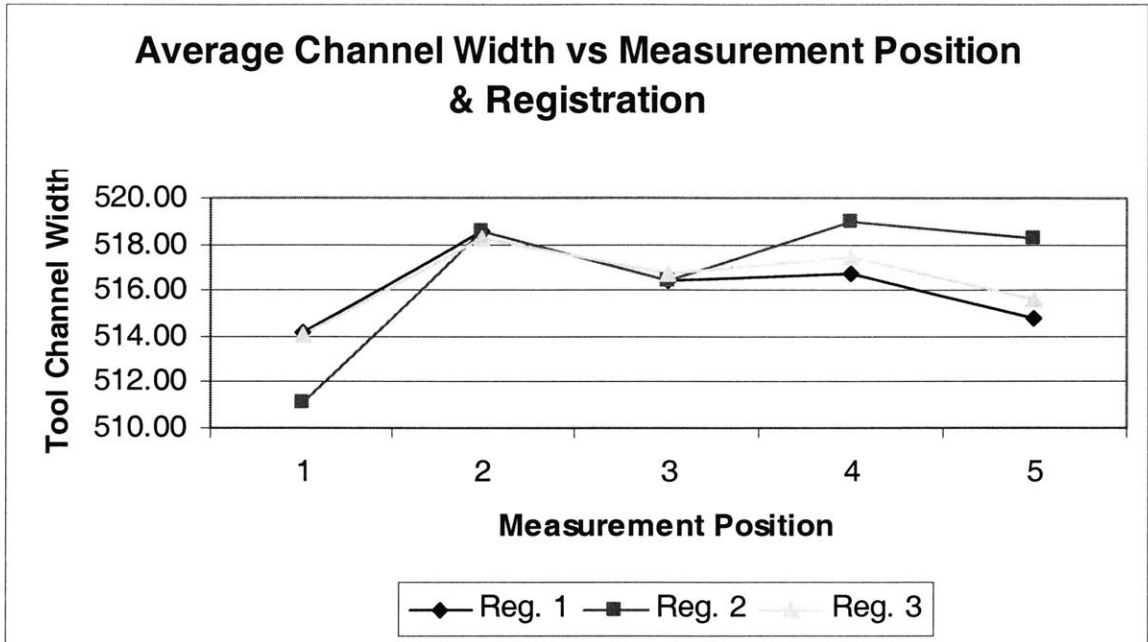
(c)   Tool Channel Width vs Measurement Position & Registration

Figure 5-5   Impact of Measurement Position and Registration on Tool Dimensions

Fig. 5-5 shows that there is some location variation among the 5 sections. These variations come from the variation of CNC machine manufacturing and hand polishing. The variations also vary with different channels randomly.

The discrepancy in registration of the same channel section is caused by the adjustment of the orientation of the measuring table. This adjustment is required due to the change of the location where the part is on the measuring table and also the change of the orientation of the part. It is also observed that the registration variations of the three middle sections are smaller than those of the two end sections. This is because the surface of middle section is flatter than that of the end sections because of less hand polishing of the middle section of the die was performed than that of the end sections, and the average height is less sensitive for flat surface than that of the curved surface. Therefore, the measurement is less sensitive to the registration in the middle of the channel.

The standard deviations of the channel dimensions of three scans at each position and registration are calculated, and Fig. 5-6 is obtained.
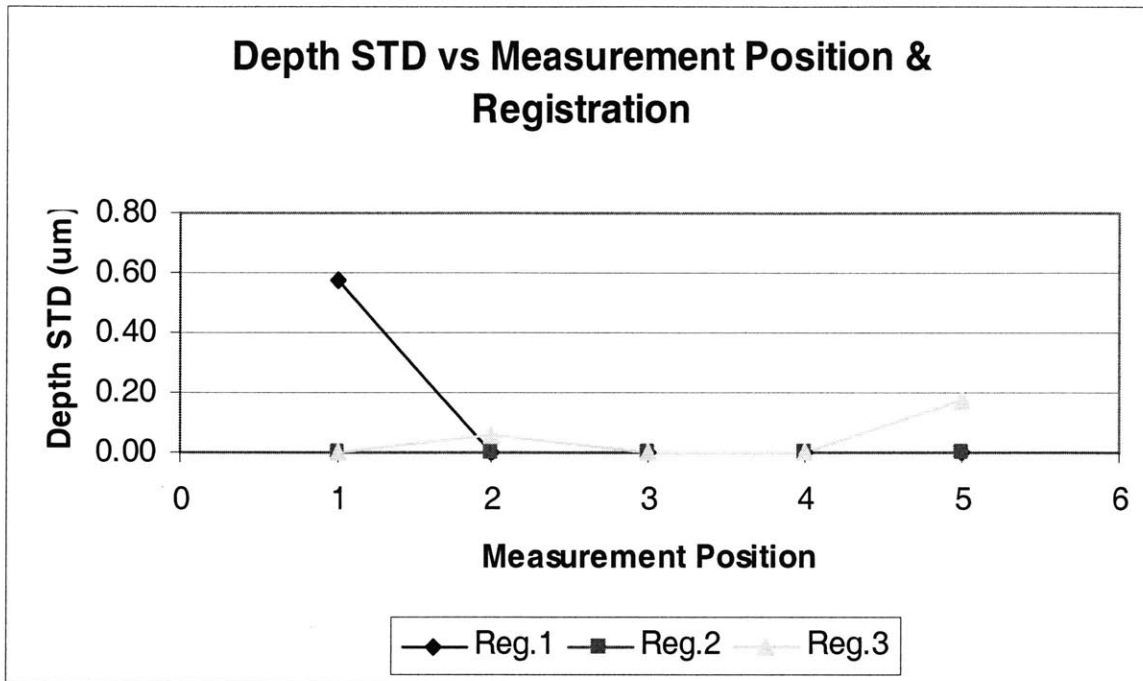
(a)   Standard Deviation of Three Scanning of the Same Channel Depth vs Measurement Position and Registration
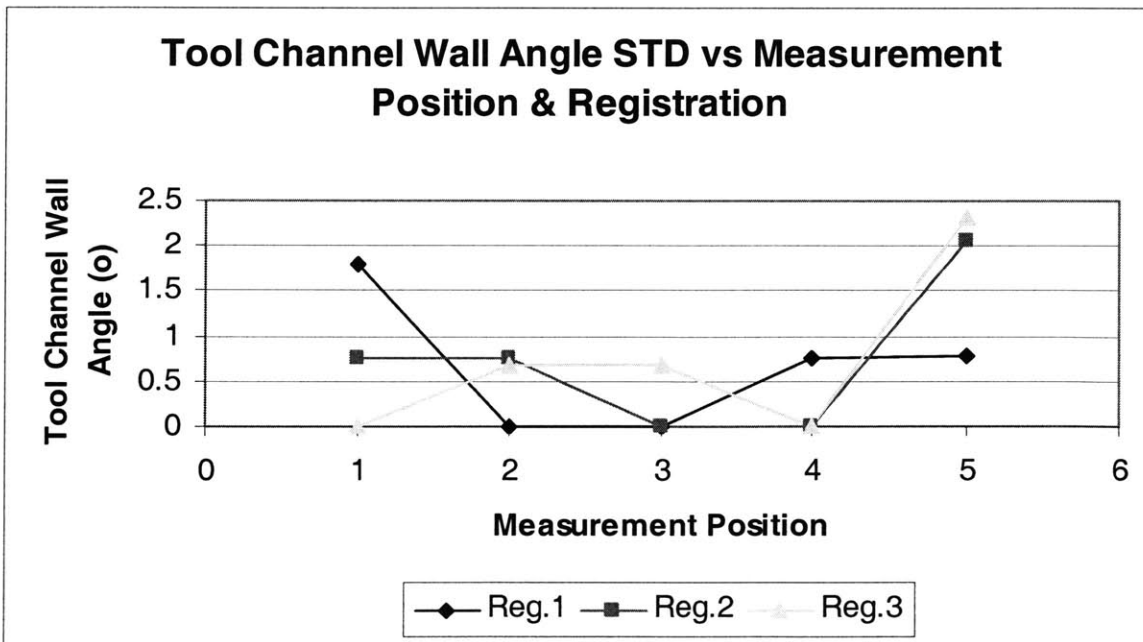
(b) Standard Deviation of Three Scanning of the Same Channel Wall Angle vs Measurement Position and Registration

Tool Channel Width vs Measurement Position & Registration
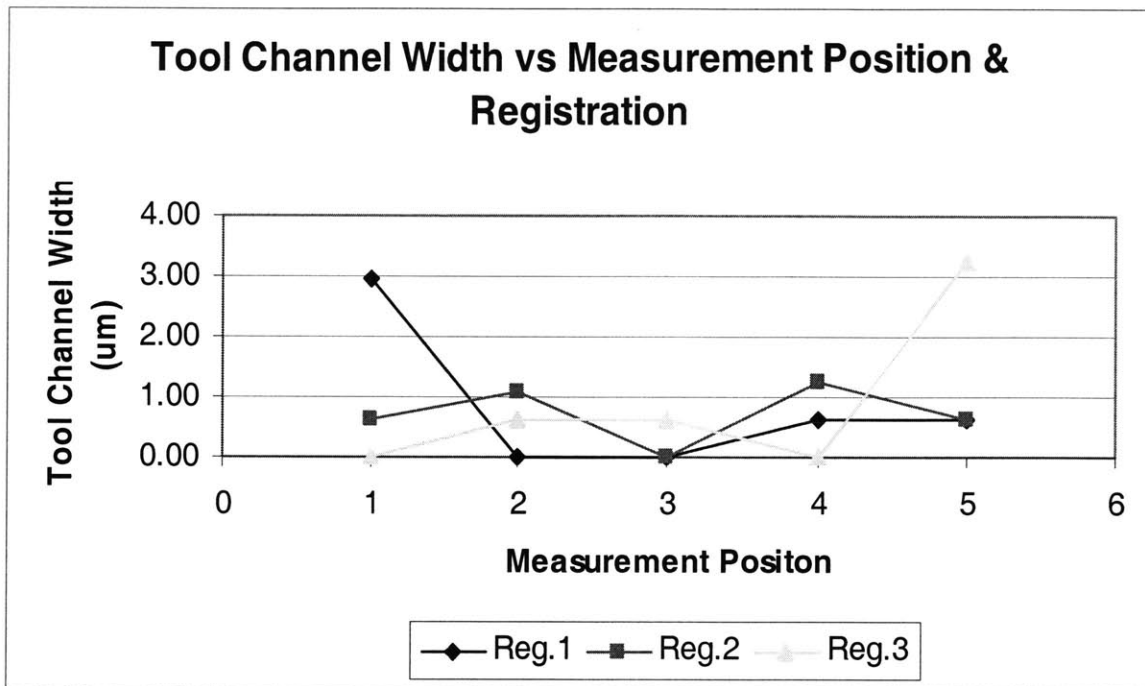
(c)   Standard Deviation of Three Scanning of the Same Channel Width vs Measurement Position and Registration

Figure 5-6   Impact of Scanning Variance on Tool Dimensions

Because of the fine resolution of depth measurements, the scanning standard deviations of depth are negligible. The scanning standard deviation in the lateral direction is in the order of microns. To be more specific, it is around 1 micron in the middle sections and 2 microns in the channel end sections. Fig. 5-6 shows that the standard deviations of three scanning at the channel end sections are bigger than the three middle sections.

In conclusion to this section, the middle section of the channel, section 3, should be the target measuring section in order to minimize the registration and scanning location variance. The standard deviation caused by registration is smaller than that caused by scanning; therefore, one registration and three scans of each channel will be used for each measurement to minimize the gage uncertainty.

5.3.3 Re-measurements of variation experiments

In order to verify the measurement accuracy, the variation experiment parts were re-measured twice on two consecutive days. The new measurements were done following the exact rules described in the previous section. The correspondent channel depth, channel wall angle and channel width data were input to excel in the format of Table 5-2. The average of the three scans of each quality spec of a channel is defined as the representative spec. The correlation of the channel depth vectors, for example, of the two measurements was calculated in order to see how well the measurements were replicated. The correlations are 0.7, 0.85, and 0.97 for channel depth, channel wall angle and channel width respectively. This shows that the two data sets are well correlated, and they follow a similar pattern. Thus, the first set of data is further studied and discussed in this thesis. The run chart of one of the two data sets and the tool data are plotted as shown in Fig. 5-7.
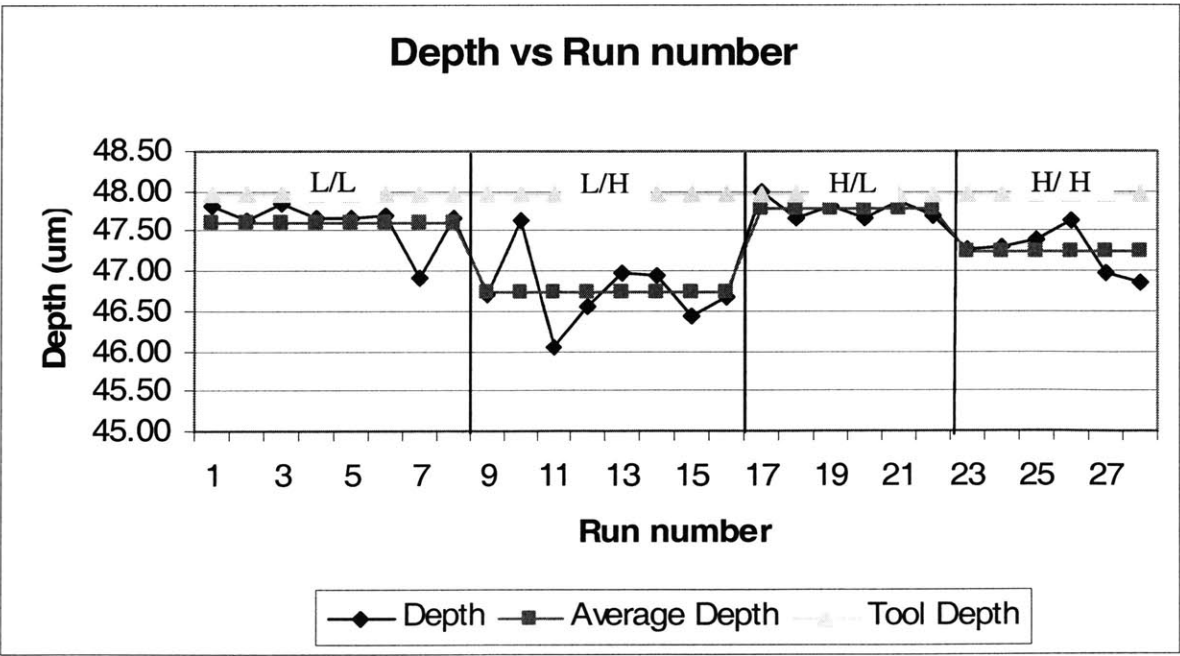
(a)   Run Chart of Channel Depth
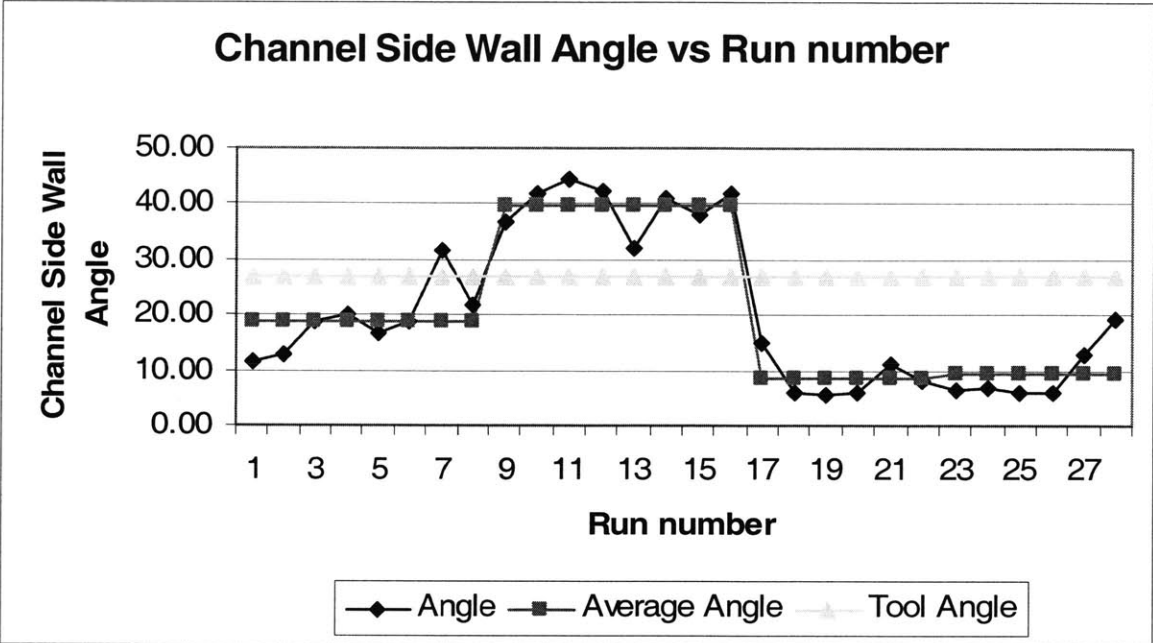
(b)   Run Chart of Channel Wall Angle
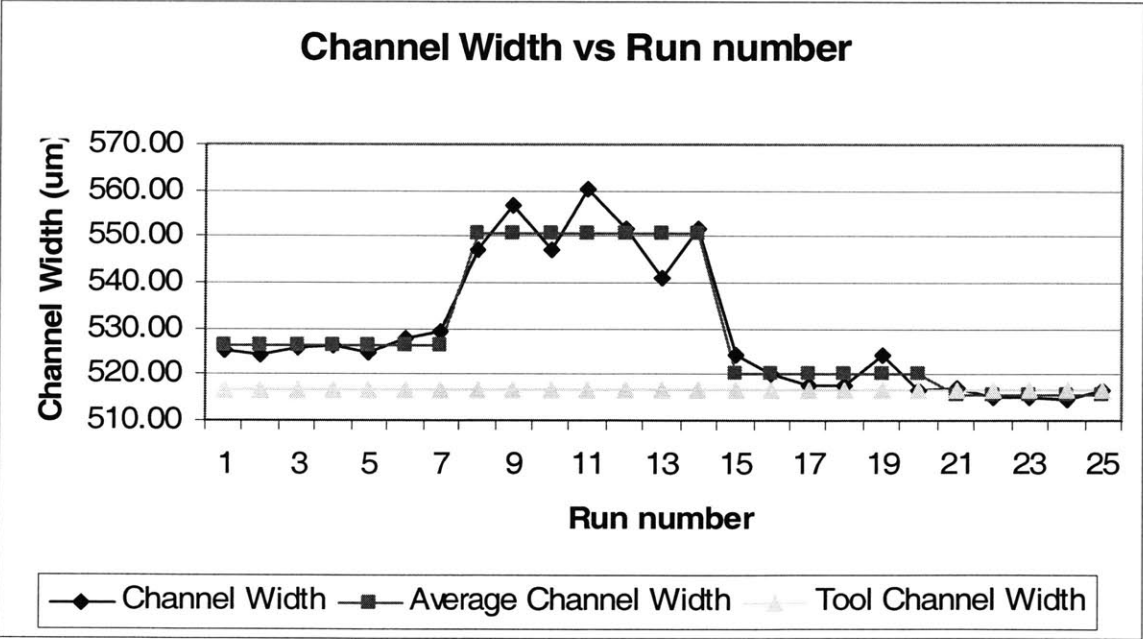
(c)   Run Chart of Channel Width

Figure 5-7   Run Chart of New Measurements of Variation Experiment Part Dimensions

Using One sigma criterion, part 7, 10 and 26 are detected to be outliers. They will be eliminated and will not be included in the analysis of process variance.

The channel depth is closest to that of the tool in the condition of H/L, and L/L condition comes next. Other two conditions, H/H and L/H result in significantly less depth.

Channel wall angles are smaller than that of the tool in most of the cases except the embossing condition of L/H. This is apparently caused by the shrinkage of the PMMA in the lateral direction. Smaller wall angle of the parts than that of the tool will result in difficult de-embossing. Thus, a channel wall angle of parts closer to that of the tool is desired.

The channel width chart shows a similar trend with that of channel wall angle chart, but there is some discrepancy in the relative position of the channel width with respect to that of the tool. Both embossing conditions of H/L and L/H result in parts with channel width very close to that of the tool. .

Excluding the outliers , the H/L embossing condition produces the parts with least variation within the same embossing condition (more details are given in section 5.4.2). Together with its capability to yield parts with channel depth and channel width close to those of the die, H/L is a very highly ranked potential embossing condition in the process window identified in chapter4. However, the channel wall angle at H/L is much smaller than that of the tool, which makes it hard to de-emboss. It is a trade off between the ability to de-emboss and process variation.

In order to test if the trends of are a general case, a second series of parts were produced and measured.

5.3.4 Variation Experiment Replicates

The next experiments were the replications of 15 series. The run charts are shown in Fig. 5-8.
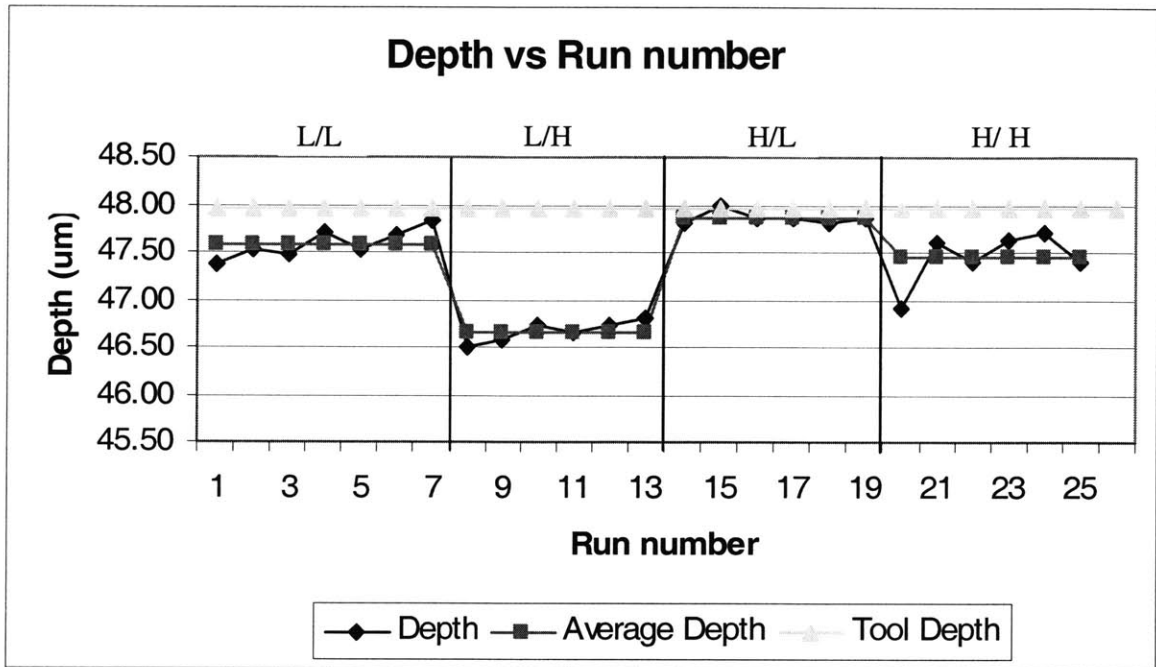
(a)   Run Chart of Channel Depth

(b)   Run Chart of Channel Wall Angle

Channel Width vs Run number
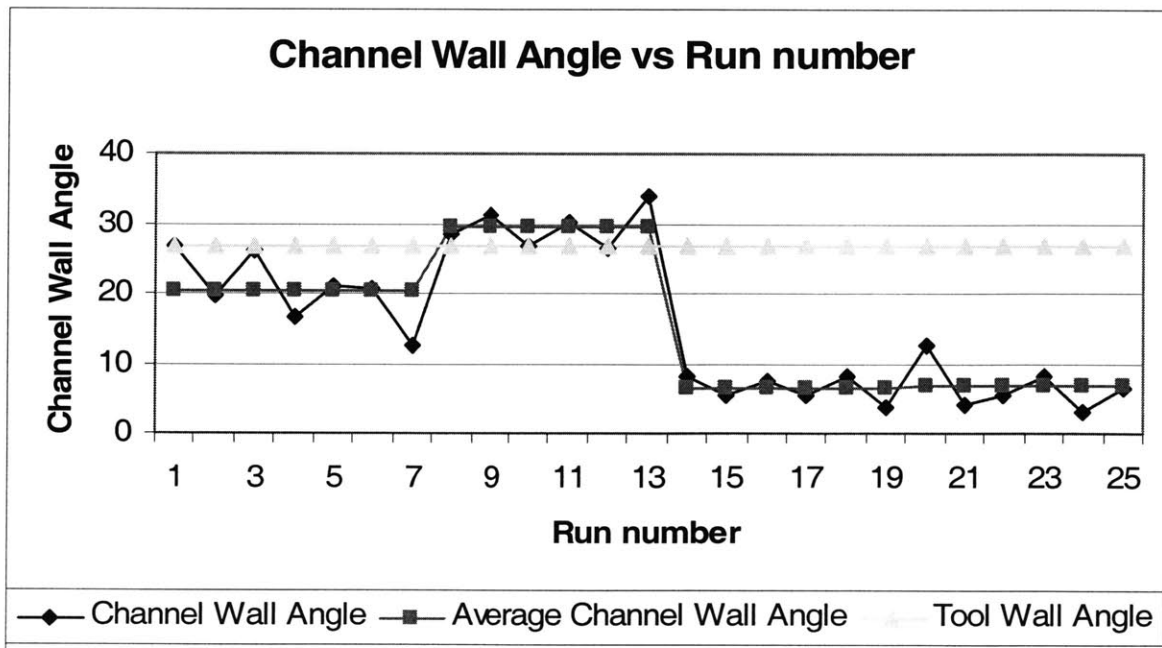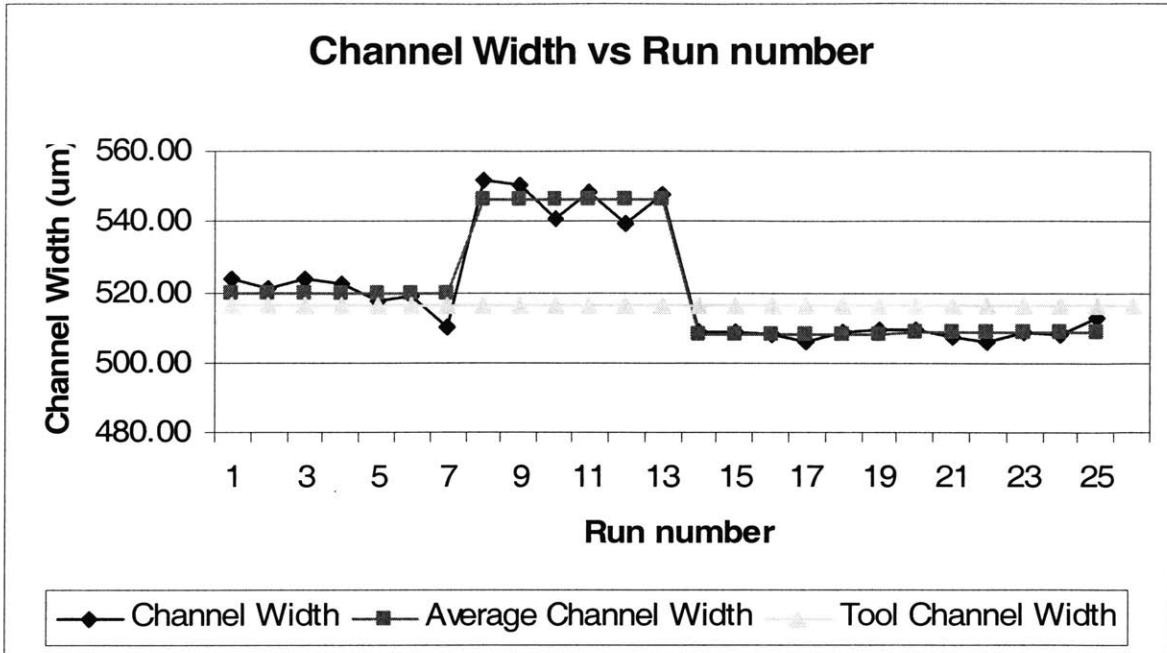
(c)   Run Chart of Channel Width

Figure 5-8   Run Chart of Measurements of 16 Series Part Dimensions

The trend observed in Fig. 5-6 is replicated in Fig. 5-7. Thus, the conclusion drawn from the embossed parts is valid.

5.4   Process Variation

5.4.1 Two-Way ANOVA

Both Fig. 5-6 and Fig. 5-7 show that embossing conditions have an impact on part quality. Whether this impact is significant was investigated using a two-way ANOVA analysis presented in this section.

The replicate data was used in this two-way ANOVA analysis. Take the depth analysis for example. The average depth of the parts embossed under identical embossing conditions is taken as the representative depth of that embossing condition. These representative depths are the elements of the Table 5-3. 'ET' stands for Embossing

Temperature, and 'DET' stands for De-Embossing Temperature. Minitab is used in doing

this Two-Way ANOVA analysis, and the result is shown in Table5-4.

Table5-3　　　　Channel Depth of 2×2 Design of Experiments

	ET	
DET	L	H
L	47.59	47.87
H	46.67	47.44

Table5-4　　　　ANOVA Analysis

Source	DF	SS	MS	F
ET	1	0.275625	0.275625	4.59
DET	1	0.455625	0.455625	7.59
Error	1	0.060025	0.060025	
Total	3	0.791275		
S = 0.245　R-Sq = 92.41%　R-Sq(adj) = 77.24%				

The F value for this analysis at a confidence interval of 95% is 4.35, and both

F(ET) and F(DET) are greater than 4.35. This means both embossing temperature and de-

embossing temperature have significant impact on channel depth, and the experimental

data is valid for a depth prediction model. Table5-5 shows the detail of this model.

Table5-5　　　　Design of Experiment Model for Channel Depth

Term	Effect	Coef
Constant		47.3925
ET	0.5250	0.2625
DET	-0.6750	-0.3375
ET*DET	0.2450	0.1225

The resulting model is given by Eqn 5-1:

$$\text{Depth}=47.39+0.26\times\text{ET}-0.34\times\text{DET}+0.12\times(\text{ET}\times\text{DET}) \qquad (5\text{-}1)$$

This equation shows that channel depth is positively proportional to embossing

temperature and negatively proportional to de-embossing temperature.

5.4.2 Process Variation

Standard deviation of quality metrics of replicated parts embossed at the same embossing condition can be used to evaluate process variation. The standard deviations of channel depth, channel wall angle and channel width of the parts embossed under the four embossing conditions are listed in Table5-6. From this table, the H/L condition is seen to result in the least variation.

Table5-6   Design of Experiment Model for Channel Depth

condition	Depth STD(um)	Angle STD(°)	CW STD(um)
L/L	0.16	5.06	4.78
L/H	0.11	2.84	5.00
H/L	0.07	1.86	1.03
H/H	0.29	3.42	2.33

5.5 *Conclusion*

Two embossing temperatures, 110°C and 120°C, and two de-embossing temperatures, 55°C and 75°C, form a 2^x2 designed experiment for both process variation and process window. The results show that the embossing condition of 120°C/55°C is the best manufacturing condition for micro embossing process with least process variation and most accurate forming of 50 x 500 micron channels in PMMA with our copper tool.

6

Conclusions and Future Work

6.1 Conclusions

This thesis studied the process window and variation of the Micro Embossing process. The tasks accomplished include:

1.   Building a copper embossing die with micro fluidic channels of 500μm width and 50μm depth;

2.   A dimensional quality assessment protocol using Matlab code based on measurements of embossed parts by a Zygo interferometer. Channel depth, channel wall angle and channel width were defined, and used as the quality metrics of embossed parts;

3.   The impact of process parameters, including embossing temperature, embossing velocity and embossing force, on embossed parts quality was identified. Results show that parts quality is most sensitive to embossing force and embossing temperature. It was found that maximizing the forces (800N in our case) achieved the best results at any forming temperature, applying it at a high rate (1000N/min) did not diminish part quality.

4.   Designed experiments with embossing temperatures of 110°C and 120°C and

de-embossing temperatures of 55°C and 75°C were carried out to determine

the most suitable embossing parameters for our material and tool. Good

replication of parts and small process variation makes embossing condition

120°C/55°C stand out. However, because the channel wall angle actually

decreased in this case, de-embossing could be a problem with increased of

aspect ratio of the channels.

6.2 Future Work

In order to lower the cycle time of Micro Embossing, and also to increase experiment efficiency in this thesis work, low embossing temperature, at which PMMA is in its glass transition state, was studied. Higher embossing temperatures, at which PMMA is in its fluid state, should be studied in the future.

Because of the lateral shrinkage of PMMA, channel wall angle of embossed parts tend to be smaller than that of die, when the aspect ratio of the features become higher, it will be difficult to de-emboss. This makes finding good de-embossing techniques an important research focus for manufacturing high aspect ratio parts.

A copper die was designed and manufactured because of its ease of manufacture. However, its surface roughness is not good enough to manufacture delicate micro devices. Silicon dies with smoother surface finish or metalized silicon tools will be necessary for future research. Also, in order to increase productivity, larger scale dies and denser feature designs on the dies are desired in a commercial manufacturing environment.

References:

[1]   Gwo-Bin Lee, and etc. Microfabricated plastic chips by hot embossing methods and their applications for DNA separation and detection, Sensors and Actuators, B75 (2001) 142-148

[2]   L.J. Heyderman, and etc. High volume fabrication of customized nanopore membrane chips, Microelectronic Engineering 67-68 (2003) 208-213

[3]   Brett R. Wenner, and etc. Biosensing on the CD Microfluidic Platform with Genetically Engineered Proteins, Society of Automotive Engineers, Inc. 2000, 1-6

[4]   L.J.Kricka, and etc. Miniaturization of analytical systems, Clin. Chem. 44 (1998), 2008-2014

[5]   Robert S.Wegeng, and etc. Process Intensification Through Miniaturization of Chemical and Thermal Systems in the 21st Century,

http://www.pnl.gov/microcats/aboutus/publications/microchemical/brenchleyfrankfurt99.pdf

[6]   Robert S. Wegeng, and etc. Opportunities for Distributed Processing Using Micro Chemical Systems.

http://www.pnl.gov/microcats/aboutus/publications/microchemical/aiche2.pdf

[7]   Antoine Daridon, and etc. Chemical Sensing using an integrated microfluidic system based on Berthelot Reaction, Sensors and Actuators B: Chemical, Volume 76, Issues 1-3, 1 June 2001, 235-243.

[8]   Todd Thorsen, and etc. Microfluidic Large-Scale Integration, Science, 18 October 2002, Vol 298, 580-584

[9]   Markus Rossi, and etc. Micro-optical modules fabricated by high-precision replication processes, Diffractive Optics and Micro-optics, June 3-6, 2002; Tucson/Paper DTuC1, Tops, vol.75, 108-110

[10]   Caliper Lifesciences, Inc.

http://www.caliperls.com/technology_partners/microfluidic/?PHPSESSID=b206a958439592e3d924d0a2feea0485

[11]   Younan Xia, et al. Complex Optical Surfaces Formed by replica Molding Against Elastomeric Masters, Science 1996 273: 347-349.

[12]   Younan Xia, et al., Soft Lithography, Angew. Chem. Int Ed. 1998, 37, 550-575

[13]   Marc A. Unger, et al, Monolithic Microfabricated Valves and Pumps by Multilayer Soft Lithography, Science, Vol 288, 7 April 2000, 113-116

[14]   Bing Xu, et al, Making Negative Possion's Ratio Microstructures by Soft Lithography, Advanced Materials, 1999, Vol.11, No. 14, 1186-1189

[15]   Noo Li Jeon, et al, Large-Area Patterning by Vacuum-Assisted Micromolding, Advanced Materials, 1999, Vol.11, No, 11, 946-951

[16]   R. Ruprecht, et al, Injection Molding of Micro Structured Components from Plastic, Metals, and Ceramics, Microsystem Technologies, 8 (2002), 351-358

[17]   V. Piotter, et al, Injection Molding of Components for Microsystems, Microsystem Technologies, 7 (2001), 99-102

[18]   V. Piotter, et al, Performance and Simulation of Thermoplastic Micro Injection Molding, Microsystem Technologies, 8 (2002), 387-390

[19]   H. Lorenz, et al, Fabrication of Photoplastic High-aspect Ratio Microparts and Micromolds Using SU-8 UV Resist, Microsystem Technologies, 4 (1998), 143-146

[20]   V. Piotter, et al, Injection Molding and Related Techniques of Fabrication for Microstructures, Microsystem Technologies, (1997), 129-133

[21]   Ruprecht R, et al, Injection Molding of LIGA and LIGA-Similar Microstructures Using Filled and Unfilled Thermoplastics; SPIE Vol. 2639 (1995), 146-157

[22]   L. Lin, et al, Comparative study of hot embossed micro structures fabricated by laboratory and commercial environments, Microsystem Technologies 4 (1998) 113-116

[23]   L.J.Heyderman, et al, High volum fabrication of customized nanpore membrane chips, Microelectronic Engineering 67-68 (2003) 208-213

[24]   Y. Chen, et al, A non-destructive method for the removal of residual resist in imprinted patterns, Microelectronic Engineering 67-68 (2003), 245-251

[25]   A. Lebib, et al, Nanoimprint lithography for a large area pattern replication, Microelectonic Engineering 46 (1999), 319-322

[26]   http://www.jo-mikrotechnik.com/noframes/english/equip/hex2.htm

[27]   http://www.rdmag.com/features/0107nano.asp

[28]   "Hot Embossing is a technique of imprinting microstructures on a substrate (polymer) using a master mold (silicon tool)." PPT of the University of Texas at Arlington

[29]   N. Roos, et al, Nanoimprint lithography with a commercial 4 inch bond system for hot embossing, presented at SPIE's 26th Annual International Symposium Microlithography, Feb. 25-March 2, 2001

[31]   Mathew Dirckx, Master's Thesis, MIT 2005

[32]   Mandy B. Esch, Influence of master fabrication techniques on the characteristics of embossed microfluidic channels, Lab Chip, 2003, 3, 121-127

[33]   H Yang, et al, Ultra-fine machining tool/molds by LIGA technology Source: Journal of micromechanics and microengineering, 2001, 11, 94-100

[34]   Roberts, K. et al, The fabrication of an array of microcavities utilizing SU-8 photoresist as an alternative 'LIGA' technology, University/Government/Industry Microelectronics Symposium, Proceedings of the Thirteenth Biennial, 6/20-6/23, 1999, 139-141

[35]   R.W. Jaszewski, et al, The deposition of anti-adhesive ultra-thin Teflon-like films and their interaction with polymers during hot embossing, Applied Surface Science, 143, 1999, 301-308

[36]   Xing Cheng, et al, One-step lithography for various size patterns with a hybrid mask-mold, Microelectronic Engineering, 71 (2004) 288-293

[37]   Yoichi Murakoshi, et al, Micro hot embossing for high aspect ratio structure with materials flow enhancement by polymer sheet, Device and Process Technologies for MEMS, Microelectronics and Photonics III, Vol. 5276 (2004), 532-539.

[38]   Yi-Je Juang, et al, Hot Embossing in Microfabrication. Part I: Experimental, Polymer Engineering and Science, March 2002, Vol.42, No3, 539-550

[39]   Harry D Rowland, et al, Polymer deformation and filling modes during microembossing, Journal of Micromechanics and Microengineering, 14(2004), 1625-1632

[40]   G.M.Swallowe, et al, A study of the mechanical properties of PMMA and PS at strain rate of 10^{-4} to 10^{3} over the temperature range 293-363K, Journal of Physics, IV France 110 (2003), 33-38

[41]   L.J.Heyderman, et al, Flow behavior of thin polymer films used for hot embossing lithography, Microelectronic Engineering 54 (2000) 229-245

[42]   Yi-Je Juang, et al, Hot Embossing in Microfabrication. Part II: Rheological Characterization and Process Analysis, Polymer Engineering and Scince, March 2002, Vol.42, No. 3, 551-566

[43]   Chunmeng Lu, et al, Analysis of Laser/IR Assisted Micro-embossing, Polymer engineering and science, 2005, Vol.45, No.5, 661-666

[44]   Wei Zhang, et al, Multilevel nanoimprint lithography with submicron alignment over 4 in. Si wafers, Applied physics letters, 2001, Vol. 79, No.6, 845-847

[45]   H.-C. Scheer, et al, A contribution to the flow behavior of thin polymer films during hot embossing lithography, Microelectronic Engineering, 56 (2001), 311-332

[46]   Donggang, Yao, et al, Cold Forging Method for Polymer Fabrication, Polymer Engineering and Science, October 2004, Vol.44, No.10, 1998-2004

[47]   Ganesan, Master's Thesis, 2004, MIT

[48]   L.A.Domeier, Microscreen-based replication of electroforming micromolds, Microsystem Technologies, 8 (2002), 78-82

[49]   Nici Ames, presentation for committee meeting.

[50]   Grant Shoji, Modeling and Control of a Hot Micro-Embossing Machine, MIT Master of Science of Mechanical Engineering, 2006

[51]   Kunal Thaker, Design of a Micro-Fluidic Functional Testing System for Process Characterization of a Hot Micro-Embossing Machine, MIT Master of Science of Mechanical Engineering, 2006

Appendix I

Fluidic Platen Heat Transfer System Design for Hot Micro Embossing Process

AI-1. Abstract

Hot embossing is a forming technique that shapes a plastic polymer part (*viz.* PMMA) by heating this part and pressing a die onto it. As in most thermal processes, the time required for heating and cooling the part are often the bottlenecks of the process and affect the throughput considerably. Understanding how to minimize these times could allow better identification of ultimate production rates, and would also enable faster experimentation in our current research work. Concurrently, production time should not be detrimental to part quality and an important factor that must be considered as it affects quality is temperature uniformity. A fluidic platen heating system was proposed to shorten the thermal cycling time and a prototype was made. Heat transfer experiments were carried out on a prototype and statistical analysis was performed. At the same time, a Finite Element Analysis (FEA) model was established to carry out heat transfer simulation. The results of the experiments and of the simulations were in agreement and proved that a proper FEA model was a good approximation of the real system. To optimize the temperature uniformity which directly affects final product quality, this FEA model was applied to some virtual experiments. By considering both thermal time and temperature uniformity, a 4mm copper platen with four parallel 2mm channels was reported as the most desirable heat transfer system with a heating settling time of 22 seconds, a cooling settling time of 20 seconds and uniformity of 0.08 ° C given a heating fluid temperature of 65° C and a cooling fluid temperature of 25° C. These results compare very favorably to other commercial setups.

AI-2. Background

Because of the high market demand of micro-fluidic and micro-optical devices, the existing processes of embossing of thermoplastic materials are receiving a renewed attention. Micro embossing involves a one step process, where the thermoplastic polymer and the embossing tool are heated several degrees above the glass transition temperature T_g of that particular polymer, after which a controlled force is applied to the tool. With the force maintained during the embossing time, the polymer and the tool are cooled below T_g and the polymer is pulled apart from the tool. The cooling cycle continues (often with a different cooling rate) until the polymer reaches the ambient temperature. The thermal cycle can be represented as in Fig.AI-1 (time not strictly to scale). Factors that determine the embossing time often include the particular working ability of the embossing machine, the material of the tool, the polymer, etc. Heating and cooling times are variables that depend on the heating and cooling scheme chosen for the system and this part is what we propose to minimize at first.
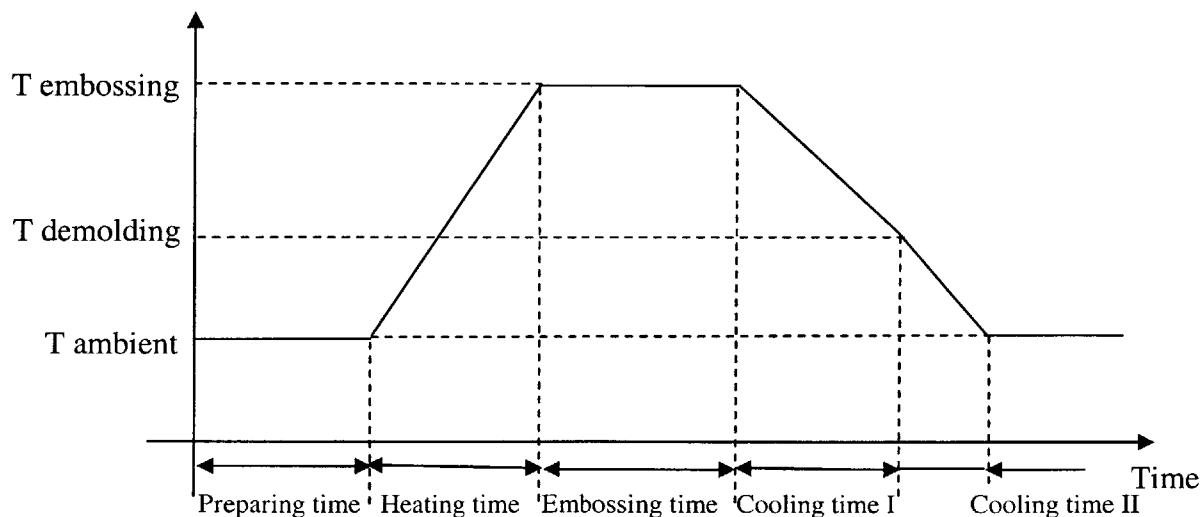
FigAI-1.   Thermal cycle

Indeed, the **thermal cycle time,** which determines the throughput of the process, could be dramatically improved if both the heating and cooling time could be reduced. Currently, two major commercial embossing machines are on the market: Jenoptik [2] hot embossing machine 'HX' serials and EV Group [3] micro embossing machine EV520HE. Heating and cooling times are given in the specifications of these machines: both the heating and cooling times of the Jenoptik machine are around 7 minutes, while the EVG micro embossing machine has a heating time of 6 minutes and a cooling time of 5 minutes. The bioMEMS lab of University of Texas at Arlington [4] has also already worked towards obtaining an optimal heating time, preventing hot spots and getting uniform heating on the tool and the polymer. They have used a 'heating cartridge' approach, that divides the polymer surface area into 5 zones and have controlled the heat flux of the 53 different heating cartridges separately. By running a Finite Element Analysis simulation they obtained a heating time of about 3 minutes and a cooling time of around 2 minutes. Our current laboratory setup has slightly lower performances with a heating time of around 15 minutes and cooling time of around 5 minutes.

Temperature uniformity is also an important factor because it can greatly influence the quality of the final product [4,5]. While both [4] and [5] recognized the importance of that particular factor, neither of them actually performed experiments to evaluate how the lack of uniformity could affect the quality of the product. In [4], temperature uniformity across an 8-inch polymer piece was around 3° C.. In [5], the temperature uniformity was maintained within ±1% (±2.25° C /255° C)

In our lab, temperature uniformity has also been an important concern[1]. In the initial design, which uses cartridge heaters and fluid cooling, a massive copper platen was used that kept variations as low as 3 ° C in that set up (shown later in FEA).

The following table sums up these different factors and their values:

TableAI-1. Thermal specification of existing machines

	Heating Time	Cooling Time	Embossing Temperature / Temperature Uniformity
Jenoptik HX Serials	7	7	N/A
EV Group EV520HE	6	5	N/A
Arlington bioMEMS group [4]	3	2	3 ° C
[5]	N/A	N/A	±2.25° C /255° C
Our group	15	5	3 ° C
Target ?	**1**	**1**	**1 ° C**

While improving temperature uniformity and reducing cycle time is the object of this report, there is trade-off between the thermal cycling time and the temperature uniformity. Faster heating and cooling times usually will cause inferior temperature uniformity in the transient states.

The work presented in this report focuses on choosing an effective heating and cooling approach that will shorten the heating and cooling times by an important factor and that would produce uniform heating, at least equivalent in performance to the mentioned references.

AI-3. Selection of heat transfer scheme

Cartridge heaters combined with a cooling fluid chiller is the most popular heat transfer scheme in the existing embossing systems [4, and our group]. FigAI-2 shows the current

---

[1] Although we seek high uniformity, the actual impact of non-uniform temperatures on embossing uniformity has yet to be quantified. This will be addressed in our future work.

embossing machine set up. Two cartridge heaters are placed in the holes at each side of the copper block, and the axes of the cartridge heater are parallel to those of the cooling channels. These axes are on a same plane that is parallel to the PMMA surface. During the heating cycle, the heaters are turned on, and the heat flux generated by the heaters is conducted directly to the PMMA surface, without much influence from the cooling channels. During the cooling cycle, the heaters are turned off. Because of the cartridge thermal mass inertia, the heaters continue serving as a heat flux source for a certain time, which will often slow down the cooling rate. Furthermore, because these cooling channels and the residue heat flux of the heaters, which are opposite heat sources, are working together asymmetrically, it could be harder to get a uniform temperature distribution across the polymer surface at the beginning of the cooling cycle.

Since the cartridge heaters are constant localized heat flux generators, it requires high thermal mass to conduct and accumulate the heat, and redistribute the temperature. By doing back the envelope calculation [6, bala's thesis], the copper block is required to be at least 6 centimeter thick in order to maintain approximately 3 ° C temperature uniformity, given the power of the heaters to be 400W. The heating and cooling time of the current set up is 15 and 5 minutes respectively (shown in TableAI-1), which needs to be improved imperatively.
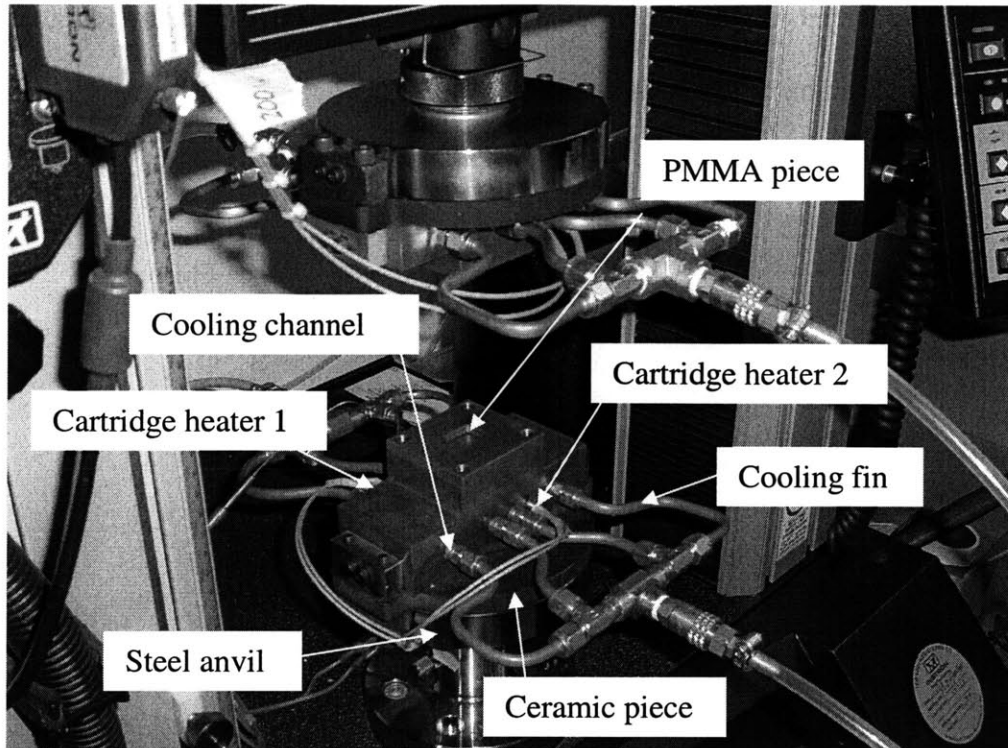
FigAI-2.   Current set up

Reducing the heating and cooling time consists in reducing the thermal mass of the system that is bound to change in temperature: copper block thermal mass and that of PMMA. The mass of PMMA is set to be constant in this project. However, the mass of the copper can be greatly reduced by using a constant temperature heat resource. A constant temperature heat resource only requires a media to conduct the heat but does less temperature redistribution work. Therefore, less thermal mass is required for the constant temperature resource case, and hence the thermal cycle time can be reduced dramatically.

An improved heat transfer system based on constant temperature resource is raised. Briefly, a copper block with parallel channels is designed as a heating platen. Hot fluid with constant temperature runs through the channels and the copper block can rapidly reach a uniform temperature, allowing the heating of the polymer placed on the copper platen, until the polymer reaches the embossing temperature. Right after the embossing process, cooling fluid runs

through the same channels and the polymer is cooled until it reaches the demolding temperature.

FigAI-3 is a representation of the new heating system.
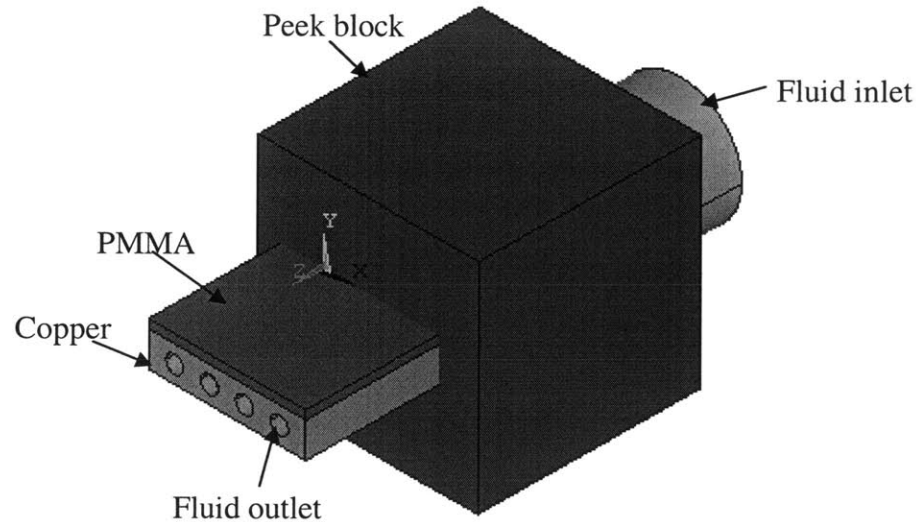
FigAI-3.   New heat transfer system

AI-4. Fluidic heat transfer system design

The fluidic heat transfer system design variables include the dimensions of the copper platen, dimensions of the channels and the design of heating and cooling curves. The best way to design this system is to use a design of experiments approach and see how each of these variables would affect the final result. However, to save on the cost and time of the experiments, a Finite Element Analysis (FEA) is done to simulate the prospective design schemes.

AI-4.1   Testing of the FEA model for current set up

Before we use FEA software to design our fluid – based heat transfer system, we should first test its ability to model an existing system. FigAI-2 shows the current cartridge based set up, whereas FigAI-4(a) shows the Ansys simulation model. The copper block is placed on a ceramic

piece and the ceramic piece is placed on the steel anvil. The two cartridge heaters are placed in the two holes in the copper block. Eight 'fins' are connected to the cooling channels in the copper block. In FigAI-2, these fins are curved, but the straightened fins in FigAI-4(a) behave the same way while making the modeling simpler. The input to this simulation model is the heat generation rate of the cartridge heaters, which is a total of 400W. Free convection is considered on all surfaces that are open to air, and pure conduction was the heat transfer mode within the solid. The initial temperature of the system was set to 25^0C.

NODAL SOLUTION
SUB =1
TIME=900
TEMP   (AVG)
RSYS=0
SMN =93.692
SMX =153.829

ANSYS
MAR 22 2004
17:31:08

93.692   107.056   120.42   133.784   147.147
     100.374   113.738   127.102   140.465   153.829
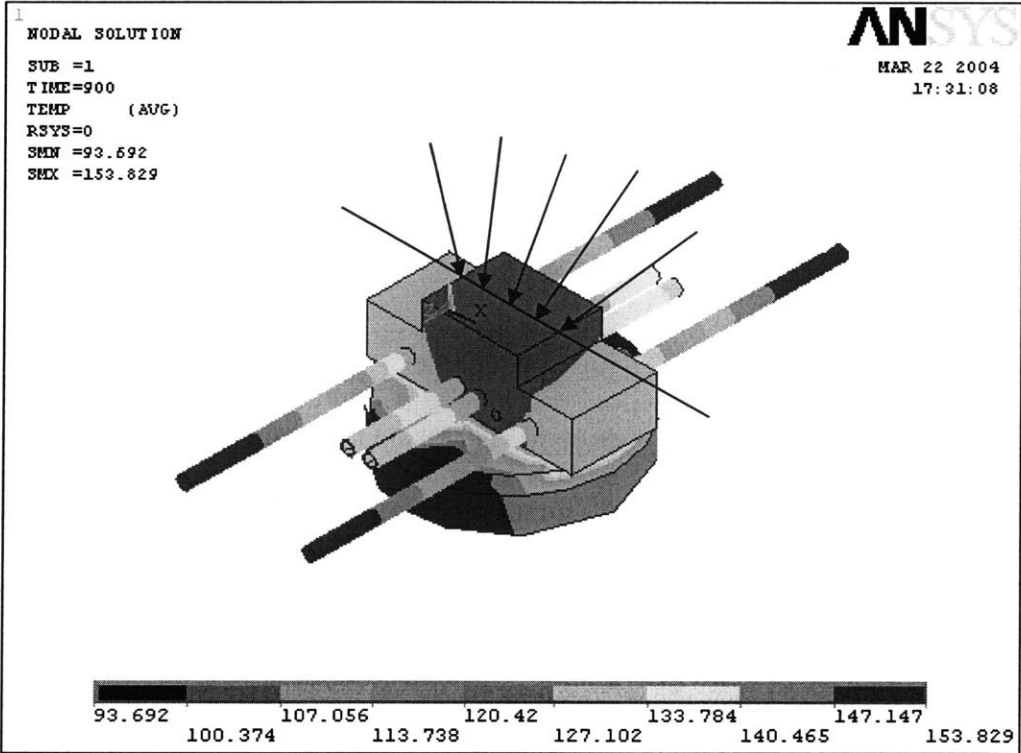
(a)   Ansys model of current set up
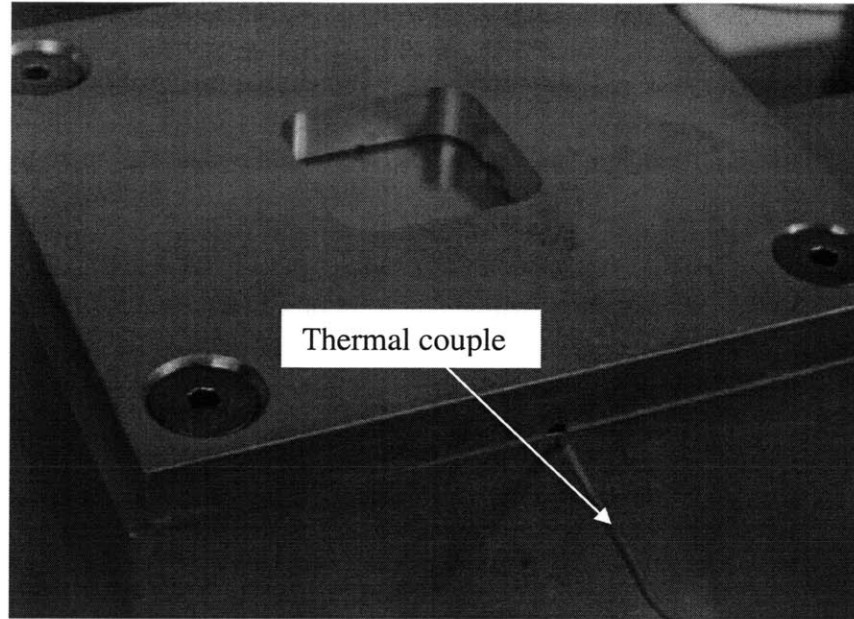
(b)   Temperature testing

FigAI-4.   Testing of current set up

TableAI-2.   Temperature of top surface of copper block

Time	P1	P2	P3	P4	P5	Temperature difference Tmax-Tmin ($^\circ$ C)
30	31.4	31.6	32.5	32.5	32.3	1.1
60	38.3	38.5	39.7	39.7	39.5	1.4
120	50.4	50.6	52.1	52.1	51.9	1.7
180	61.1	61.3	62.9	62.9	62.8	1.8
240	70.8	71.0	72.7	72.7	72.5	1.9
300	79.6	79.8	81.6	81.6	81.4	2
360	87.7	87.9	89.8	89.8	89.6	2.1
420	95.3	95.5	97.4	97.4	97.3	2.1
480	102.5	102.7	104.7	104.7	104.5	2.2
540	109.4	109.6	111.5	111.5	111.4	2.1
600	115.9	116.1	118.1	118.1	118.0	2.2
660	122.2	122.5	124.5	124.5	124.4	2.3
720	128.4	128.6	130.6	130.6	130.5	2.2
780	134.3	134.5	136.6	136.6	136.5	2.3
840	140.1	140.3	142.4	142.4	142.3	2.3
900	145.7	146.0	148.0	148.0	147.9	2.3

Data of the table was obtained following these methods: a thermal couple was inserted into a hole located very close to the top surface of the copper block, in order to test the open loop heating curve (see FigAI-4(b)). The temperature measured by the thermal couple can be assumed very close to that of the center point (P3) of the top surface of the copper block. In order to compare the FEA results with the experimental data, the temperature of point P3 was recorded every 60 seconds, shown in TableAI-2. Results are interpreted as such: the temperatures respond similarly to a simple first order system with a settling time of around 1700 seconds, and the steady-state temperature is around $305\,^0C$. The exponential model is fitted to the data in a least squares fashion and found to be:

$$T = 280(1 - e^{-t/1695}) + 25 \qquad\qquad (AI-1)$$

Leaving the cartridge heater on for 900 seconds, we obtain the temperature transient response. The settling time is found to be 1300 seconds, and the steady state temperature is around $300\,^0C$. The fitted model is:

$$T = 280(1 - e^{-t/1300}) + 26.33 \qquad\qquad (AI-2)$$
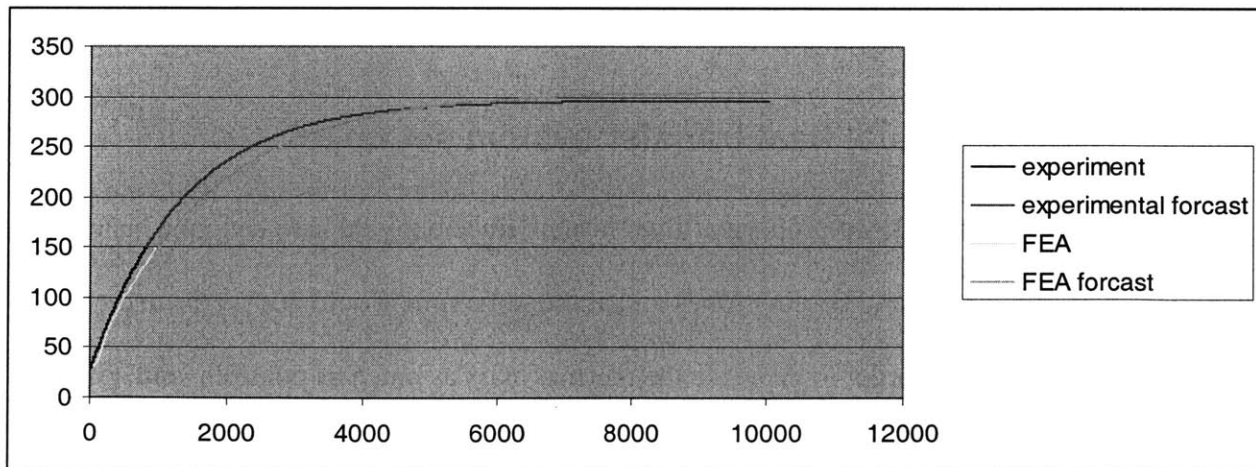
Fig5. FEA and experimental heating data

Because of the direction of the cartridge heaters and cooling channels, the temperature gradient is perpendicular to this direction. The temperatures of points P1, P2, P3, P4, and P5, which divide the line into four parts equally, are also recorded every 60 seconds to estimate the temperature uniformity of the top surface of the copper block, shown in TableAI-2. The last column of Table1 shows the subtraction of the maximum and minimum value at the same time point. At the time of 900 seconds, a temperature difference of around 2.3 ° C.

From the two first order system time response expressions and FigAI-5, we find that the steady-state temperatures are pretty close, but the settling time of the FEA model is larger than that of the experiment. The large difference in settling time between the experiment and the FEA suggests that most parameters (geometrical and material) are accurate and that the variations mostly come from the heater power.

However, around the embossing temperature, the FEA model and actual experiments were consistent in the order of minutes. In conclusion, we can use an FEA approach to do the simulation of our virtual set up.

AI-4.2. Novel virtual heat transfer system set up

As stated in section 3, we propose a 'fluid heater' since our goal is to design a heater that could minimize the heating and cooling times and at the same time would not sacrifice the temperature uniformity. In order to decrease the thermal mass as much as possible, and still create a part that could possibly be machined. we make a 1mm thick copper piece with 0.5mm diameter channels. Because we want to compare the FEA results with that of the actual experiment, and due to the manufacturing limitations, we try the 4mm thick copper with 2 mm diameter channels. The area of the top surface of the copper block is $20 \times 18 mm^2$, and $5mm$ of

that length is inserted into the 'peek' block and the rest (15mm) is hung outside. (See Fig 2) The polymer to be heated is 1mm thick PMMA with the top surface area around the same size as the copper block.

The embossing temperature has also been a research focus in other universities. Chou, in 1995, was the first one to proceed with embossing experiments; the embossing temperature was then $200\,^{0}C$ [6]. In 1997, he reduced this temperature to $175\,^{0}C$ [7]. Narasimhan [8] showed after several experiments that lower embossing temperatures, around $146\,^{0}C$ produce higher quality parts. Chen [9] used a statistical approach and found an optimal embossing temperature of $120\,^{0}C$. The current available literature results are therefore quite different and future research has yet to formulate a generally accepted definition for the optimal embossing temperature.

In theory, any temperature above the glass transformation temperature of PMMA is suitable for the embossing. However, because of experimental constraints (the adhesive used to glue the copper and peek can't stand high temperature), we find some difficulty heating up the PMMA part to the required temperature. Since we are choosing and testing only the heat transfer scheme, we set the hot fluid temperature at $65\,^{0}C$. With a higher temperature, only the magnitude of the thermal cycling time will be changed.

AI-4.3   FEA simulation of 'fluid heater'

AI-4.3.1   Copper platen

At first, we want to simulate the heat transfer properties of the copper platen (without PMMA on top of it). FigAI-5 shows the Ansys simulation model of the copper platen. A constant

uniform temperature distribution within the fluid channels at the heating fluid temperature is assumed.

Free convection is the major heat loss, and the boundary condition is the free convection with air at room temperature, at the top, bottom and on the two side surfaces.
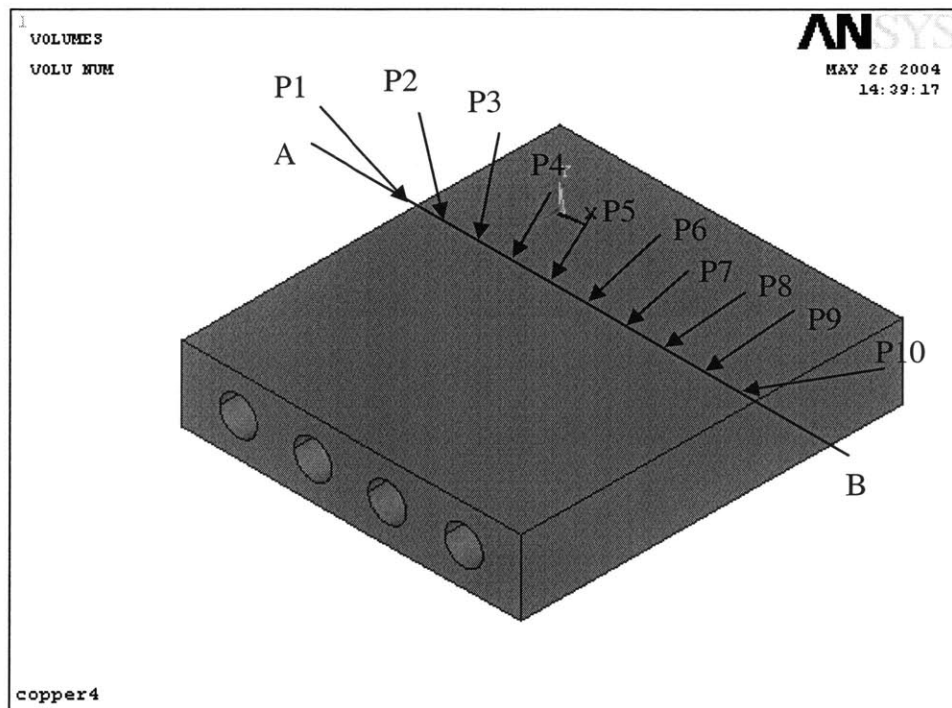
FigAI-5.   Ansys model of copper platen

Justification of the constant uniform temperature input assumption:

To justify this assumption, we will look at the temperature drop expected along the fluid channel at the expected heat loss rates for this setup.

Assume we used water as heating fluid, we had its mechanical properties as:

density $\rho = 1000kg / m^3$, heat capacity $C_p = 4200J / (kg \cdot k)$, viscosity $\mu = 0.9 \times 10^{-6} m^2$, heat conductivity $K = 0.610W / (m \cdot k)$

The diameter of the channel is 2mm. The Reynold's number should be less than 2300 so that the flow inside the channels can be considered as laminar flow. This limits the flow velocity to 2m/sec as shown in EqnAI-3

$$R_e = \frac{\bar{V}D/2}{\mu} < 2300 \Rightarrow \bar{V} < 2m/s \qquad (AI-3)$$

Where $\bar{V}$ is the average velocity in the channels.

The average heat transfer rate is given by

$$q = (\rho_{cu}\nabla_{cu}C_p\Delta T - h\Delta\bar{T}S_{cu})/t \qquad (AI-4)$$

where the density of copper is $\rho_{cu} = 8900kg/m^3$, the heat capacity of copper is

$C_{cu} = 380J/(kg.k)$, ∇_{cu} is the volume of the copper piece, h is the convection coefficient of the air (*calculated later*), and the convection surfaces area is

$s_{cu} = (0.018 \times 0.02) \times 2 + 0.02 \times 0.004 \times 2 \ m^2$

In order to get the practicable average heat transfer rate through out the heating process, we adopt the real experiments (*the experiments done using the 4mm copper, recorded by the infrared camera, and will be noted in section 5*) values. The settling time is estimated to be $t = 4$ s, so the average heat transfer rate is obtained through equation (AI-4) to be 20W. The average heat transfer rate causes the average temperature drop along the four channels during the heating cycle, so the average temperature drop could be obtained through the following equation:

$$\rho C_p(\bar{T}_{out} - \bar{T}_{in})\bar{V}(\frac{\pi D^2}{4}) = \frac{q}{4} \qquad (AI-5)$$

then $\bar{T}_{out} - \bar{T}_{in} = \dfrac{q}{\rho C_p\bar{V}\pi D^2} \approx 0.2C$

$0.2\,^0C$ is the transient average temperature drop, and it is small enough for us to ignore. In the steady state, the heat supplied by the fluid is only used to compensate the heat loss through convection, and this leads to the temperature drop to be on the order of millidegrees.

Convection coefficient:

From Bala's thesis, the convection coefficient of air can then be determined with the known Nusselt number:

$$h = \frac{N_u K_{air}}{l} \tag{AI-6}$$

where K_{air} is the conductivity of the air, L is the length of the copper piece, $N_u = 17.21$.

$$h = 17.21 \times 0.03 / 0.02 \approx 25 w / (m^2 \cdot k) \tag{AI-7}$$

Simulation results of heating copper platen:

The initial temperature of the copper platen is $25\,^0C$, and the temperature of the inner area of the four channels is set to $65\,^0C$ at time 0. This model will calculate a new temperature for each finite element node every 0.01 second. FigAI-6 shows the temperature distribution at the end of 0.5 second. We can see from the figure that the temperature is very uniform.
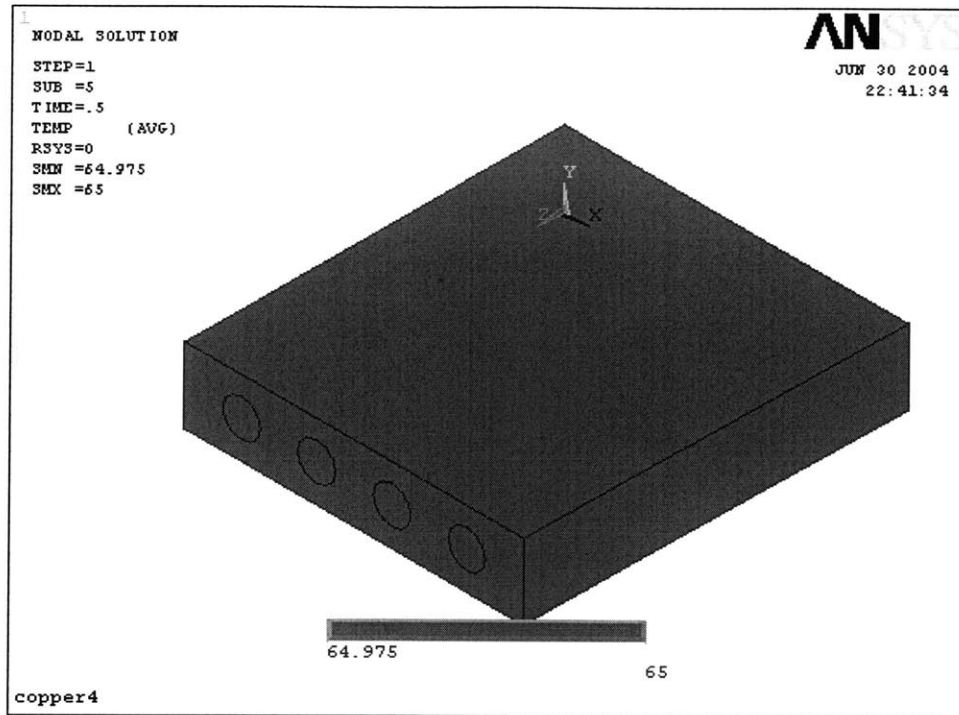
FigAI-6.   Simulation result of copper platen at 0.5 second

In order to estimate the uniformity of the whole surface, we record the time dependent

temperatures of 10 points (P1, P2, ...,P10) on line AB, which is the center line in 'X' direction

on top of the copper platen (the coordination is given by Ansys model, shown in FigAI-6). The

10 points are located evenly on line AB. TableAI-3 shows the temperatures of the 10 points, and

they are recorded every 0.1 second. The last column shows the temperature difference between

the maximum and minimum values of the same row/time. This temperature difference goes

below 1 degree at 0.3 second, and at the end of 1 second the gap was on the order of a

millidegree.

FigAI-7. shows the heating curve of the 10 points, 'Series1 to Series 10' represent the

heating curve of 'P1 to P10' respectively. From this figure, we find that the 10 points actually

fall into 3 groups according to the time response curve. Among the 3 groups, the response trend

is the same but has different settling time. The dominant settling time of the copper platen is around 0.3 second.
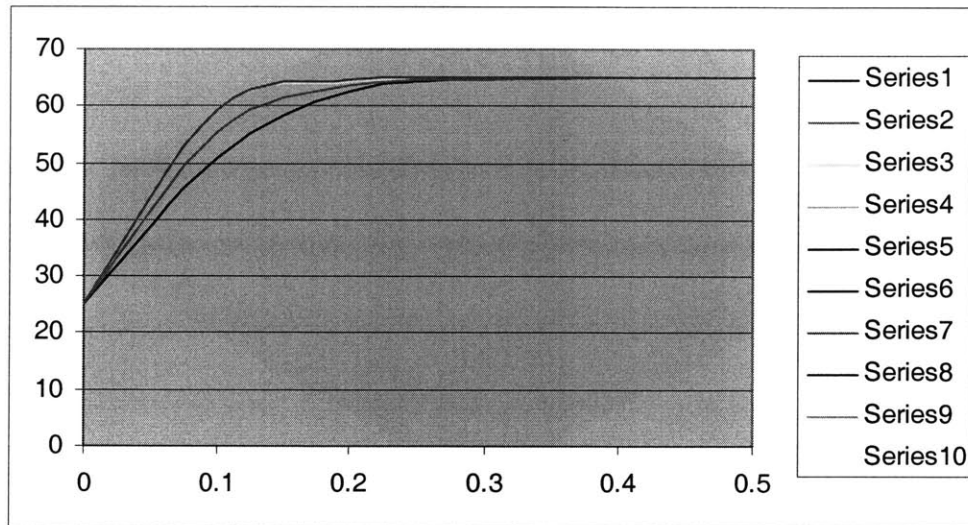
FigAI-7. Heating curve of copper platen

TableAI-3.　　　Temperature of top surface of copper platen

Time(s)	P1	P2		P10	Temperature difference Tmax-Tmin
0	25	25	25	25	0
0.1	50.8012	55.6741	...	50.7069	4.9672
0.2	62.4264	63.5367	...	62.4172	1.1195
0.3	64.5465	64.752	...	64.5455	0.2065
0.4	64.9125	64.9526	...	64.9124	0.0402
0.5	64.975	64.9864	...	64.9749	0.0115
0.6	64.9856	64.9921	...	64.9855	0.0066
0.7	64.9874	64.993	...	64.9873	0.0057
0.8	64.9877	64.9932	...	64.9876	0.0056
0.9	64.9877	64.9932	...	64.9877	0.0055
1	64.9877	64.9932	...	64.9877	0.0055

AI-4.3.2　　Copper + PMMA

Now, a PMMA piece is added onto the top surface of the copper platen. The simulation model is shown in FigAI-8. The initial temperature of both copper and PMMA is $25\,^0C$, and the temperature of the inner area of the four channels is set to $65\,^0C$ at time 0. This model will calculate a new temperature for each finite element node every 3 second. By simulation, we

obtained the heating curve shown in figAI-9. The "Series1 to Series 10' represent the heating curve of points 'P1 to P10' respectively. The 10 points are located evenly on the center line AB.
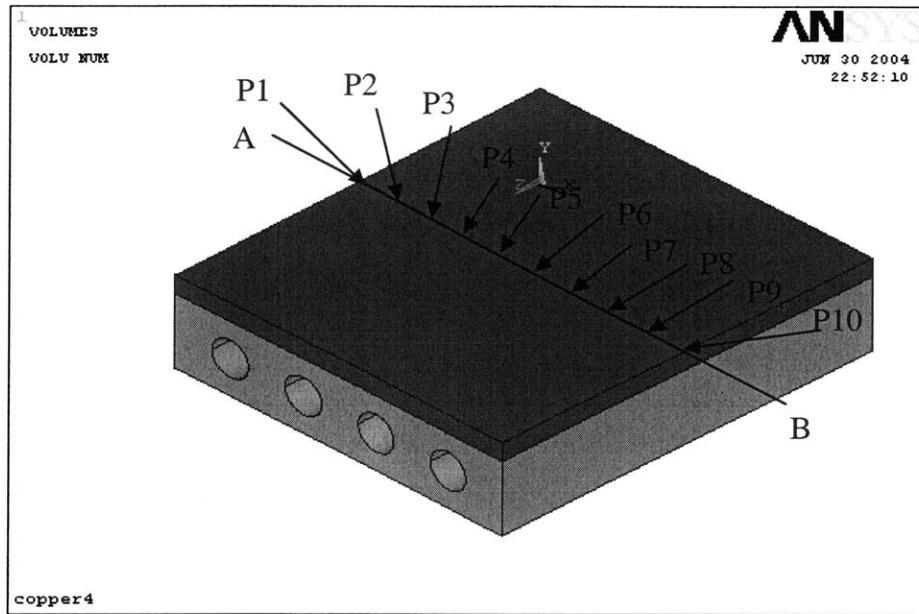
FigAI-8.　　　Ansys model for copper platen and PMMA piece
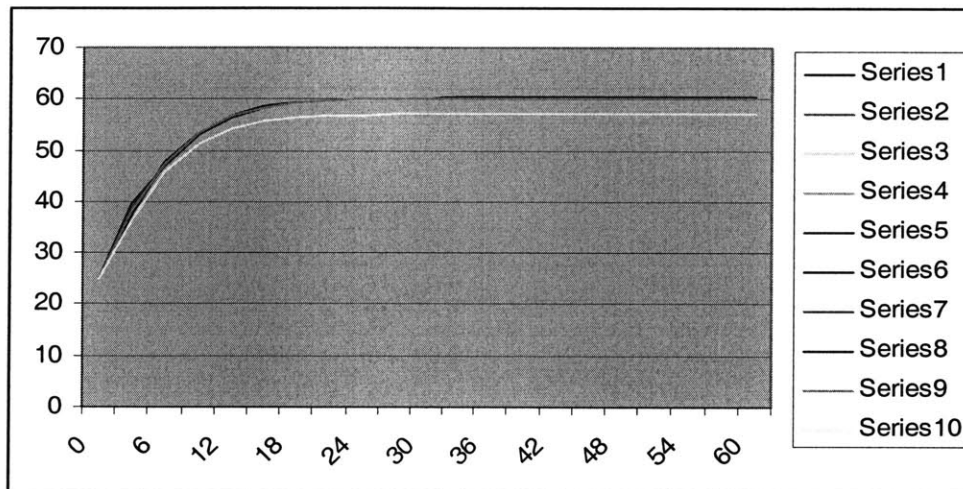
FigAI-9.　　Heating curve of PMMA on copper heater

The lower heating curve shows that the temperature of the edge of PMMA piece is lower due to the convection. Because of the convection at the surfaces, the top surface temperature saturates at around 60 degrees. The settling time of PMMA is around 22 second. Compared to the settling time of the copper platen, this settling time is dominant. If we don't use the copper platen as a heater, and instead, we just apply a uniform constant temperature source to the bottom of the PMMA piece, we get the heating curve shown in FigAI-10.
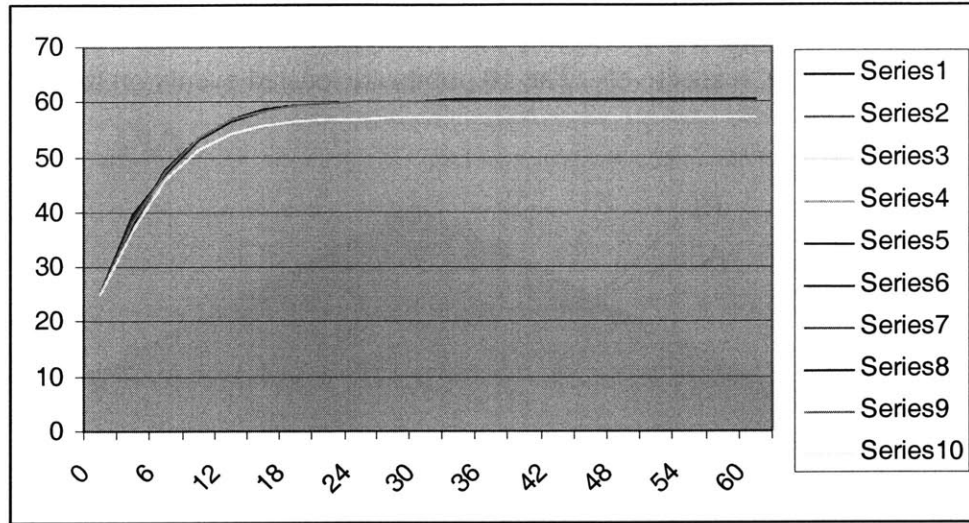
FigAI-10.   Heating curve of PMMA

Comparing these two figures, we can see that the heating process of the PMMA from the

bottom surface is a little bit faster than using the copper heater. Subtracting the temperature of

these two models, we get the temperature difference, shown in TableAI-4:

TableAI-4.   Temperature difference of two FEA models

time(s)	Temp.			Mean	STD
0	0	0	0	0	0
3	0.0402	0.0948	...	0.07525	0.051072
6	0.1147	0.0562	...	0.06163	0.025015
9	0.0924	0.0439	...	0.04352	0.01845
12	0.0634	0.0302	...	0.02727	0.013966
15	0.0443	0.0212	...	0.01746	0.010551
18	0.0332	0.0156	...	0.01175	0.008514
21	0.0269	0.0122	...	0.00846	0.007336
24	0.0233	0.0103	...	0.00658	0.006682
27	0.0214	0.0092	...	0.00551	0.006352
30	0.0203	0.0085	...	0.0049	0.006147
33	0.0197	0.0081	...	0.00455	0.006043
36	0.0194	0.0079	...	0.00437	0.005996
39	0.0192	0.0078	...	0.00428	0.005969
42	0.0191	0.0078	...	0.00422	0.005951
45	0.0191	0.0078	...	0.00419	0.005958
48	0.019	0.0077	...	0.00414	0.005934
51	0.019	0.0077	...	0.00416	0.005926
54	0.019	0.0077	...	0.00414	0.005934
57	0.019	0.0077	...	0.00414	0.005934
60	0.019	0.0077	...	0.00416	0.005931

We can see that the temperature difference is so little that we can conclude that the hot water heated up the copper very fast and nearly immediately (less than half second later) the copper acted as a uniform constant temperature source. If we decrease the thickness of the copper piece, it will only decrease the settling time of the copper and will not change that of the PMMA piece. This means that we don't need to make a tiny copper heater, but on the other hand, we should choose a proper thickness for it, and test its mechanical properties, such as the deformation under pressure, to see if it meets the strength requirement.

At the end of 60 seconds, we run cold water of room temperature, $25\,^{0}C$ through the channels, and obtain the cooling curve of the 10 points over another minute of experiment. We find out that the cooling settling time, around 20 seconds, is faster than the heating, which is because convection is also a heat loss process that speeds up cooling rate.

TableAI-5.   cooling temperature of the top surface of the PMMA

time(s)	N1	N2	N3	N...	N10	Temperature difference (Tmax-Tmin)
0	57.1528	60.2706	60.3407	...	57.1669	3.1879
3	45.7137	47.3444	47.8114	...	45.8295	2.0977
6	36.3208	37.8649	37.7748	...	36.3289	1.5441
9	30.9353	31.8243	31.7655	...	30.9139	0.9104
12	28.0927	28.5793	28.5542	...	28.074	0.5053
15	26.6107	26.874	26.8648	...	26.5985	0.2755
18	25.8391	25.9808	25.978	...	25.8318	0.149
21	25.4373	25.5132	25.5129	...	25.4331	0.0801
24	25.228	25.2685	25.2689	...	25.2256	0.0433
27	25.1189	25.1405	25.141	...	25.1176	0.0234
30	25.062	25.0735	25.0739	...	25.0613	0.0126
33	25.0324	25.0384	25.0387	...	25.032	0.0067
36	25.0169	25.0201	25.0203	...	25.0167	0.0036
39	25.0088	25.0105	25.0106	...	25.0087	0.0019
42	25.0046	25.0055	25.0056	...	25.0045	0.0011
45	25.0024	25.0029	25.0029	...	25.0024	0.0005
48	25.0013	25.0015	25.0015	...	25.0012	0.0003
51	25.0007	25.0008	25.0008	...	25.0006	0.0002
54	25.0003	25.0004	25.0004	...	25.0003	1E-04
57	25.0002	25.0002	25.0002	...	25.0002	0
60	25.0001	25.0001	25.0001	...	25.0001	0
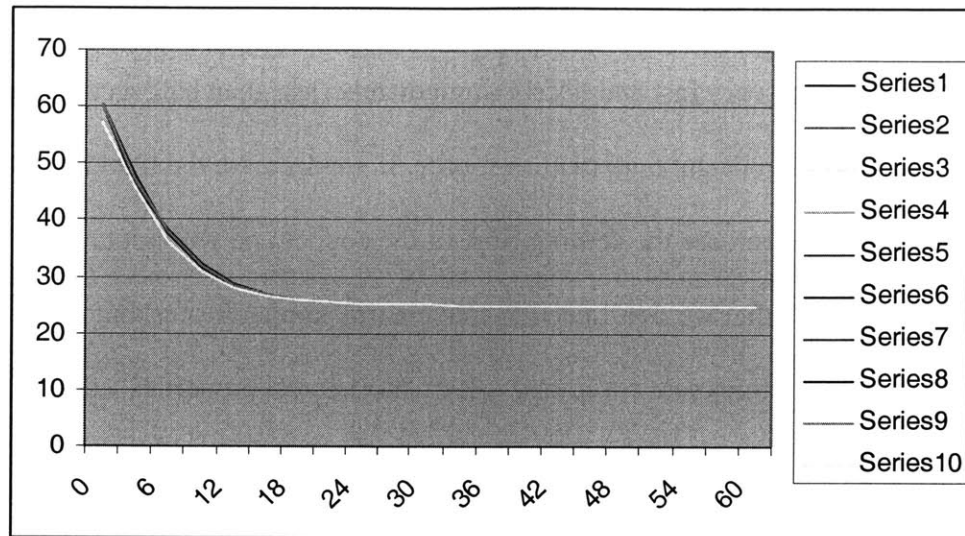
Fig11. Cooling curve

AI-4.3.3   Structure Finite Element Analysis of Copper & PMMA

Current working pressure (45Mpa) is applied to the top of the PMMA piece. We assume that the mechanical character of PMMA don't change with temperature, and always acts as a solid. The boundary condition is that the bottom surface of the copper platen is fixed. By doing simulation, we obtain the displacement result shown in FigAI-12. The maximum displacement is 33 micro meters, which happens on the PMMA piece in the 'X' direction. The maximum vertical displacement (main displacement, 'Y' direction) of the copper heater is around 7 micro meters, which is negligible compared to the thickness of the copper paten. However, the PMMA is not solid at these temperatures, and hence the PMMA will deform more while the copper will deform less, which is good for the set up. FigAI-13 shows the normal vertical stress (where the maximum stress happens,'Y' direction). The maximum stress is 0.175×10^9 Pa, and it is smaller than the yield strength of copper 0.96×10^9 Pa. These analyses are based on the 4mm copper, but since we will choose a thicker copper piece, it won't change the conclusion that the structure of the copper heater is very safe.
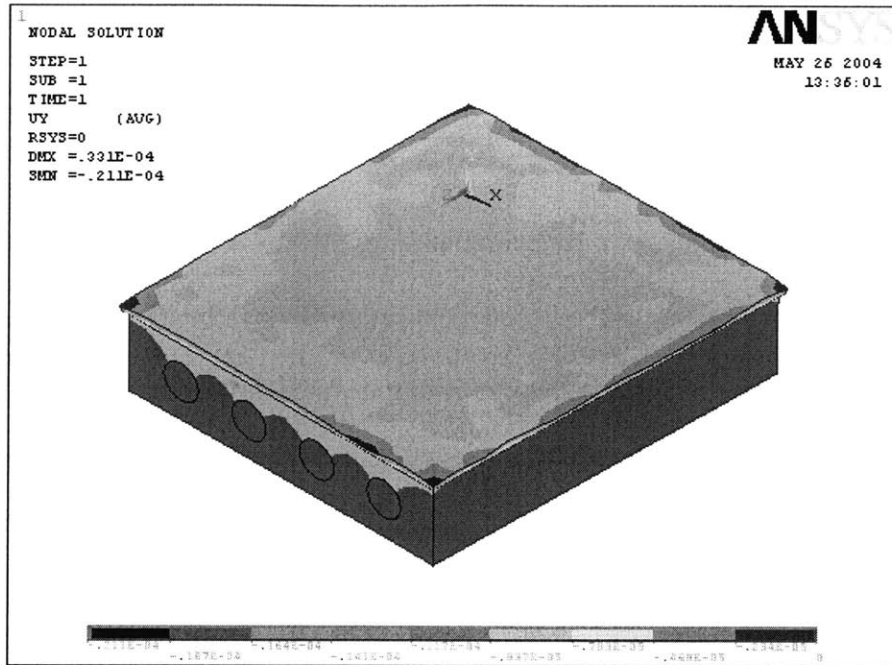
FigAI-12.　Displacement of heater and PMMA
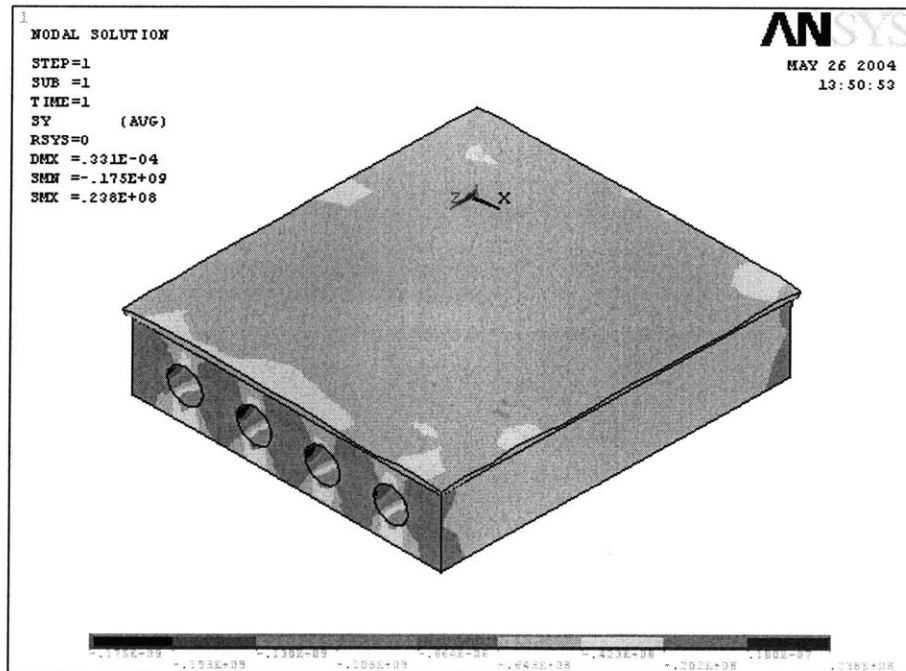
FigAI-13.　Normal vertical stress

AI-5. Actual experiments

AI-5.1   Experiment set up

In order to test the reliability of the simulation of the new virtual set up, we also did some actual experiments. FigAI-14 shows the experiment set up. Two orange buckets contain the hot water and cold water separately. Two valves control the water flow and are connected by a 'T' tube to the working part. The working part is made up of a copper piece and a 'peek' high temperature resistant polymer block. The copper piece is inserted and glued in the peek block. The 'peek' block works as a buffer and a manifold. The valve (hot valve) that connected directly to the hot water bucket is opened so that the hot water run through the peek buffer and the channels in the copper piece, therefore the copper is heated. An infrared camera is used to record the transient temperature change of the top surface of the object.
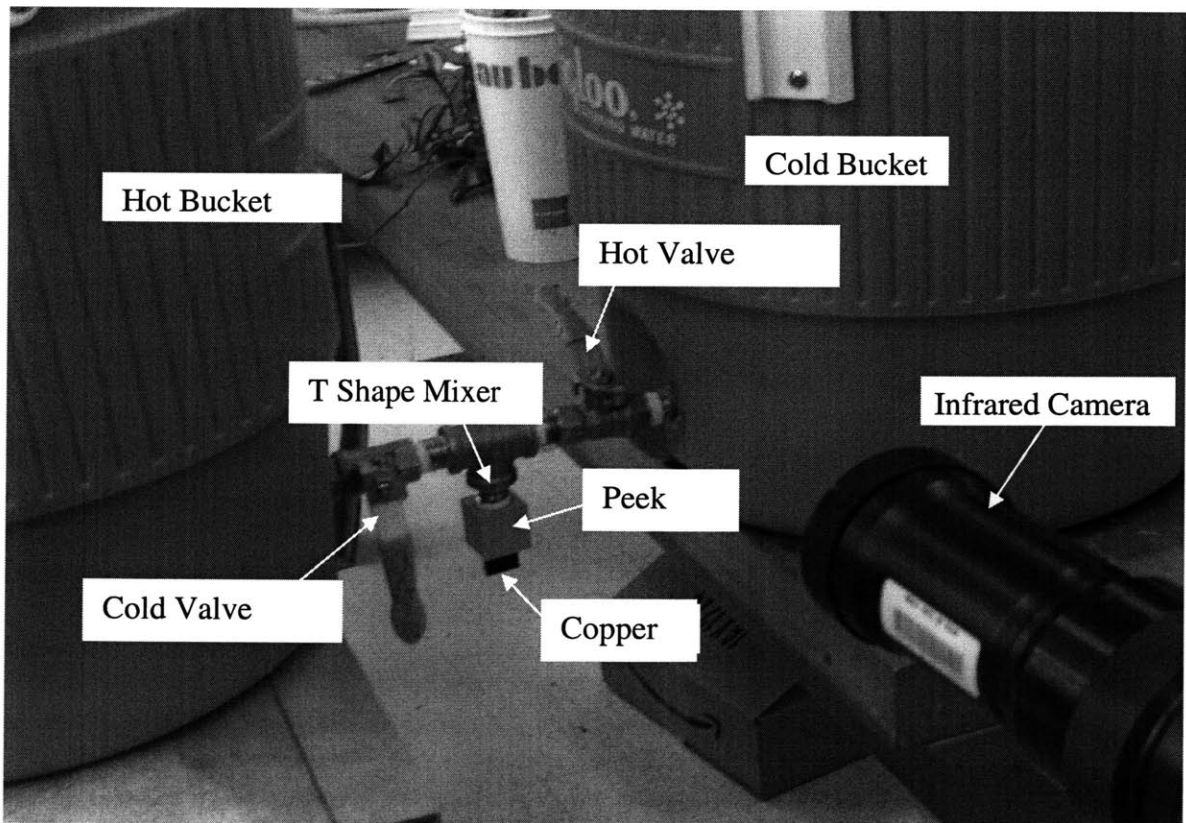
FigAI-14.   Actual experiment set up

AI-5.2   Copper heat transfer experiment

A black tape is attached to the surface of the copper platen because of the high emissivity

of the copper surface so that the transient heat transfer process can be recorded by an infrared

camera. We turn on the hot valve, and hence the copper is heated, and after the copper has

reached a steady state, the cold valve is turned on and at the same time the hot valve is turned off.

The hot water temperature is $65\,^0C$; the cold water temperature is $25\,^0C$. We set the infrared

camera temperature range to be $50\,^0C$. 20 color bands represented the $50\,^0C$, so the temperature

resolution of the video is 2.5 degrees. We estimate the settling time to be the time when the

whole top surface turns to the highest temperature color. TableAI-5 shows the estimations of the

10 settling times of ten heating experiments.

TableAI-6. Settling time of heating copper platen

Run Number	1	2	3	4	5	6	7	8	9	10
Settling Time	3	4	3	4	4	4	4	4	3	4
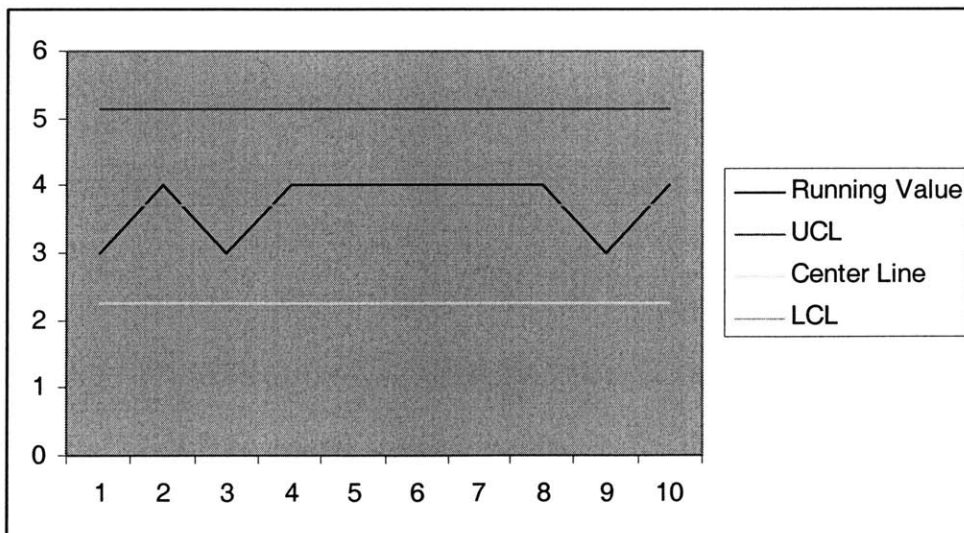
FigAI-15.   Control chart of the copper settling time

FigAI-15 shows that the 10 runs of the copper heat transfer processes are in control. This

means the settling time is around 3.7 seconds. This settling time is longer than that obtained in

the simulation. The reasons for this might come from:

- heat loss due to the brass pipes connection;

- the convection coefficient calculation is not so accurate;

- each time the heating cycle started from the end of the cooling cycle (except the first run), which led to a lower temperature input (the hot water mixes with the cold water that remained in the cooling pipe).

In order to see how these factors affect the result, the following experiments are done: Uninstall the heat transfer system (the Peek and copper), heat the connection brass pipes until it reaches the steady state. Transient temperature of the 'T connection' is taped. Reassemble the heat transfer system as soon as possible, and then turn on the hot valve. Transient temperature of the copper surface is also taped. 10 such experiments are done, and the results are obtained as shown in tableau-7:

Table7. Settling Time of heating "T" and copper platen

Running Number	1	2	3	4	5	6	7	8	9	10
Settling Time of "T" (s)	3	3	3	3	3	3	3	4	4	4
Settling Time of Copper(s)	2	1	2	2	2	3	2	3	3	3
Time difference in between (s)	5	4	4	4	4	5	6	5	5	4
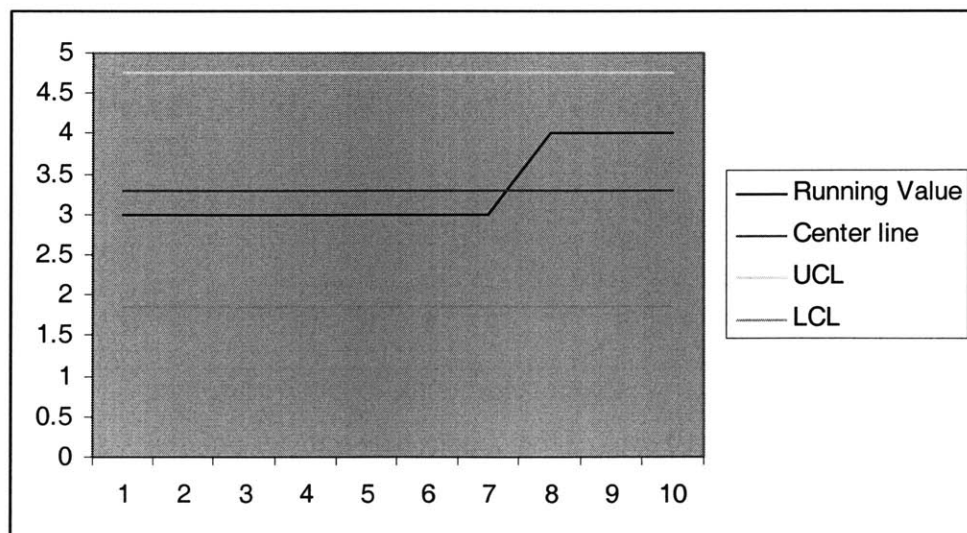
FigAI-16.   Control chart of the "T" settling time
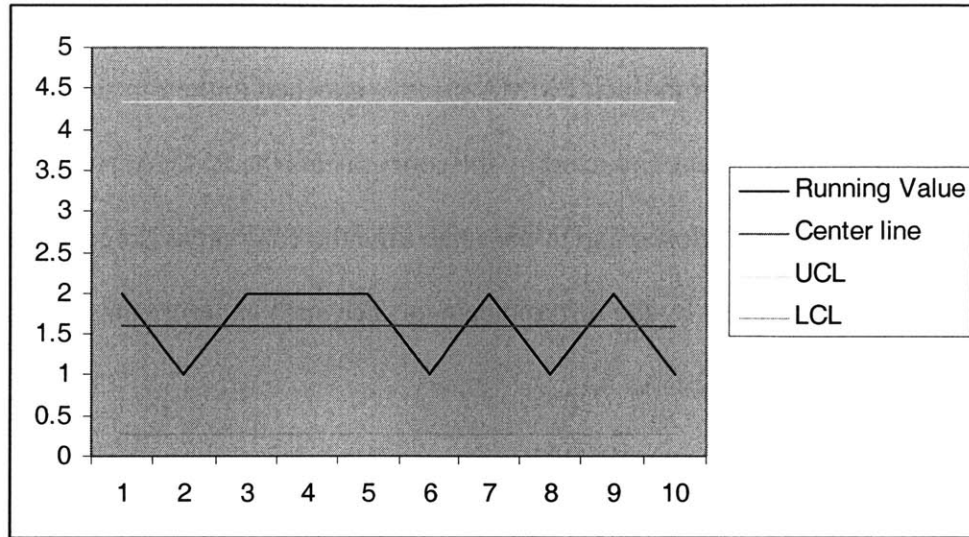
FigAI-17.   Control chart of the copper settling time

FigAI-16 and AI-17 both show that the heating experiments are all in control. Since 4-5 seconds are needed to install the 'Peek' and 'Copper' again, some heat of the 'T' connection is lost during that time through conduction and convection, which make the settling time of the new experiments is not exactly the subtraction of the settling time of the copper in the old experiments and the settling time of the 'T' section, but there is still comparatively large settling time difference, and the time constant is much closer to that of the simulation. In this heat transfer system, the 'T' connection was the dominant heat resistance, so, the settling time was determined by that of the 'T' connection.

No obvious vertical 'temperature band' that are parallel to the channels is detected from the camera video, which means that the temperature uniformity across the surface is good within the resolution of the video. Same thing happens to the simulation transient movie. If we have a proper software to analyze the video, it would help a lot to obtain more precise results.

AI-5.3   Copper +PMMA heat transfer experiment

In this experiment, a 1 mm thick PMMA piece is attached to the top surface of the copper. As the copper is heated, the heat conducted by the copper heats the PMMA. At the end of the heating cycle, the hot valve is closed and at the same time the cold valve is opened. The transient temperature change is recorded by the infrared camera. Ten such experiments are conducted, and the settling time is shown in TableAI-8.

TableAI-8.   Settling time of heating PMMA

Running Number	1	2	3	4	5	6	7	8	9	10
Settling Time of "T" (s)	22	23	25	23	24	25	27	23	22	27
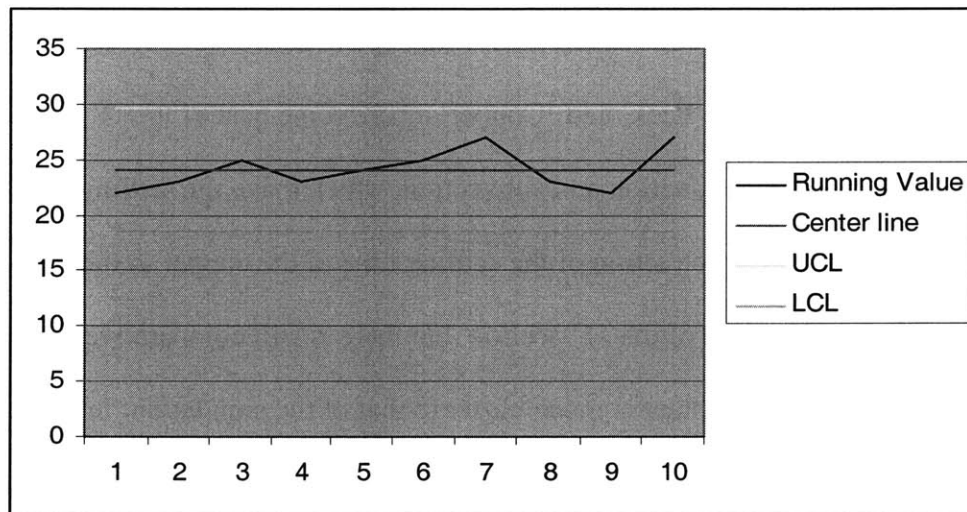
FigAI-18.   Control chart of the PMMA settling time

FigAI-18 shows that the heating of PMMA is in control. The average settling time is around 24 seconds, which is a bit higher than that obtained in the simulation, 22 seconds. As for the uniformity, it is the same as that of the heating of the copper, uniform temperature distribution is obtained.

AI-6. Optimization of system parameters using FEA

In section AI-4 and AI-5, we set up an initial heat transfer system, and prove that proper FEA model is able to provide a good approximation of the reality. In this section, based on the initial design, we would like to vary the thickness of the copper, the location of the channels and the temperature changing path of the heating fluid, and more FEA simulations will be done in order to get better system output: smaller settling time and better temperature uniformity. The objective embossing material used is PMMA and the set up and mechanical properties remained the same as stated in section AI-4.

AI-6.1 Varying the thickness of copper platen

We may be able to obtain different settling time and temperature uniformity by varying the thickness of the copper platen. It is not practical to decrease the thickness of the copper piece with the dimensions of the channels unchanged and the locations remain in the center plane of the copper piece, we only increase the thickness of copper piece to 6mm, 8mm and 10mm. The simulations are done and temperature step response and temperature uniformities are obtained, shown in FigAI-19, TableAI-9 and FigAI-20. From FigAI-19, not much difference of the heating or cooling settling time is detected for the four different occasions. From tableAI-9 and FigAI-20 we find that the temperature difference is the largest for the '4mm' system at the beginning of the heating cycle, but it decreases faster than any other systems, and becomes smallest when the system reaches the steady state. However, this difference is on the order of millidegrees. The same thing happens to the cooling cycle.
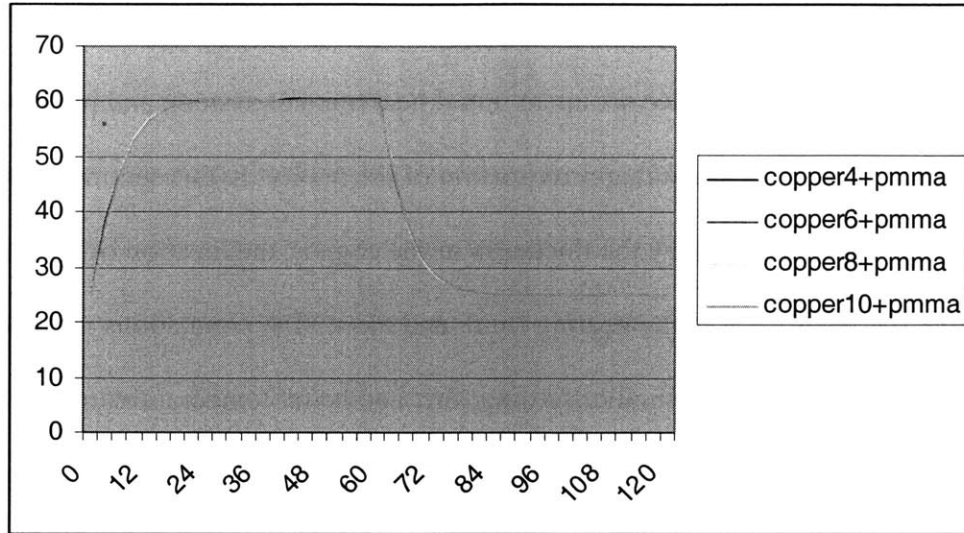
FigAI-19.　Step temperature responses

TableAI-9. Temperature difference (Tmax-Tmin)

time(s)	Temperature Difference(^0C)			
	copper4+PMMA	copper6+PMMA	copper8+PMMA	copper10+PMMA
0	0	0	0	0
3	2.063	1.5479	2.0436	1.8124
6	0.7151	0.5463	0.6627	0.5748
9	0.4943	0.361	0.4891	0.434
12	0.2635	0.1886	0.2625	0.2327
15	0.1354	0.0951	0.1348	0.1186
18	0.0728	0.0736	0.0741	0.071
21	0.0704	0.0734	0.0715	0.0672
24	0.0697	0.0754	0.0706	0.068
27	0.0696	0.0769	0.0711	0.07
30	0.0719	0.078	0.0736	0.0719
33	0.0732	0.0787	0.0752	0.073
36	0.074	0.079	0.0763	0.0741
39	0.0746	0.0793	0.0769	0.0749
42	0.0749	0.0796	0.0772	0.0753
45	0.0751	0.0796	0.0773	0.0755
48	0.0752	0.0797	0.0774	0.0757
51	0.0753	0.0797	0.0775	0.0758
54	0.0753	0.0797	0.0776	0.0758
57	0.0753	0.0797	0.0776	0.0758
60	0.0753	0.0797	0.0776	0.0759
63	2.0578	1.5425	2.0369	1.8053
66	0.7203	0.5524	0.6667	0.5998
69	0.4995	0.3767	0.4946	0.4471
72	0.2687	0.2155	0.2691	0.2511
75	0.1407	0.1204	0.1415	0.1374
78	0.0738	0.0671	0.0744	0.0752
81	0.0387	0.0373	0.0391	0.0412

84	0.0208	0.0208	0.0209	0.0226
87	0.0113	0.0115	0.0114	0.0124
90	0.0061	0.0063	0.0062	0.0069
93	0.0034	0.0035	0.0033	0.0037
96	0.0018	0.0019	0.0018	0.002
99	0.001	0.001	0.001	0.0011
102	0.0005	0.0006	0.0006	0.0006
105	0.0003	0.0003	0.0003	0.0003
108	0.0002	0.0002	0.0002	1E-04
111	1E-04	1E-04	1E-04	1E-04
114	1E-04	1E-04	1E-04	1E-04
117	0	0	0	1E-04
120	0	0	0	0
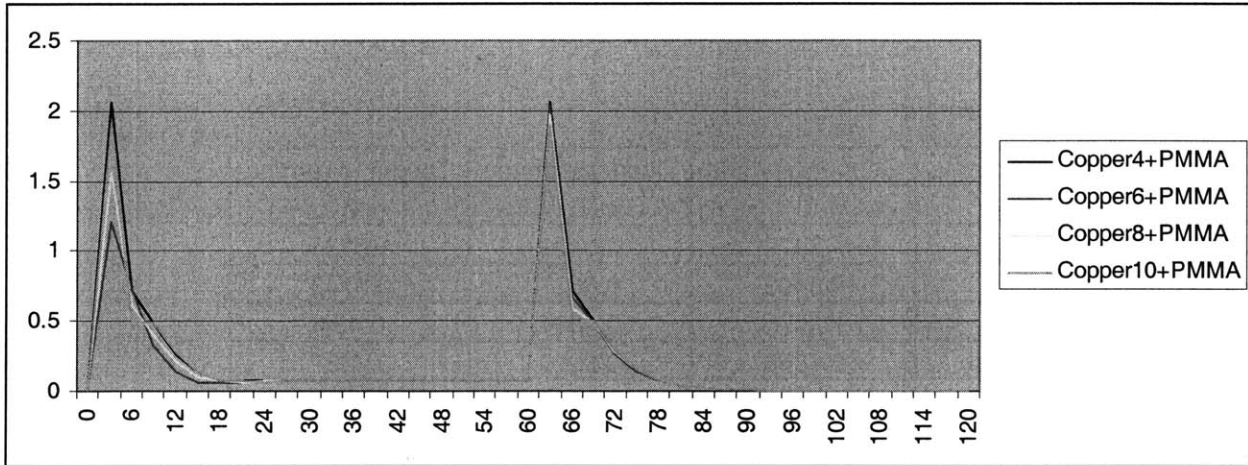
FigAI-20. Temperature gap

AI-6.2 Varying the location of fluidic channels

Now we would like to see if varying the locations of the fluidic channels will influence the settling time and the temperature uniformity, so the locations of the fluidic channels of 6mm, 8mm and 10mm copper are moved downwards until the axis of the channels are just 2mm above the bottom surface of the copper platen. We obtain the temperature response and uniformity picture shown in FigAI-21, TableAI-10 and FigAI-22.
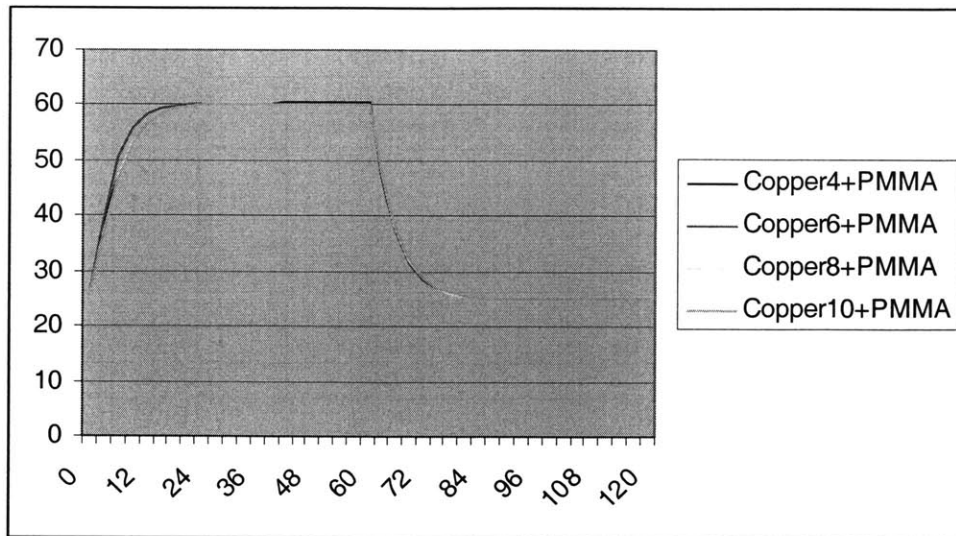
FigAI-21.   Temperature response

TableAI-10. Temperature gap

Time	Copper4+pmma	Copper6+pmma	Copper8+pmma	Copper10+pmma
0	0	0	0	0
3	2.063	1.5479	2.0436	1.8124
6	0.7151	0.5463	0.6627	0.5748
9	0.4943	0.361	0.4891	0.434
12	0.2635	0.1886	0.2625	0.2327
15	0.1354	0.0951	0.1348	0.1186
18	0.0728	0.0736	0.0741	0.071
21	0.0704	0.0734	0.0715	0.0672
24	0.0697	0.0754	0.0706	0.068
27	0.0696	0.0769	0.0711	0.07
30	0.0719	0.078	0.0736	0.0719
33	0.0732	0.0787	0.0752	0.073
36	0.074	0.079	0.0763	0.0741
39	0.0746	0.0793	0.0769	0.0749
42	0.0749	0.0796	0.0772	0.0753
45	0.0751	0.0796	0.0773	0.0755
48	0.0752	0.0797	0.0774	0.0757
51	0.0753	0.0797	0.0775	0.0758
54	0.0753	0.0797	0.0776	0.0758
57	0.0753	0.0797	0.0776	0.0758
60	0.0753	0.0797	0.0776	0.0759
63	2.0578	1.5425	2.0369	1.8053
66	0.7203	0.5524	0.6667	0.5998
69	0.4995	0.3767	0.4946	0.4471
72	0.2687	0.2155	0.2691	0.2511
75	0.1407	0.1204	0.1415	0.1374
78	0.0738	0.0671	0.0744	0.0752

81	0.0387	0.0373	0.0391	0.0412
84	0.0208	0.0208	0.0209	0.0226
87	0.0113	0.0115	0.0114	0.0124
90	0.0061	0.0063	0.0062	0.0069
93	0.0034	0.0035	0.0033	0.0037
96	0.0018	0.0019	0.0018	0.002
99	0.001	0.001	0.001	0.0011
102	0.0005	0.0006	0.0006	0.0006
105	0.0003	0.0003	0.0003	0.0003
108	0.0002	0.0002	0.0002	1.00E-04
111	1.00E-04	1.00E-04	1.00E-04	1.00E-04
114	1.00E-04	1.00E-04	1.00E-04	1.00E-04
117	0	0	0	1.00E-04
120	0	0	0	0
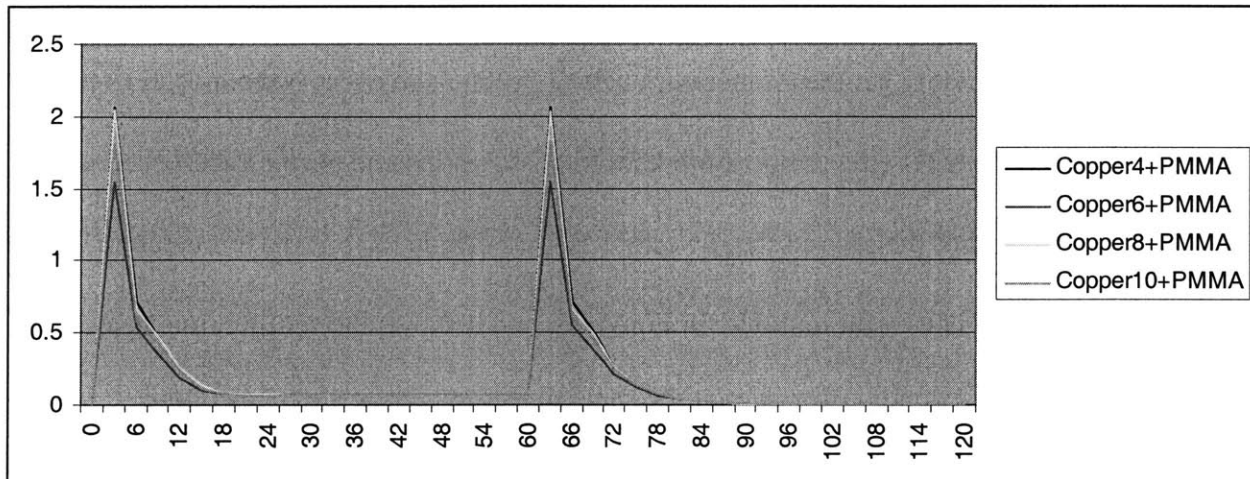
FigAI-22.   Temperature gap

Not much difference of the temperature settling times is observed among these four values. However, the settling times are slightly longer than that of the previous ones. The trend of the temperature difference is also similar to that of the previous simulations.

AI-6.3   Varying of heating path

We could improve the settling time by changing the "heating path", the temperatures of the heating fluids that go through the channels. For example, from the analysis above, we could propose a better heating path so that the PMMA piece could be heated to a certain temperature

that is close to the target temperature by first applying a very high temperature fluid for a short period of time and then lower this fluid temperature to control the PMMA temperature to its desired target value.

For example, we simulate an experiment at $130\ ^{o}C$ (twice $65\ ^{o}C$) and find out the heating time to bring the PMMA to a certain temperature, say, $60 \pm 0.5^{o}C$. Fig23 shows the simulation heating curve. Since the simulation is done in a step size of 3 seconds (we can decrease the step size, but 3 seconds is chosen because we want to save the computer memory and speed the calculation up), we can only get the temperature value of each node every 3 seconds. From the curve, we find approximately the temperature goes to $46\ ^{o}C$ at the end of the first 3 second, and around $74\ ^{o}C$ at the end of the second step 6 second. So, we decide to shift the temperature of the heating fluid to $65\ ^{o}C$. The result is shown in FigAI-23, and it shows the settling time decreases from 22 seconds to 15 seconds. How ever at the same time it increases the temperature difference.
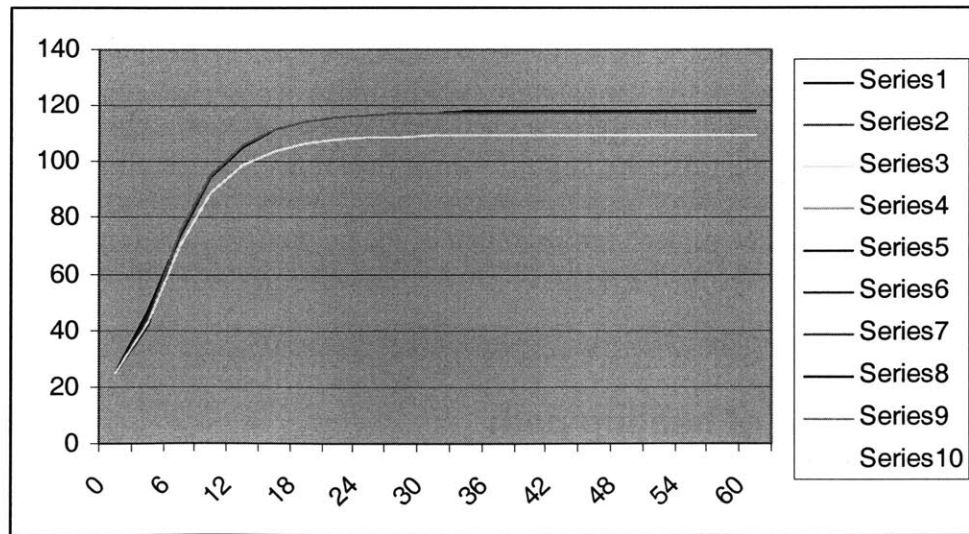
FigAI-23.   Heating curve of copper6+pmma using 130 C heating fluid
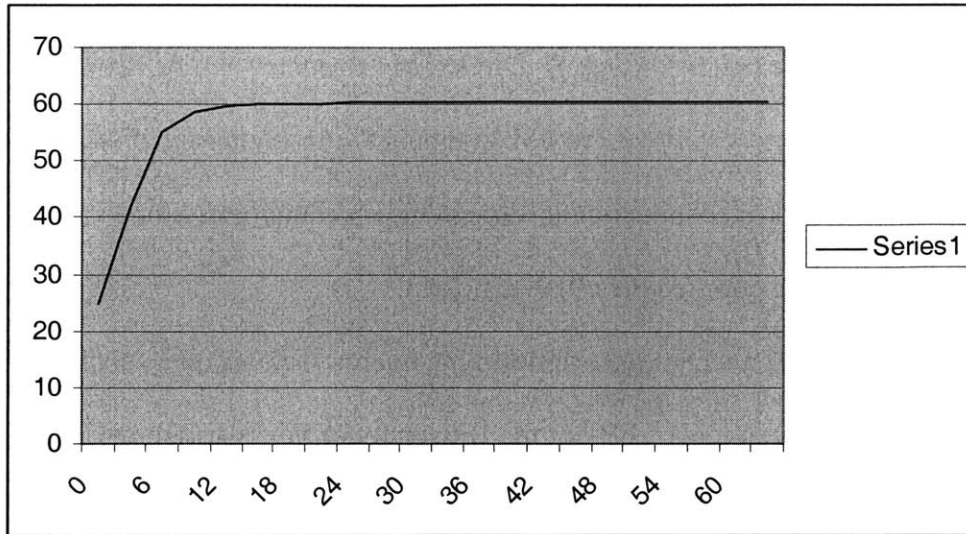
FigAI-24.　Heating curve of 130C and 65C heating fluids

AI-7. Conclusion

1. Statistical analysis of the experiments showed that a proper FEA model could be a good approximation of the real situation. We can change the system parameters comparatively easily and do virtual experiments by using the FEA model.

2. The result of the virtual experiments showed that the '4mm' copper heat transfer system was the optimal design.

Appendix I Reference

[1]   Hardt, D. E., Ganesan, B., Wang, Q, Dirckx, M., Rzepniewski, A. K., "Process Control in

Micro-Embossing: A Review ", Proc. 3rd SMA Annual Symposium Jan, 2004.

[2]   http://www.jo-mikrotechnik.com/noframes/english/equip/hex2.htm

[3]   http://www.rdmag.com/features/0107nano.asp

[4]   "Hot Embossing is a technique of imprinting microstructures on a substrate (polymer)

using a master mold (silicon tool)." PPT of the University of Texas at Arlington

[5]   N. Roos, T. Luxbacher, T. Glinsner, K. Pfeiffer, H. Schulz, and H.C.Scheer,

"Nanoimprint lithography with a commercial 4 inch bond system for hot embossing", presented

at SPIE's 26th Annual International Symposium Microlithography, Feb. 25-March 2, 2001

[6]   Stephen Y. Chou, Peter R. Krauss, and Preston J. Renstrom, "Imprint of sub-25 nm vias

and trenches in polymers", Applied Physics Letter, Vol.67, no. 21, 20 November 1995, pp. 3114-

3116.

[7]   Lingjie Guo, Peter R. Krauss, and Stephen Y. Chou, "Nanoscale silicon field effect

transistors fabricated using imprint lithography", Applied Physics Letter, Vol. 71, no. 13, 29

September 1997, pp. 1881-1883

[8]   Jagannathan Narasimhan and Ian Papautsky, "Polymer embossing tools for rapid

prototyping of plastic microfluidic devices", Journal of Micromechanics and Microengineering,

Vol. 14, 2004, pp. 96-103

[9]   Chin Lung Chen and Fuhua Jen. Fabrication of Polymer Splitter by Micro Hot

Embossing Technique

Appendix II

Literature Review on the High Viscous Fluid Flow in Micro Embossing Process

AII-1. Abstract

Micro embossing process is a single-step polymer deformation process, which involves the flow of the polymer into the recessive area of the embossing die. Good understanding of the flow pattern can help choosing proper manufacturing machine and material parameters so as to improve the micro embossing productivity and quality. This report reviews the current research on the theoretical and experimental study of polymer flow in micro embossing process. Researchers agree that the increasing of embossing temperature, embossing pressure and film thickness results in shorter embossing time, better material filling and surface finishing. However, there are some conflicts in either the diversity of the experiments consequence or the explanation of the similar phenomena observed. There is still no effective theoretical estimation of the productivity and quality, and no systematic quality evaluation criteria or scientific research on the improvement of the final parts either.

AII-2. Introduction

With the development of biomedical, energy, and optical industries, large scale manufacturing of high quality, low cost and disposable micro fluidic and optical devices is in need. A single step polymer deformation micro embossing process is getting much research attention to fulfill the market needs.

Micro embossing process involves a one step process: the thermoplastic polymer, normally polymethylmethacrylate (PMMA) is chosen because of its chemistry stabilities and good photonic properties, and the embossing patterned silicon master tool are heated up above the glass transition temperature T_g . After that a controlled force or pressure is

applied to the tool, and it moves toward the PMMA with a certain embossing velocity. During this time, the low Raynold's number polymer fluid flows under the pressure and fulfills the cavities of the die until the viscous polymer has the opposing shape of the features on the die. With the force or pressure maintained, the polymer and the die are cooled down below glass transition temperature of the polymer, and the polymer is pulled apart from the die. The cooling cycle continues (often with a different cooling rate as the one before the polymer is separated from the die) until the polymer reaches the ambient temperature.

The process cycle can be represented as in Fig. AII-1 (time not strictly to scale). The factors that determine the micro hot embossing efficiency, which is directly related to the process cost, often include preparing time, heating and cooling time, and embossing time. Currently researchers are doing investigation of the selection of the thermal transfer scheme in order to minimize the heating and cooling times, which occupy a major part of the cycling time. TableAII-1 shows the heating and cooling times of the present embossing machines.

TableAII-1. Thermal specification of existing machines

	Heating Time (min)	Cooling Time (min)
Jenoptik HX Serials	7	7
EV Group EV520HE	6	5
Arlington bioMEMS group	3	2
Our group (current set up)	15	5
Our group target set up	**1**	**1**

T embossing

T demolding

T ambient

Preparing time | Heating time | Embossing time | Cooling time I | Cooling time II
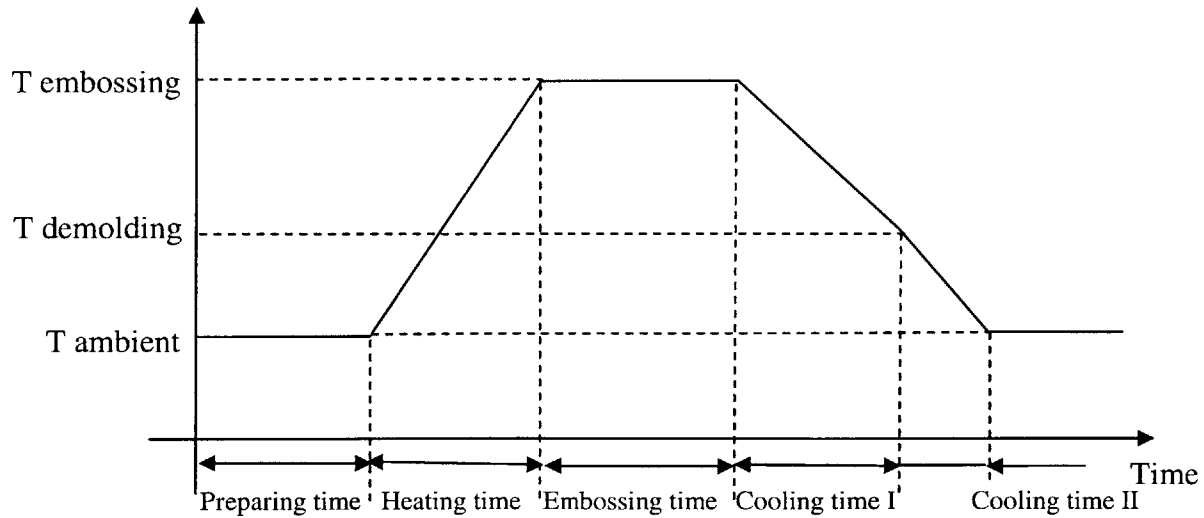
Time

Figure AII-1.   Micro hot embossing process cycle

As the heating and cooling times are decreasing, the proportion of embossing time in this cycle is increasing if the embossing time remains unchanged. Thus, a better time estimation of the embossing time is required.

The quality of the embossed part, which are represented as the dimension accuracy, variation and surface flatness, is determined by the embossing pressure, temperature, time and velocity scheme and etc. All the determining factors are affecting the final quality by affecting the polymer fluid flow pattern. Therefore, better understanding of the polymer fluid flow physics that shape the final product is imperative for both better estimation of the cycle time and final product quality.

In this report I would like to summarize the polymer flow research in micro/nano embossing done by other researchers. I will introduce the work done by others one by one first and then give out my thought toward them.

AII-3. Current research

AII-3.1　Heyderman

Heyderman[1] investigated the PMMA fluid filling into the cavities of a die

during the micro embossing process by varying the polymer molecular weight, polymer

film thickness, embossing temperature, embossing time, and cooling time. A series of

embossing time that is short enough is chosen so that the polymer will be hardened and

de-embossed from the die when the cavity is only partially filled. By doing this, the

filling path of the PMMA fluid is recorded. The experiments show the polymer in the

center of the cavity region is pushed by the moving polymer from the borders in the very

first embossing stage. This causes a compression of the central region, and thus results in

a convex profile. Because of the polymer thinning effect, the viscosity of the PMMA

flow that is close to the cavity wall decreases, and hence the fluid climbs up the wall

faster than the central region. Besides this, the surface tension also helps to pull the

polymer up along the wall. Therefore, between the central region and the region close to

the wall, there is a material dip.

In Heyderman's paper [1], the optimal embossing temperature was $290\,^{0}C$ with

an embossing time of 2 minutes. But in the real application, it was reduced to $270\,^{0}C$ with

the embossing time increased to 10 minutes to avoid the polymer degradation at

$290\,^{0}C$ and at the same time to guarantee the fulfilling of the polymer into the cavities.

Beside the experimental results, Heyderman and his coworkers also found

theoretical equation that expressed the relations among the embossing pressure,

embossing time, polymer viscosity and geometry dimensions by applying a simple two-

dimensional squeeze flow theory. Their equation of the filling time of the polymer into

the cavities is:

$$t_f = \frac{\eta_0 S^2}{2p}(\frac{1}{h_f^2} - \frac{1}{h_0^2})$$ (AII-1)

where η_0 is the polymer viscosity; p is the embossing pressure; h_f and h_0 are the final

and initial height of the polymer film respectively; S is the die width. Assume W and D

are the width and depth of the cavity, then there exists the mass conservation relation

$h_f = h_0 - WD/S$. Equation (AII-1) was obtained based on the purely viscous

incompressible liquid and non slip boundary condition assumptions. It shows that the

filling time is proportional to the viscosity of the fluid and is inversely proportional to the

embossing pressure. In order to decrease the filling time, we would better increase the

PMMA film thickness or decrease the ratio of cavity volume to die width.

Heyderman's experiments show that when the PMMA viscosity is in the range

300 to 3000Pa.s the polymer fills the cavities most completely. In order to control the

viscosity, Williams-Landel-Ferry (WLF) equation is applied:

$$\log a_T = -\frac{C_1(T - T_0)}{C_2 + T - T_0} = \log\frac{\eta}{\eta_{T_0}}$$ (AII-2)

where C_1 and C_2 are constants for a specific polymer. From WLF equation, we see that

temperature is ideally (no polymer thinning or thickening) the only factors that

determines the polymer viscosity.

AII-3.2   Schift

In Heyderman's colleague Schift's another paper [2], he reported that both

capillary effects and the compressive effects guide the polymer fluid flow in the self-

assembled patterns. Electrostatic fields were applied between the die and the PMMA film,

and under this field, the polymer mounds were deformed and the velocity of polymer

flow into the cavities is speeded up. They also talked about the viscous fingering, but

since they did not do the experiments in the vacuum circumstance, it is not clear if the

fingering is a result of trapped air or the combination effect of trapped air and trapped

moisture.

There is no much theoretical information in paper [2], but by investigating the

experiments they pointed out that different embossing parameters, stamp geometries and

polymers characters are the factors that affect the final formation. A study including a

theoretical determination of the pattern period is imperative.

AII-3.3   Chukalina

Chukalina [3] studied a simple case: a round flat stamp of radius R moves with

velocity u into a resist layer of thickness h and viscosity η. She estimated the printing

force based on the Raynold's equations (no induction process):

$$F_R = 3\pi\eta u R^4 / 2h^3 \tag{AII-3}$$

From the equation above, we could see that the way to lower the embossing force is to

lower the volume flow rate: $\pi R^2 u$. In order to reduce the embossing time, we should

inverse proportionally increase the embossing force.

Same as Heyderman, Chukalina [3] divided the embossing process into two stages: first is the short distance mass transfer, which is a filling procedure into the cavities. The second stage involves large distance mass transfer through narrow channels. The first stage determines the embossing time and hence analysis of the first stage is important to estimate the duration of the stage. Set the Z coordinate axis along the depth of the cavity and the perpendicular X coordinate axis along the width of the cavity. The stabilized flow is characterized by

$$V_x = 4(\frac{h}{L})(1 - \frac{z}{h})(\frac{z}{h}) = 4\frac{z}{L}(1 - \frac{z}{h}) \qquad \text{(AII-4)}$$

$$V_z = 0 \qquad \text{(AII-5)}$$

in total correspondence to Raynold's solution. Equation (AII-4) shows that the velocity of the flow front is parabolic. Equation (AII-5) also implies that there is no mass transfer along the X direction.

Chukalina [3] also did some research of the impact of chain size on the mass transferring capability at nano scale. The relation between the polymer particles' radius L and polymer length N is

$$L = L_0 N^{\frac{1}{2}} \qquad \text{(AII-6)}$$

For a polymer with molecular weight 100, the particle radius is around 20-100nm. This is comparable with resist thickness and embossing structure details. So, in this situation, the viscosity is now dependent on the distance between the polymer molecule and the walls.

In paper [3], Chukalina did research on the viscosity near wall by using probability theories. $W(z)$ is the probability for a polymer molecular chain to avoid the wall. This chain starts at a location of distance 'z' from the wall. The viscosity of it at this

location is, $\eta(z) = \eta_b / W(z)$, where η_b is the isotropic bulk viscosity. Mathematical model for $W(z)$ calculation is non-stationary diffusion equation with absorption on the boundary. It gives for small h / L

$$W(z) = \sin(\pi \frac{z}{h}) \exp[-(\pi \frac{L}{h})^2]$$ (AII-7)

And hence the printing force is

$$F(p) = \frac{1}{2} \pi \eta u R^4 \exp[(\pi \frac{L}{h})^2]$$ (AII-8)

Now this force is a little bit different with that obtained in equation (AII-3), where the printing force increases at power $\frac{1}{h^3}$. Chukalina gave out these results, but she didn't have experiments that can support her equations, and the deduction of them was not presented in paper [3] either.

AII-3.4   Scheer I

Scheer [4] carried out experiments with different hot embossing conditions:

1.   Three different embossing systems: hydraulic press system, motor-driven atomized press system and commercial EV520 HE hot embossing system

2.   Two different dies: the first one is silicon die with pyramid arrays in an area of $2 \times 2cm^2$. This is used to investigate the filling of recessed patterned fields and the replication of three-dimensional structures. The features' dimension varies from 400nm to $100\,\mu m$. The other die is a 4 inch wafer die. There is large unpatterned recessed area between the elevated features, so this die is mainly used for investigation of the flow of material with large unpatterned recessed areas.

3. Different polymers: PMMA with mean molecular weight of 350k. The glass

transition temperature of it is $T_g = 105^0 C$. Plex 6792 and mr-i-8030,

$T_g = 115^0 C$. The authors did not present much about the differences in the

flow properties of the polymers. They picked these polymers just because of

the variance of dry etching stabilities of them.

4. Polymer film thickness varies from 500nm to 4 μm.

5. Embossing temperature $T = T_g + 90^0 C$, embossing pressure 100bar.

Scheer also pointed out that

1. Different spring back of the polymer happened at the elevated die region.

2. The shrinkage of edges of features was bigger than that of the center part. This

resulted in a bow shape in the centre of the feature.

3. Higher pressure will cause shear thinning effect at the wall and it will help the

polymer fluid flows faster.

However, this paper did not talk much about the elastic recovery but the polymer

flow during the embossing. The flow was characterized by the viscosity parameters, so

first of all, they applied WLF equation and Vogel-Fulcher law. They found that at about

$100^0 C$ above T_g, a temperature change ΔT of $10^0 C$ resulted in a change of viscosity or

response time of one order of magnitude. The viscosity of all polymers have approximate

the same order of magnitude, which is around 10^{12} Pa s at T_g, and about 10 Pa s at about

$100^0 C$ above T_g. The zero shear viscosity η for PMMA is in the range of 300-70000 Pa

s in the embossing temperature range.

The polymer during embossing process is regarded as a non-compressible Newtonian liquid, which is characterized by its zero shear viscosity η at a selected processing temperature with this assumption, the relation between the effective pressure p_{eff}, the actual polymer height $h(t)$, the stamp radius R and the vertical imprint velocity $v(t)$ can be derived from hydrodynamic theory. Assuming a simple cylindrical polymer block and an unpatterned stamp are used, the relation among the parameters are shown below:

$$v(t) \approx (p_{eff} h(t)^3)/(\eta R^2) \tag{AII-9}$$

which only has discrepancy in coefficient with what Chukalina obtained. In the equation above, Scheer stressed the concept of 'effective pressure'. The effective pressure is different during filling process and maintaining force stages. The effective pressure is much higher for the elevated dies than the recessive masters. So, after the filling process ends, and if we use the same external embossing force, the embossing velocity will drop dramatically for the elevated masters.

The results for the recessed patterned dies show that for an unfulfilled polymer part, the cavities at the periphery are better filled than those in the center. In the same embossing conditions, the thicker the polymer film on the substrate is the better filling for the cavities in the center is. This corresponds to equation (AII-9) well, which shows that larger polymer film thickness will lead to larger polymer flow velocity, and hence the smaller filling time will be obtained.

The results of the experiments with large recessed un-patterned areas (regions between elevated stamp features) show that as the die is penetrating into the film a polymer front starts to move away from the edge of each elevated features. This causes a

flower-like propagating rim around the embossed feature in the film. In addition to that, they obtained examples for a superimposed spot-like or mound-like filling, developing from the horizontal polymer surface. As the thickness of the polymer film increases, all the flower-like, spot-like and the mound-like type of filling will be less pronounced.

AII-3.5   Scheer II

Scheer started to evaluate hot embossing lithography at the wafer scale level based on the phenomena observed and stated in paper [4]. First of all, in order to avoid the mounds and stretches the polymer thickness can be increased. Secondly, the increase of embossing time is quite useful but slows down the process. Thirdly, temperature increase is more efficient than time increase because of the logarithmic viscosity dependency between characteristic reaction times and respective temperature of a polymer. But when temperature is raised beyond a level of $100^{0}C$ above T_g, the effect is decreasing. Besides this, the polymer may start to decompose and thus may change its dry etch stability, and the temperature induced stresses may complicate wafer scale processing. Finally, the pressure increase is efficient too and is easily done. Besides these, the wafer scale embossing requires that the wafer should be very flat.

AII-3.6   Schulz

Thickness and uniformity of the residual layer are major global quality criteria for nanoimprint lithography. They carried out several experiments with 2x2 cm silicon stamp covered with an anti-adhesive layer of perfluorooctyl trichlorosilane. It is fully patterned with feature sizes from 400nm up to $100\,\mu m$, about 510nm with variant pattern density. The film thicknesses of polymer polystyrene (PS, $T_g =112^{0}C$) are 140, 275 and 560 nm,

which correspond to the 50%, 100% and 200% filling of the PS supply of stamp cavities. The films are spin coated to the substrates and rest under ambience for 12 hours. This is followed by a 30 minutes anneal at $150\,^{0}C$ under vacuum, and later it is cooled down from 150 to 70 ^{0}C within 3 hours to ensure the polymer relaxation. The embossing temperature is $200\,^{0}C$, embossing pressure is 100bar, and the embossing time is 3 minutes.

Schulz demonstrated that the height and uniformity of the residual layer strongly depend on the specific stamp layout which has to be considered for correct choice of the initial polymer layer thickness. A 100% polymer filling into the cavities is favorable, while an over filling should be avoided for optimal residual layer thickness.

AII-3.7　　Ressier

Ressier[7] did some research on the recovery of residual resist occurring directly after the de-embossing stage in the center of micrometric patterns replicated by hot embossing lithography. Their dies were 4x4mm silicone positive mould, which contained several arrays of pillars, ranging from 5 to 100 μm in diameter and 230 nm in depth. The distance between them was in the same order to their diameter. The ratio of elevated to recessed mould areas was about 10%. The polymer used was PMMA, which had a 15kg/mol molecular weight and 98 ^{0}C glass transition temperature. The PMMA film here was 270 nm. The embossing speed was 0.050mm/min, the embossing time was 30 minutes, and the de-embossing speed was 0.5mm/min. The embossing force varied from 300 to 1500N, the embossing temperature varies from 150 to 200 ^{0}C, and the de-embossing temperature was $50\,^{0}C$.

Ressier set the embossing temperature to be 175 ^0C, at which temperature

PMMA had a rubbery behavior, and de-embossing temperature to be $50\,^0C$ when PMMA

is in the glass regime. The results showed that the recoveries of the PMMA happened just

after the de-embossing stages, which was apposing to what were stated in paper [6] that

the recoveries happened after several months. Given the same embossing temperature and

pressure, for the same depth of the patterns, the features with smaller diameter tended to

have less spring back relaxation. For a certain pattern, increasing the pressure and

temperature will help to reduce the recoveries.

AII-3.8   Bickerton [8]

As for the flow modeling approach, we can refer to some injection/compression

moulding theories, as stated in paper [8]. Bickerton divided the injection moulding

process into two phases: polymer flows into the mould cavities and be compressed

thereafter. Assume the cavity is a cylinder, and the filling time of the polymer along the

cylinder height is ignored, so the flow is the radial flow with a constant intersection area.

The governing equation for the fluid pressure is:

$$\frac{1}{r}\frac{d}{dr}(r\frac{dp}{dr}) = \frac{\mu\dot{h}}{Kh}$$

(AII-10)

the boundary conditions during the injection phase are

$$r = r_i \quad p = p_{inj}$$

(AII-11)

$$r = r_f \quad p = 0$$

(AII-12)

where p is the local pressure of the fluid, r is the radius of the flow, r_f is the radius of the flow front, μ is the viscosity of the fluid, h is the cavity thickness, K is the perform permeability tensor.

The equations above reduce to the local pressure:

$$p(r) = p_{inj} \frac{\ln(r/r_f)}{\ln(r_i/r_f)}$$ (AII-13)

Then the force exerted on the mould due to fluid pressure is found to be

$$F_{fluid} = \frac{2\pi p_{inj}}{\ln(r_i/r_f)} (\frac{r_i^2}{2} \ln(\frac{r_f}{r_i}) - \frac{1}{4}(r_f^2 - r_i^2))$$ (AII-14)

whereas during the compression phase the boundary conditions are

$$r = r_i \quad \frac{dp}{dr} \approx 0$$ (AII-15)

$$r = r_f \quad p = 0$$ (AII-16)

these lead to the local pressure and force:

$$p(r) = \frac{\mu \dot{h}}{4Kh} ((r^2 - r_f^2) + 2r_i^2 \ln(r_f/r))$$ (AII-17)

$$F_{fluid} = \frac{\pi \mu \dot{h}}{4Kh} (-\frac{r_f^4}{2} + 2r_i^2 r_f^2 - \frac{3r_i^4}{2} + 2r_i^4 \ln(\frac{r_i}{r_f}))$$ (AII-18)

These equations were used to explore the effect of process design parameters on resulting filling time and clamping force requirements. When we increase the clamping force or increase the internal stress applied to the mould, the filling time could be reduced. Experiments results verified the suitability of the governing flow equations, with good agreement found between experimental and numerically predicted fluid pressure trace. But the predictions of the mould clamping force during the compression phase showed

significant qualitative differences, more work being required to understand time dependent reinforcement deformation behavior. Due to the similar time scales of these deformation phenomena, and the duration of a typical injection moulding filling phase, development of viscoelastic reinforcement deformation models is required to improve modeling of these processes.

3.9 Non Newtonian polymer fluid flow

In all the research papers mentioned above, the polymer fluid flow is assumed to be Newtonian fluid flow, but there is some evidence indicating that polymeric flows in micro channels have non Newtonian characteristics. Yao [9] studied the size-dependent viscosity, wall slip and surface tension on the filling process of polymeric materials into micro channels.

Much previous research shows that the viscosity close to the tens of micrometers channel is 50-80% higher than the bulk viscosity. This increase is believed to be because of either collective molecular motion effects or the immobility of the layer of molecules in contact with the solid surface. The microscale viscosity is:

$$\eta(\dot{\gamma}, T, p) = \phi(z)\eta_b(\dot{\gamma}, T, p) = (1 + \xi \frac{g^2}{D^2})\eta_b(\dot{\gamma}, T, p) \qquad \text{(AII-19)}$$

where η_b is the macroscale bulk viscosity, and $\phi(z)$ is the microscale size correcting factor, and it is obtained based on the Eringen-Okada equation. ξ is a nondimensional constant, g is the gyration radius of fluid molecules, and D is an external characteristic length. So, the wall thickening is playing a role in the polymer flow in the micro channels.

When the dimension of the channels goes down to several micro meters or less, the wall shear stress exceeds a critical value, so the wall slip happens. A modified power-law slip model is used in the simulation

$$u_s = \frac{a}{1+(\sigma_c / \sigma_w)^k} \sigma_w^i$$ (AII-20)

where σ_w is wall shear stress, σ_c is the critical wall stress for slip, i is a power-law index, and a is some scalar coefficient. The factor $\frac{1}{1+(\sigma_c / \sigma_w)^k}$ with a large power k basically zeros the slip velocity for stresses less than σ_c and becomes about equal to one for shear stresses slightly greater than σ_c.

Scheer[4,5] stated that the surface tension was the force that drew the polymer up along the wall, but Yao did not agree with it. The equivalent pressure change, Δp, at the front of capillary flows due to the surface tension can be calculated using this equation:

$$\Delta p = \frac{\lambda \cos \theta}{r}$$ (AII-21)

where λ is the surface tension of the liquid in units of Nm^{-1}, r is the radius of the capillary, and θ is the contact angle of the liquid with the capillary tube. For polymer PS, $\lambda \approx 0.033 Nm^{-1}$, and for the micro radius of the capillary, the maximum Δp is around 0.033MPa, which is much less than the injection molding pressure, 1~200Mpa. So, the surface tension force is not large enough to pull up the polymer.

AII-4. Summary

Several researchers are focusing on the investigation of the micro/nano embossing polymer flow. They interpreted the results mostly qualitatively based on the experimental study of embossing process. Based on the low Reynold's number fluid equations and incompressible non-slip Newtonian assumptions, they found out that polymer viscosity, embossing pressure, polymer film thickness and the geometry of the cavities were main factors that affect the embossing time. Increasing the embossing pressure, lower the polymer viscosity, and thickening polymer film will help reducing the embossing time.

Due to some reasons, the polymer fluid is not flowing into the cavities parallelly, which results in the imperfect surface quality, such as flower like, bound like and fingering surface. By choosing the embossing parameters, for example, increasing the thickness of the polymer film, increasing the embossing temperature will help improving the part quality. However, no surface quality criteria are set, and hence there is no real research on it yet. Other factors that affect the quality, such as the impact of vacuum on the bounds and fingering are still not clear.

There are some conflicts among the researchers when they are trying to explain the phenomena that they observed. Heyderman [1] explained that the polymer climbing the wall faster than the polymer in the center of the cavity was because of the polymer thinning near the wall. Whereas Yao [2] believed that either collective molecular motion effects or the immobility of the layer of molecules in contact with the solid surface made the viscosity near the wall 50-80% higher than the bulk viscosity.

Sometimes different phenomena were observed. Ressier[7] observed the bowing effect on the parts just after their being de-embossed from the dies, but in paper [6], the bowing effect was only detected after several months.

In the current research papers, the polymer is coated onto a substrate and form a thin layer. The research results show that sufficient polymer supply will help improving the final quality. So, in our research, we choose bulk polymer as the embossing object. In the following section, the high viscous polymer fluid flow into the cavity is simplified as a 2 dimensional problem, and the deduction procedure is shown below.

AII-5. 2-D micro viscous PMMA fluid flow into cavity in hot embossing process

In this section, all the equations are obtained based on the no slip boundary condition, constant viscosity and isothermal process assumptions.
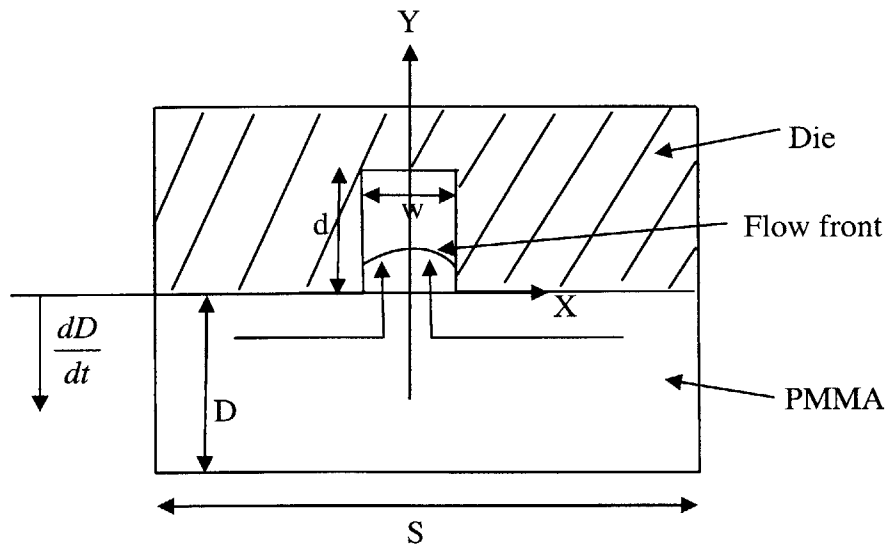

Figure AII-2.   2-D polymer fluid flow pattern

The figure above shows the embossing process: silicon die pressed the heated

PMMA piece with speed $\dfrac{dD}{dt}$; the viscous PMMA 'fluid' flows into the cavity of the die

under the assumptions given above.

'Fully developed' viscous fluid flow

In order to apply the fully developed viscous fluid theory, we need to find the

developing length of the flow and compare this length with the depth of the cavity

[Microsystem Design]:

$$L_d = \frac{d}{16} R_{ed} \qquad \text{(AII-22)}$$

where Reynolds number is

$$R_{ed} = \frac{WV}{\mu} \qquad \text{(AII-23)}$$

W and d are the width and depth of the cavity respectively. S and D are the width and

thickness of PMMA piece respectively.

Substitute (AII-23) into (AII-22), we get

$$L_d = \frac{dW}{16\mu} V \qquad \text{(AII-24)}$$

Since $dW \sim (10^{-12} \sim 10^{-8} m)$, $\mu \sim 10^4 (m^2 / s)$ and $V \ll 1(m/s)$, we

get $L_d \sim (10^{-16} \sim 10^{-12} m)$, which is much smaller than the depth $d \sim (10^{-6} \sim 10^{-4} m)$.

Thus, we can ignore the developing length, and look at the flow as a fully developed flow

from the beginning.

Filling flow into the cavity

'Non slip' boundary condition and parabolic flow front

'Non slip' boundary condition is assumed, so the velocity of the viscous flow has

a parabolic flow front with zero velocity at the wall.

$$V(x) = ax^2 + b \qquad \text{(AII-25)}$$

The boundary conditions are:

$$V(x)\big|_{x=-w/2\,\text{or}\,w/2} = 0 \qquad \text{(AII-26)}$$

Mass conservation

We assume the PMMA fluid is incompressible, and then the mass conservation is:

$$\frac{dl}{dt}(s-w) = \int_{-w/2}^{w/2} V(x)dx \qquad \text{(AII-27)}$$

from equation (4),(5)and(6), we get the parameters of the parabolic flow front as:

$$a = \frac{-6(s-2w)}{w^3} \cdot \frac{dl}{dt} \qquad \text{(AII-28)}$$

$$b = \frac{3s-4w}{2w} \cdot \frac{dl}{dt} \qquad \text{(AII-29)}$$

so, the velocity is

$$V(x) = \frac{-6(s-2w)}{w^3} \cdot \frac{dl}{dt} x^2 + \frac{3s-4w}{2w} \cdot \frac{dl}{dt} \qquad \text{(AII-30)}$$

Raynold's equation:

The Navier-Stokes equation in the very low Raynold's number situation is:

$$\mu \frac{d^2V}{dx^2} = \frac{dp}{dy} \qquad \text{(AII-31)}$$

Pressure boundary conditions are:

$$p\big|_{y=0} = p_0 \qquad \& \qquad p\big|_{y\ at\ flow\ front} = 0 \qquad \text{(AII-32)}$$

Solving equation (AII-9), we get

$$\frac{dl}{dt} = \frac{pw^3}{-12d(s-2w)\mu} \qquad \text{(AII-33)}$$

The velocity profile is

$$V(x) = \frac{1}{2d\mu} \cdot \frac{dl}{dt} \cdot x^2 - \frac{pw^2(3s-4w)}{24d(s-2w)\mu} \cdot \frac{dl}{dt} \qquad \text{(AII-34)}$$

The average velocity is

$$\bar{V} = \frac{\int\limits_{-w/2}^{w/2} V(x)dx}{w} = \frac{pw^2(s-w)}{-12d(s-2w)\mu} \tag{AII-35}$$

Hence, the estimated filling time is

$$t = \frac{d}{\bar{V}} = \frac{-12d^2(s-2w)\mu}{pw^2(s-w)} \tag{AII-36}$$

Equation (AII-36) shows the embossing filling time is proportional to the polymer viscosity and inversely proportional to the pressure, and relates to the cavity and features' geometry.

In this report, the filling process is assumed to be a Newtonian highly viscous fluid flow process, and no energy exchange happens. Maybe the non Newtonian fluid flow should also be considered.

Appendix II Reference

[1]   L.J. Heyderman, H. Schift, C. David, J. Gobrecht, T. Schweizer, *Flow behavior of thin polymer films used for hot embossing lithography*, Microelectronic Engineering 54 (2000), 229-245

[2]   H. Schift, L.J. Heyderman, M. Auf der Maur and J. Gobrecht, *Pattern formation in hot embossing of thin polymer films*, Nanotechnology 12(2001) 173-177

[3]   M.V.Chukalina, V.N.Matveev, V.V.Sirotkin, A.A. Svintsov and S.I.Zaitsev, *Deformation and viscous flow in nano-imprinting*, 8th Int. Symp. "Nanostructures:Physics and Technology", St. Petersburg, Russia, June 19-23, 2000

[4]   H.-C.Scheer, H.Schulz, *A contribution to the flow behaviour of thin polymer films during hot embossing lithography*, Microelectronic Engineering 56 (2001) 311-332

[5]   H.-C.Scheer, H.Schulz, D.Lyebyedyev, *Strategies for Wafer-Scale Hot Embossing Lithography*, Proceeding of SPIE 4349, (2001), p.86

[6]   H.Schulz, M. Wissen, H.-C. Scheer, *Local mass transport and its effect on global pattern replication during hot embsossing*, Microelectronic Engineering 67-68 (2003) 657-663

[7]   Laurence Ressier, Christel Martin, Jean Pierre Peyrade, *Atomic force microscopy study of micrometric pattern replica by hot embossing lithography*, Microelectronic Engineering 71 (2004) 272-276

[8]   S. Bickerton, M.Z. Abdullah, *Modeling and evaluation of the filling stage of injection/compression moulding*, Composites Science and Technology 63(2003) 1359-1375

[9]   Donggang Yao and Byung Kim, *Simulation of the filling process in micro channels for polymeric materials,* Journal of Micromechanics and Microengineering, 12 (2000) 604-610